DROPLET SOLIDIFICATION AND ITS EFFECTS ON DEPOSIT MICROSTRUCTURE IN THE UNIFORM DROPLET SPRAY PROCESS

by

Chen-An Chen

B.S. in Mechanical Engineering
National Chiao-Tung University, Hsin-Chu, Taiwan
(1986)

M.S. in Mechanical Engineering
Massachusetts Institute of Technology, May 1994

Submitted to the Department of Mechanical Engineering
in Partial Fulfillment of the Requirements for the Degree of

DOCTOR OF PHILOSOPHY IN MECHANICAL ENGINEERING

at the

MASSACHUSETTS INSTITUTE OF TECHNOLOGY

May 1996

Signature of Author _____
Department of Mechanical Engineering
June 28, 1996

Certified by _____
Professor Jung-Hoon Chun
Chairman, Doctoral Thesis Committee
Department of Mechanical Engineering

Accepted by _____
Professor Ain A. Sonin
Department of Mechanical Engineering

Droplet Solidification and its Effects on Deposit Microstructure in the Uniform Droplet Spray Process

by
Chen-An Chen

Submitted to the Department of Mechanical Engineering
on June 28, 1996 in Partial Fulfillment of the Requirements for the
Degree of Doctor of Philosophy in Mechanical Engineering

ABSTRACT

Spray forming is an alternative to conventional metal-working technology for the production of material preforms or near-net-shape components. However, the non-uniform droplets and coupling of process parameters associated with gas-atomized spray not only make process control difficult, but also severely limit the range of attainable microstructures. For this reason, the uniform-droplet spray (UDS) forming process was developed. The uniform droplet size and uncoupled process parameters allow for simplified modeling and precise microstructural control.

The microstructure evolution in the UDS process can be divided into three stages: droplet solidification in flight, droplet impact, and post-impact evolution. The droplet thermal states, characterized by the degree of undercooling in undercooled droplets or the liquid fraction and morphology of solids in partially solidified droplets, have a great influence on droplet impact behavior and post-impact microstructure evolution. It is the objective of this work to research how droplet solidification evolves during the UDS process. A droplet thermal model was developed to study the effects of various process parameters such as droplet charge, initial droplet velocity, and droplet size on droplet solidification. Experiments were also performed to investigate the effects on droplet solidification of flight distance, droplet size, and oxygen concentration using a Zn-20 wt% Sn alloy. The effects of droplet thermal state on the deposit microstructure in spray forming were studied using a Sn-5 wt% Pb alloy.

The droplet thermal model assumes Newtonian cooling in the droplets and simultaneously computes the droplet flight trajectory and droplet heat transfer. The Scheil equation was incorporated to model solute redistribution in the droplet during solidification. Several cases were run to study the effects of initial droplet velocity, droplet charge, and droplet size on droplet cooling. 200 μm diameter droplets with three different initial velocities (3, 5, and 7 m/s) were used to study the initial velocity effects. The simulation results show that droplets with a higher initial velocity have a higher cooling rate; however, they appear to have a higher temperature and liquid fraction when collected at the same flight distance due a quicker flight. 200 μm diameter droplets with three different droplet charges (2.3×10^{-12}, 4.1×10^{-12}, and 5.8×10^{-12} Coulomb) were used to investigate the droplet charge effects. The simulation results show that droplet charge affects droplet cooling mainly by changing the spreading distance, i.e., the distance at which the heat transfer coefficient increases dramatically. For the droplet size effect study, 100, 200, 300 μm droplets with the same initial velocity (5 m/s) were investigated. The results show that droplet size is the most critical process parameter in controlling the droplet cooling rate.

For the flight distance effect study, 288 μm droplets were collected using carbon steel substrates at every 0.05 m from 0.35 to 0.75 m and 181 μm droplets were collected from 0.15 to 0.55 m. Scanning electron microscopy revealed surface morphology and cross-sectional microstructures. The results showed that the 288 μm droplets solidified gradually without undercooling and the 181 μm droplets experienced about 110 K undercooling.

The cross-section micrographs of the 288 μm droplet samples were image analyzed to determine the liquid fraction. These liquid fractions show good agreement with those derived from the simulation. For the droplet size effect study, 288, 245, 181, and 96 μm droplets were collected at the bottom of the chamber using an oil bath. The results show that the 288 μm droplets experienced virtually no undercooling with dendritic microstructure and surface nucleation. Three types of microstructures were observed for the 245 μm droplets. The first type is similar to the 288 μm droplet microstructure. About 28% of the 245 μm droplets collected belong to this category. The second type is characterized by a cellular structure nucleated within the droplet and dendritic structures solidified after recalescence. About 63% of the 245 μm droplets collected belong to this category. The third type is defined by a cellular structure nucleated on the droplet surface and dendritic structures solidified after recalescence. About 9% of the 245 μm droplets collected belong to this category. The 181 and 96 μm droplets were all undercooled and internally nucleated. The percentage of the cellular structure increases and the sizes of the cells and dendrites decrease when droplet size decreases. Kinetic competition between different catalysts for nucleation explains why the population of undercooled droplets, the degree of undercooling, and the tendency to nucleate internally increase as the droplet size decreases. For the oxygen effect experiment, 181 μm droplets were sprayed and collected using an oil bath with the chamber oxygen concentrations maintained at 5, 50, and 100 ppm. No significant difference in the cross-section microstructure is evident. The droplets are undercooled and internally nucleated.

Seven experiments were performed to study the effects of the droplet thermal state and the substrate condition on the droplet microstructure by spraying droplets of 100% liquid with 85 K superheat, 100% liquid with no superheat, 70% liquid, and 40% liquid onto a substrate maintained at 426 and 446 K, respectively. Droplets with 100% liquid all produced epitaxial columnar microstructures. With 70% liquid droplets and a 446 K substrate, a fine, equiaxed, dense microstructure was produced. Porous structures resulted when 70% liquid droplets were deposited onto a 426 K substrate or when 40% liquid droplets were deposited onto a 446 K substrate. The epitaxial columnar microstructure resulted because nucleation in the molten splat was more difficult than the continuous growth of the columnar crystals into the newly added liquid layer. The equiaxed microstructure evolved mainly from randomly oriented crystals, which were originally present as dendrites in the droplets and were re-oriented upon impact. Porous structures resulted because the degree of droplet spreading was reduced either due to low liquid content in the droplets or due to high freezing rate resulting from a relatively cold substrate.

Thesis Supervisor: Dr. Jung-Hoon Chun

Title: Edgerton Associate Professor, Department of Mechanical Engineering

Acknowledgments

I would like to thank the many people who have helped me complete my education and thesis at MIT. Special thanks are due:

First and foremost to my wife and best companion, Chia-Hui, for providing encouragement and support whenever I needed it, for patiently enduring my frequent absences in the evenings and on weekends, and, most of all, for sharing life with me.

To my parents, for their caring and financial support over the years. Without them, this thesis could have never been accomplished.

To my thesis supervisor, Professor Jung-Hoon Chun, for the freedom to explore ideas, for confidence in me, and for the best education a professor can provide — to let me believe in myself. To him, my gratitude is eternal.

To Professor Teiichi Ando, for leading me to the discipline of materials science and engineering and for his many helpful discussions.

To my other thesis committee members, Professors Samuel Allen and John Vander Sande, for their time and advice.

To the members of the DBM group — Jeanie Cherng, whose mere presence would enlighten the whole laboratory, Sukyoung Chey, who always shared his point of view in religions with me, Ho-Young Kim, who is probably one of the best friends I have made at MIT, Jiun-Yu Lai, whom I thank for preparing some pictures for this thesis, Tom Nowak, whom I always turned to for advice, Juan-Carlos Rocha, whom I thank for helping with some experiments, Wes Williams, who constantly reminded me that I looked ugly, and Pyongwon Yim, from whom I have learned many things about life and technique — to all of them for their companionship and inspiration.

To Fred Cote for helping me design and build most of the apparatus in the laboratory.

To Yin-Lin Xie for providing assistance in the Materials Science and Engineering Laboratory.

To Diane D'Alderette for being a terrific friend to me.

To Julie Drennan for providing excellent administrative support and for proofreading this thesis.

Finally, I would like to dedicate this volume to my wife and my parents.

This work was supported by the National Science Foundation
under grant No. DDM 930375.

Table of Contents

List of Figures

Chapter 4

List of Tables

Chapter 1
Introduction

1.1 Background

For the production of parts or materials with optimal microstructure and properties, spray forming offers an attractive alternative to conventional casting. This is due in large part to rapid solidification within the droplets and incremental solidification at the deposit surface [1,2]. Numerous studies have shown that these processes can produce materials with fine, equiaxed microstructures and little phase segregation in a variety of alloy systems [3-10]. Although these studies are promising, several constraints inherent to these processes limit the full potential of the spray forming concept [11]. Gas atomization, for example, results in a spray with a wide distribution of droplet diameters and trajectories. Droplets of different sizes will solidify at different rates, resulting in a spray which contains liquid, partially liquid droplets, and solid particles. Varying droplet sizes result in a restricted range of attainable microstructures, frequent problems of porosity [11,14], and limited utilization of process models. The uniform droplet spray (UDS) process was developed to overcome these shortcomings [15-16].

A schematic of the droplet generation unit for the UDS process is shown in Figure 1.1. The droplet generation unit, contained in a gas-tight chamber, consists of a stainless-steel melting crucible with an orifice at the bottom, a band heater placed around the melting crucible, a vibration transmitter connected to a piezoelectric transducer, a droplet charging plate, and a moving copper substrate placed on a computer-controlled x-y table. In this process, a charge of metal is melted in a heated crucible. By applying pressure to the crucible, molten metal is ejected through the orifice to form a laminar jet. The jet is then broken into uniform droplets at a desired frequency by vibrations imposed by the piezo-electric transducer. Each droplet is then electrically charged by the DC voltage charging plate as it breaks from the jet to prevent merging with other droplets and to control the

spreading of the uniform droplets as they travel down the chamber. Due to the charge, the droplets repel each other to form a uniform spray. The uniform droplets are then deposited onto the temperature- and motion-controlled substrate to produce the desired deposit shape and microstructure. In the UDS process, all spray parameters are uncoupled. When combined with computer-controlled substrate motion, the UDS process can produce a wide range of tightly controlled spray forming conditions, many of which are not available to non-uniform droplet spray processes.

The microstructure evolution in the UDS process can be divided into three stages: droplet solidification in flight; droplet impact; and post-impact evolution. Droplet thermal states, characterized by the degree of undercooling in undercooled droplets or the liquid fraction and morphology of solids in partially solidified droplets, can have an great influence on droplet impact behavior and post-impact microstructure evolution. Therefore, it is essential to understand how droplet solidification evolves during the process in order to achieve precise microstructural control.

1.2 Literature Review

1.2.1 Modeling of Droplet Solidification

Modeling of droplet solidification in gas-atomized spray forming processes has attracted much scientific and industrial interest. Most of the earlier works were concerned with isothermal solidification, in which the interface temperature is fixed at the melting point and the solidification interface is concentric [17,18,19,20]. Lei and Mehrabian developed both a Newtonian and a non-Newtonian model for simulating the solidification of a undercooled pure metal droplet [21]. The interface velocity was calculated based on the kinetic equation suggested by Turnbull [22]. Relationships are established among the growth kinetics, the interface velocity, and undercooling. Similar work was performed by Levi [23] on binary alloys based on a Newtonian model. Works incorporating droplet velocity profiles in simulating droplet solidification were also developed for gas-atomized

spraying processes [12,13]. More recently, Zhao [24] modeled undercooled droplet solidification in two dimensions using experimentally determined dendrite growth rates and the dendrite growth model based on the theory of Lipton, Kurz, and Trivedi [25]. This model correctly predicts bulk sample recalescence temperature at different undercoolings. Passow [26] constructed a droplet solidification model for the UDS process by considering the droplet flight path change due to the interaction among the gravity force, drag force, and electrical repulsion force. His model is restricted to the solidification of pure metals.

1.2.2 Experimental Works on Droplet Solidification

Numerous work have been carried out to study droplet solidification experimentally. Many of the experiments studied the undercooling of droplets by dispersing liquid metals into a large number of isolated droplets. By applying this method, Turnbull and Cech reported temperature measurements of undercooled metals and investigated the nucleation kinetics of these undercooled droplets [27,28]. Chu et al. studied the undercooling behavior of tin-lead droplets with various compositions by emulsifying the droplets in an organic oil [29]. Recently, the pyrometric technique has been employed for the thermal measurement of undercooled droplets. More detailed information on recalescence has been reported [24,30,31,32,33]. Droplet solidification in gas-atomized processes was studied indirectly through examining and analyzing the powder microstructures due to the difficulty in direct measurement of droplet temperature and liquid fraction in real spray forming conditions. Microstructure development related to solidification in two alloy steel compositions was examined as a function of powder size by Sriharan and Perepezko [2]. They found that with decreasing powder size the solidification morphology changed from a dendritic to a cellular mode with a refined size scale.

1.2.3 Effects of Droplet Thermal State on Deposit Microstructure

Due to the non-uniform droplet size and coupling of process parameters in gas-atomized spraying processes, effects of droplet thermal state on deposit microstructure are difficult to investigate. Often deposit microstructures are related to the spray density or

melt flow rate. Singer and Evans [1] produced deposits with two different microstructures by varying the spray density. Bewlay and Cantor [9] investigated the microstructure change due to the change in melt flow rate and gas flow rate. However, work on the effects of droplet thermal state on deposit microstructure has not been reported.

1.3 Goal of Research

Although droplet solidification has been studied intensively, understanding of droplet solidification in non-experimental situations is still very limited due to the difficulty in conducting experiments and in measuring the degree of solidification. No work has been reported on the liquid fraction and solid morphology of partially solidified droplets in spray forming. With uniform droplet size and decoupled process parameters, the UDS process is an ideal tool for studying droplet solidification in real spray forming situations. Since the UDS process is new, the relationships between the process parameters, droplet solidification and deposit microstructure are still unclear. Therefore, the goals for this work are:

(1) Develop a droplet solidification model for binary alloys for the UDS process and study the effects on droplet solidification of various process parameters through numerical simulations.

(2) Study the effects on droplet solidification of various process parameters experimentally and verify the numerical model by comparing the liquid fractions derived experimentally and numerically.

(3) Study the effects of droplet thermal states on deposit microstructure to provide a general description of how droplet thermal states influence final deposit microstructure.

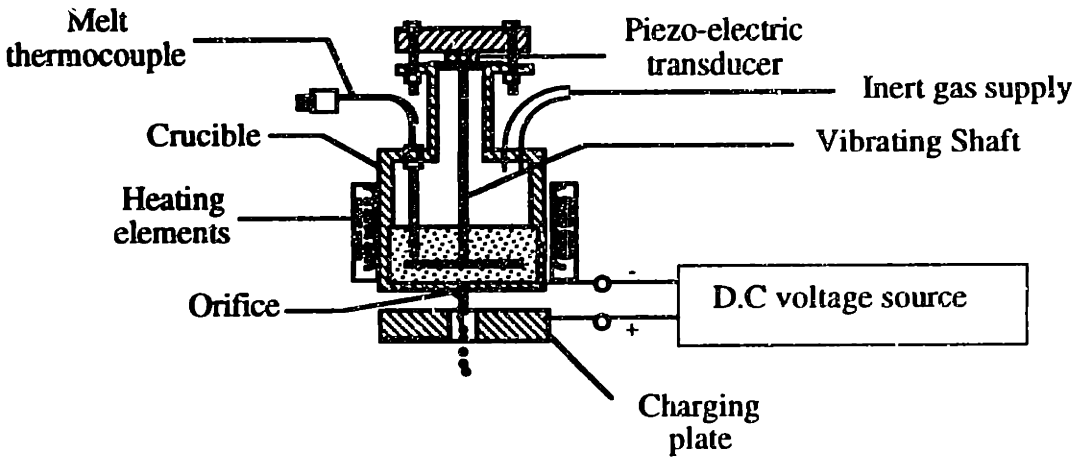

Figure 1.1 Droplet Generation Unit for the UDS process

Chapter 2
Droplet Solidification in Flight: Modeling

2.1 Introduction

Modeling of droplet solidification for the UDS process is made relatively easy by the uniformity of size and velocity profile of the droplets. Since no statistical or empirical derivation is involved in obtaining the droplet size and velocity distribution, a precise model for droplet solidification is possible. The objective of this chapter is to develop an accurate model to provide a design tool for laboratory experiments and industrial spray forming processes.

In the UDS process, charged droplets scatter as they travel. The scattering affects the velocity and thus the cooling rate. Consequently, droplet flight path and solidification should be modeled simultaneously. A droplet flight trajectory model developed by Passow [28] is incorporated into a droplet thermal model developed by the author to simulate droplet solidification in the UDS process. Droplet velocities calculated by the droplet thermal model are input to the droplet thermal model to compute droplet heat transfer and thus the droplet solidification. The droplet flight trajectory model is described briefly below. The droplet thermal model capable of predicting the temperature and liquid fraction of non-undercooled droplets is discussed in more detail. The effects on droplet solidification of several process parameters such as initial jet velocity, droplet charge, and droplet size are studied through simulation.

2.2 Droplet Flight Trajectory Model

The droplet flight trajectory can be modeled by considering all the forces acting on the droplets. Figure 2.1 illustrates the forces imposed on a droplet. Based on the force balance, the equation of motion for the droplets can be written as:

$$m_d \frac{d\vec{v}_d}{dt} = \vec{F}_g + \vec{F}_d + \vec{F}_c \tag{2.1}$$

where $\vec{v}_d$ is the velocity of the droplet, $\vec{F}_g$, the gravity force, $\vec{F}_d$, the drag force, and $\vec{F}_c$, the Coulomb force.

The gravity force is merely the product of the droplet mass and the gravity constant. It is given by:

$$\vec{F}_g = - m_d \, g \, \vec{Z} \tag{2.2}$$

where $\vec{Z}$ is the unit vector in the vertical direction.

The total Coulomb force acting on the droplet is derived by summing all the Coulomb forces imposed by its neighboring droplets. It is given by:

$$\vec{F}_C = \frac{1}{4 \Pi \varepsilon_o} \sum_{j=0}^{N} \frac{q_d^2}{\vec{r}_j} \tag{2.3}$$

where ε_o is the permittivity of free space, N is the total number of droplets in flight, q_d is the electrical charge carried by each droplet, and rj is the distance between the droplet and droplet j. Since the droplets are all aligned initially, the horizontal component of the coulomb force for each droplet should be maintained at zero if the droplets are not disturbed horizontally. However, disturbances are always present to cause the droplets to become unstable and to deviate from the centerline as they travel. Therefore, the disturbances should be taken into account in the droplet flight trajectory modeling. The disturbances are modeled in this work by superimposing a randomly oriented horizontal displacement of fixed magnitude to each droplet. The magnitude of the displacement is obtained by forcing

the simulation derived spray cone width to equal to the one derived experimentally. This magnitude is found to be approximately the droplet diameter divided 10000.

The drag force, $\vec{F}_d$, can be expressed as:

$$\vec{F}_d = -1/8\, C_d\, \pi\, \rho_m\, d_d^2\, |\vec{v}_d|\, \vec{v}_d \tag{2.4}$$

where C_d is the coefficient of drag, ρ_m is the density of the metal, and $\vec{v}_d$ is the velocity of the droplet. In the UDS process, the droplets are in a stream before they scatter. Therefore, the drag coefficient employed in Equation 2.4 must account for the alignment and scattering of the droplets. For a droplet in free flight, the coefficient of drag, C_{D_s}, is equal to [34]:

$$C_{D_s} = 0.28 + \frac{6}{\sqrt{Re}} + \frac{21}{Re} \tag{2.5}$$

where Re is the Reynolds number of the droplet. According to Mulholland et al. [35], the drag coefficient for an aligned stream of droplets, C_{D_A}, is:

$$C_{D_A} = \left[(C_{D_{1+}})^{-n} + (C_{D_S})^{-n} \right]^{-1/n} \tag{2.6}$$

where n is an empirical parameter (n=0.678+/-.07), C_{D_s} is the drag coefficient of a sphere as given in Equation 2.5, $C_{D_{1+}}$ is the drag coefficient as ratio of droplet spacing and diameter of the droplets approaches one (l_d/d_d->1). This drag coefficient, $C_{D_{1+}}$, is equal to:

$$C_{D_{1+}} = C_{D_1} + \frac{a}{Re} (\lambda_d / d_d - 1) \tag{2.7}$$

where a is another empirical parameter (a=43.0+/-15.4), Re is the Reynolds number for the droplets, and C_{D_1} is the drag coefficient when droplet spacing over diameter equals one (l_d/d_d=1). It is given by:

$$C_{D_1} = \left[(C_{D_{rod}})^{n} - (C_{D_S})^{n}\right]^{-1/n} \tag{2.8}$$

where $C_{D_{rod}}$ is the drag coefficient for a rod and is equal to 0.755 / Re. Before the droplets have scattered more than one drop radius from the centerline, a weighted average, C_{D_r}, of the coefficients C_{D_S} and C_{D_A} is used:

$$C_{D_r} = (1 - r/r_d)\, C_{D_A} + (r/r_d)\, C_{D_S} \tag{2.9}$$

where r is the distance from the centerline and r_d is the radius of the droplets. After that, the drag coefficient of a single sphere is used.

The non-linear equations of motion for the droplets are solved using a fourth-order Runge-Kutta numerical integration. Velocity from this model is used to obtain the heat transfer coefficient of droplets in flight.

2.3 Droplet Thermal Model

2.3.1 Heat Transfer of Droplets

The temperature history and solidification of droplets can be modeled by considering the their heat loss to the surrounding environment through convection and radiation. Based on the heat balance, the governing equation for the heat transfer of a droplet can be written as:

$$m_d \frac{dH}{dt} = h\, A_d^s (T_d - T_g) + \sigma\, \varepsilon\, A_d^s \left(T_d^4 - T_g^4\right) \tag{2.10}$$

where m_d is the total mass of the droplet, H is the enthalpy of the droplet per unit mass, h is the convective heat transfer coefficient, A_d^s is the surface area of the droplet, σ is the Stefan-Boltzman constant, ε is the emissivity, T_d is the droplet temperature, and T_g is the gas temperature. The radiation term can be neglected for low melting point metals and alloys such as tin, lead, and zinc since it is magnitudes of order less than the convection term at low temperatures. For high melting point metals and alloys, such as bronze, it becomes important. A uniform temperature distribution in the droplets (Newtonian cooling) can be assumed if the Biot number ($Bi=hd_d/k_d$) is less than .01. That is the case in this study for Zn-20 wt% Sn droplets as large as 300 μm. The convective heat transfer coefficient, h, is given by [23]:

$$h = \left(\frac{k_g}{d_d}\right)\left(2.0 + 0.6\, Re^{1/2}\, Pr^{1/3}\right)\left(\frac{C_{g(avg.)}}{C_g}\right)^{0.26} \tag{2.11}$$

where k_g is the thermal conductivity of the gas, C_g is the heat capacity of the gas at the gas temperature, and $C_{g(avg.)}$ is the heat capacity of the gas at the average of the gas and droplet temperatures. Re is the Reynolds number and Pr the Prandtl number. To account for the aligned stream of droplets, the heat transfer coefficient is adjusted by the ratio C_{D_r}/C_{D_s}, where C_{D_r} is the adjusted drag coefficient for a line of droplets and C_{D_s} is the drag coefficient of a single droplet. This adjustment is made based on the assumption that the development of the thermal boundary layer around a droplet bears a similarity to that of the momentum boundary layer. Therefore, the adjusted heat transfer coefficient is written as:

$$h_{aligned} = \frac{C_{D_r}}{C_{D_s}} h \tag{2.12}$$

In general, the enthalpy of a binary alloy per unit mass, H, can be formulated as:

$$H = f_\ell H_\ell + (1 - f_\ell) H_S \tag{2.13}$$

where f_ℓ is the liquid fraction, H_ℓ is the enthalpy of the liquid portion, and H_s is the enthalpy of the solid portion. H_ℓ and H_s, respectively, can be expressed as:

$$H_\ell = (1 - \overline{C}_\ell) H_{\ell,1}(T) + \overline{C}_\ell H_{\ell,2}(T) \tag{2.14}$$

$$H_S = (1 - \overline{C}_S) H_{S,1}(T) + \overline{C}_S H_{S,2}(T) \tag{2.15}$$

where $\overline{C}_\ell$ and $\overline{C}_S$ are the average weight composition of the solute in the liquid and in the solid, $H_{\ell,1}$ and $H_{\ell,2}$ are the enthalpies of the primary phase and the solute in the liquid phase, and $H_{S,1}$ and $H_{S,2}$ are the enthalpies in the solid phase, respectively. Equations 2.14 and 2.15 are based on the assumption that the heat of mixing effect on the enthalpy change can be neglected as insignificant. In order to calculate Equation 2.13, f_ℓ, $\overline{C}_\ell$, and $\overline{C}_S$ must be expressed in terms of the temperature T. In the mushy regime, these relationships depend on the solidification model employed. Therefore, a solidification model should be adopted before Equation 2.10 can be solved.

2.3.2 Solidification Model

The Scheil equation is employed in this work to model solute redistribution in the droplet during solidification. The "Scheil equation" solidification model assumes no diffusion in the solid phase, complete diffusional mixing in the liquid phase, and local equilibrium at the solid-liquid interface [36]. Figure 2.2 illustrates these assumptions with a schematic diagram. With these assumptions, the Scheil equation is obtained by equating the solute rejected by the solidified solid and the resulting increase of solute in the liquid. This balance is:

$$(C_\ell - C_S^*) df_\ell = f_\ell dC_\ell \tag{2.16}$$

where C_ℓ is the weight composition of the solute in the liquid, C_S^* is the weight composition of the solute at the solid interface, and f_ℓ is the liquid fraction. Note that if undercooling does not occur and local equilibrium is maintained at the solid-liquid interface, the equilibrium phase diagram can be applied to obtain the relationship between C_ℓ and C_S^*. Equation 2.16 can then be integrated from $C_\ell = C_O$ at $f_\ell = 1$ to yield the liquid fraction, f_ℓ, as a function of the liquid composition, C_ℓ. C_O is the initial composition. As a result, the liquid fraction can be expressed in terms of T since the relationship between C_ℓ and T can be derived from the equilibrium phase diagram. Finally, Equation 2.10 can be solved for the temperature and liquid fraction of the droplet.

2.4 Simulation of Droplet Solidification

A MATLAB program was written to simulate solidification of Zn- 20wt% Sn droplets in the UDS process (see Appendix A). Physical constants used in the simulation are described in Appendix B. Figure 2.3 shows the flow chart of the program. First the process parameters such as the melt temperature, initial jet velocity, orifice size, perturbation frequency, DC charging voltage, and final flight distance are put into the program. With this information, the program predicts the change of droplet acceleration, velocity, and position within a small time step based on Equation 2.1. The droplet heat transfer coefficient is then calculated to give the enthalpy loss within the time step. Following this, an iteration method obtains the temperature change of the droplet according to Equation 2.13 and the Scheil equation to match the calculated enthalpy loss. The program then stores important variables and checks the flight distance. If the final distance is reached, the program ends, if not, the program continues the loop.

Several cases were run to study the effects of initial droplet velocity, droplet charge, and droplet size on droplet cooling. The parameters used in these simulations are listed in Tables 2.1, 2.2, and 2.3. Droplets with a 200 μm diameter and with three different initial

velocities, 3 , 5 , and 7 m/s, were used to study the initial velocity effects. Droplets with a 200 μm diameter and with three different droplet charges, 2.3×10^{-12} , 4.1×10^{-12} , and 5.8×10^{-12} Coulomb, were used to investigate the droplet charge effects. For the droplet size effect study, 100, 200, and 300 μm droplets with the same initial velocity, 5 m/s, were investigated.

2.5 Results and Discussion

2.5.1 Initial Velocity Effect Study

The initial velocity affects droplet cooling through two mechanisms. The first mechanism functions by varying the spreading distance, at which point the heat transfer coefficient increases dramatically as mentioned earlier in the modeling section. The spreading distance is defined as the flight distance at which the droplets scatter from the centerline for a distance equal to the droplet diameter. The second mechanism works by changing the heat transfer coefficient through droplet velocity according to Equation 2.11. Thus, it is necessary to examine how the spreading distance and the droplet velocity vary with the initial jet velocity before their effects on droplet cooling can be investigated. As shown in Figure 2.4, the velocities for both the 3 and 5 m/s cases increase initially and then decrease toward the terminal velocity, which is slightly less than 3 m/s. The velocity for the 5 m/s case varies from 5 m/s at the start to 3.6 m/s at the end of 1 m long flight distance. The velocity change for the 3 m/s case is insignificant since the initial velocity is already close to the terminal velocity. The initial increase in velocity is caused by the reduction in the drag coefficient due to the alignment of the droplets. The velocity curve for the 7 m/s case, however, does not show an initial rise because the reduction in the drag coefficient is overcome by the increase in the drag force due to the high initial velocity. Variations in the starting points of spreading can be noticed. As shown in Figure 2.4, the spreading distance increases with initial velocity.

The effects of the initial velocity on droplet cooling can now be illustrated easily by the heat transfer coefficient vs. flight time plot presented in Figure 2.5. As shown in the figure, the spreading times are approximately the same for all three cases, and the heat transfer coefficient increases with the initial velocity. It therefore can be concluded that droplets with a higher initial velocity experience faster cooling. When the temperatures of the droplets are plotted against time, droplets with higher initial velocities should have a lower temperature at any certain flight time. The use of flight time however is not practical; the flight distance is applied in process design and control more often. To examine how the temperature plot will change when the flight distance is employed instead of the flight time, the amount of heat loss, Q_L, at a fixed distance, L, is calculated as:

$$Q_L = h_{L(avg.)}\, t_L \tag{2.17}$$

where t_L is the flight time to reach the distance, and h_L(avg.) is the averaged heat transfer coefficient during the flight time. To express t_L and $h_{L(avg.)}$ in terms of flight time, the following equations can be written as:

$$h_{L(avg.)} \propto v_{d(avg.)}^{0.6} \tag{2.18}$$

$$t_L \propto \frac{1}{v_{d(avg.)}} \tag{2.19}$$

where $v_{d(avg.)}$ is the averaged droplet velocity from flight distance 0 to L. Equation 2.18 is derived from 2.11 with the consideration that the term $(2+Re^{1/2})$ can be approximated by $(Re^{0.6})$ for the range of interest. Therefore, the relationship between the Q_L and the averaged velocity is given by:

$$Q_L \propto \left(\frac{1}{v_{d(avg.)}}\right)^{0.4} \tag{2.20}$$

It can be concluded from Equation 2.20 that droplets with a higher initial velocity will lose less heat than droplets with a lower initial velocity at the same flight distance. This conclusion is confirmed by the temperature vs. flight distance plot shown in Figure 2.6 (a). Note that the longer spreading distance associated with a higher initial velocity further reduces the amount of heat loss at a fixed flight distance.

As shown in Figure 2.6 (a), the temperatures initially decrease slowly in the mushy regime; after a certain point they decrease more abruptly until reaching the eutectic point (471.5 K). This phenomenon occurs because at the early stage of solidification the enthalpy lost is used to solidify the pure zinc phase; while at the later stage, it becomes more difficult to solidify the pure zinc phase from a high concentrated solution of tin. The enthalpy loss is largely compensated by the decrease in temperature rather than by phase transformation. As shown in Figure 2.6 (b), the difference in liquid fraction between the 3 m/s case and the 7 m/s case is averaged at 0.3 from flight distance 0.20 to 0.50 m. After 0.50 m, the difference decreases dramatically because the rate of increase in liquid fraction decreases.

2.5.2 Droplet Charge Effect Study

The simulation results of the droplet charge effect study are shown in Figures 2.7 and 2.8. As shown in Figure 2.7 (a), the velocities for all three cases increase initially and then decrease after the droplets reach the spreading distances. The spreading distance decreases as the droplet charge increases since the spreading distance is inversely proportional to the repulsion force, i.e., the droplet charge. A shorter spreading distance resulting from a smaller droplet charge leads to an earlier deceleration of the droplets and thus a lower droplet velocity. The difference in velocity for the three cases studied is smaller than 0.5 m/s. This small velocity difference causes a slight variation in the heat transfer coefficient

as shown in Figure 2.7 (b). Such a variation is insignificant when compared to the dramatic increase in convective heat transfer upon droplet scattering. Therefore, droplet charge affects droplet solidification mainly by changing the spread distance, i.e. the location at which the heat transfer rate jumps. The shorter the spreading distance, the less time the droplets stay in the lower heat transfer regime, and the faster the droplets cool. This phenomenon is readily observed from Figure 2.8 (a). As shown in the figure for the 2.3×10^{-12} Coulomb case, the delay in the spreading is reflected by the delay in reaching the eutectic temperature at a later stage. Figure 2.8 (b) presents the liquid fraction vs. flight distance plot. As shown in the figure, the difference in liquid fraction between the 2.3×10^{-12} Coulomb case and the 5.8×10^{-12} Coulomb case is approximately 0.2 from flight distance 0.25 to 0.45 m. After 0.45 m, the difference decreases because the enthalpy loss of the droplets is largely compensated by the decrease in temperature rather than by phase transformation.

2.5.3 Droplet Size Effect

The results of the droplet size effect study are presented in Figures 2.9 and 2.10. As shown in Figure 2.9 (a), the velocities for both the 300 μm and 200 μm cases increase initially and then decrease after the spreading distance. The velocity change for the 200 μm case is more prominent than that for 300 μm case. The simulation was run for the 100 μm case from flight distance 0 to 0.5 m because the droplets have already cooled to ambient temperature by the time they reach 0.5 m. The velocity for this case decreases continuously from 5 m/s at the start to 1.6 m/s at the end of the simulation. Major differences in spreading distance can be observed in Figure 2.9 (a). The spreading distance for the 300, 200, and 100 μm cases are 0.04, 0.10, and 0.18 m, respectively.

The heat transfer coefficient vs. flight distance plot is shown in Figure 2.9 (b). As shown in the figure, the change in the heat transfer coefficient induced by varying droplet size is much more than that caused by varying initial droplet velocity or droplet charge. The heat transfer coefficient increases more than twice when the droplet size decreases from

300 to 100 μm. In addition to the heat transfer coefficient, the area to volume ratios of the droplets must also be considered in evaluating the droplet size effects on droplet cooling. The rate of enthalpy loss per unit droplet mass, $\dot{H}$, can be written as:

$$\dot{H} = \frac{A}{\rho V} h \Delta T \tag{2.21}$$

where A is the droplet surface area, V is the droplet volume, ρ is the density and h is the heat transfer coefficient as described in Equation 2.11. By substituting the area and volume of the droplet into Equation 2.21, Equation 2.21 becomes:

$$\dot{H} = \frac{6}{\rho d_d} h \Delta T \tag{2.22}$$

where d_d is the droplet diameter. From Equation 2.22 and Figure 2.9 (a), it can be concluded that the rate of enthalpy loss increases dramatically as droplet size decreases. Other factors such as the shorter spreading distance and the lower average velocity add up to increase the amount of heat lost at a fixed flight distance for smaller droplets. As shown in Figure 2.10, the 100 μm droplets solidify completely at 0.28 m, while the 300 μm droplets remain approximately 40% liquid at 1 m.

2.6 Conclusions

(a) Droplets with a higher initial velocity have a higher cooling rate. However, since the time required for them to reach a certain flight distance is shorter, they lose less heat than the droplets with a lower velocity at the same flight distance. Therefore, droplets with a higher velocity appear to have a higher temperature and liquid fraction when collected at the same flight distance.

(b) The droplet charge affects droplet cooling mainly by changing the spreading distance, i.e. the distance at which the heat transfer coefficient increases dramatically. The delay in spreading distance for less charged droplets is reflected by the delay for the droplet temperature to reach the eutectic point. The heat transfer coefficient change resulting from the small velocity change is insignificant in influencing droplet cooling.

(c) Droplet size is the most critical process parameter in controlling the droplet cooling rate. A wider range of cooling rates is achieved by varying the droplet size than by altering the initial velocity or droplet charge. Smaller droplets cool faster and solidify in short distance; thus they are more sensitive to variations in flight distance than larger droplets.

Table 2.1 Simulation conditions for the initial velocity effect study.

Initial jet velocity (m/s)	7	5	3
Droplet size (μm)	200	200	200
Droplet charge (Coulomb)	5.8×10^{-12}	5.8×10^{-12}	5.8×10^{-12}
Melt temperature (K)	708	708	708

Table 2.2 Simulation conditions for the droplet charge effect study.

Droplet charge (Coulomb)	2.3×10^{-12}	4.1×10^{-12}	5.8×10^{-12}
Initial jet velocity (m/s)	5	5	5
Droplet size (μm)	200	200	200
Melt temperature (K)	708	708	708

Table 2.3 Simulation conditions for droplet size effect study.

Droplet size (μm)	100	200	300
Droplet charge (Coulomb)	4.1×10^{-12}	4.1×10^{-12}	4.1×10^{-12}
Initial jet velocity (m/s)	5	5	5
Melt temperature (°C)	708.15	708.15	708.15

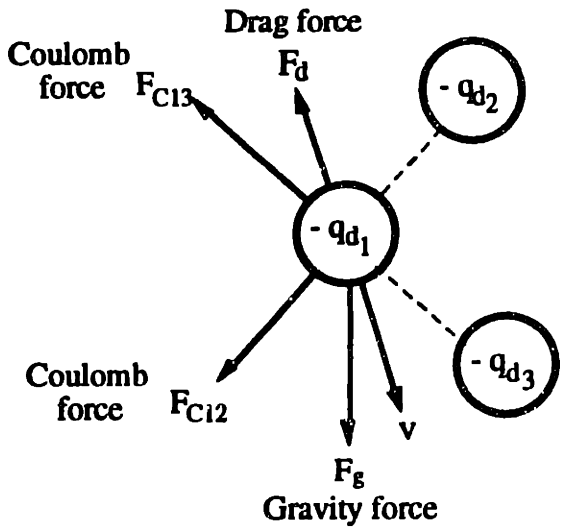

Figure 2.1 Forces acting on a single droplet.

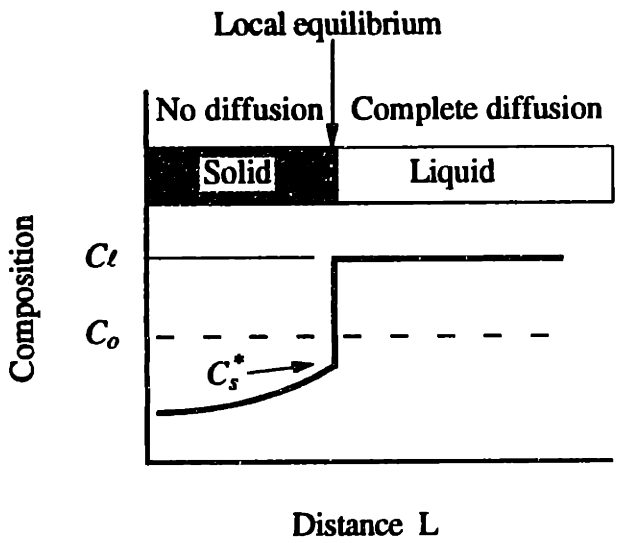

Figure 2.2 Solute redistribution in Scheil equation.
C_o is the initial solute composition in the liquid.

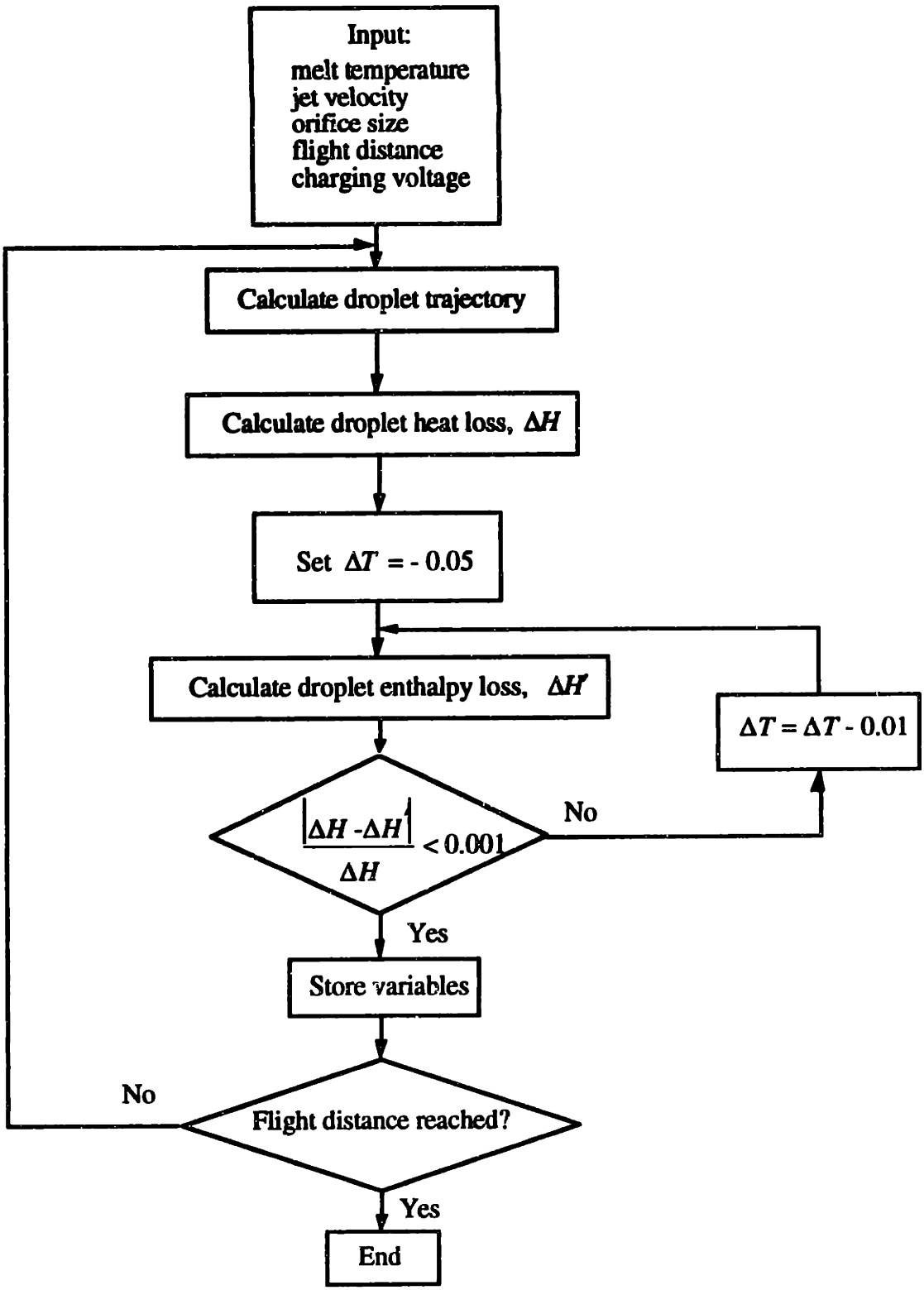

Figure 2.3 Flow chart for the droplet solidification simulation program.

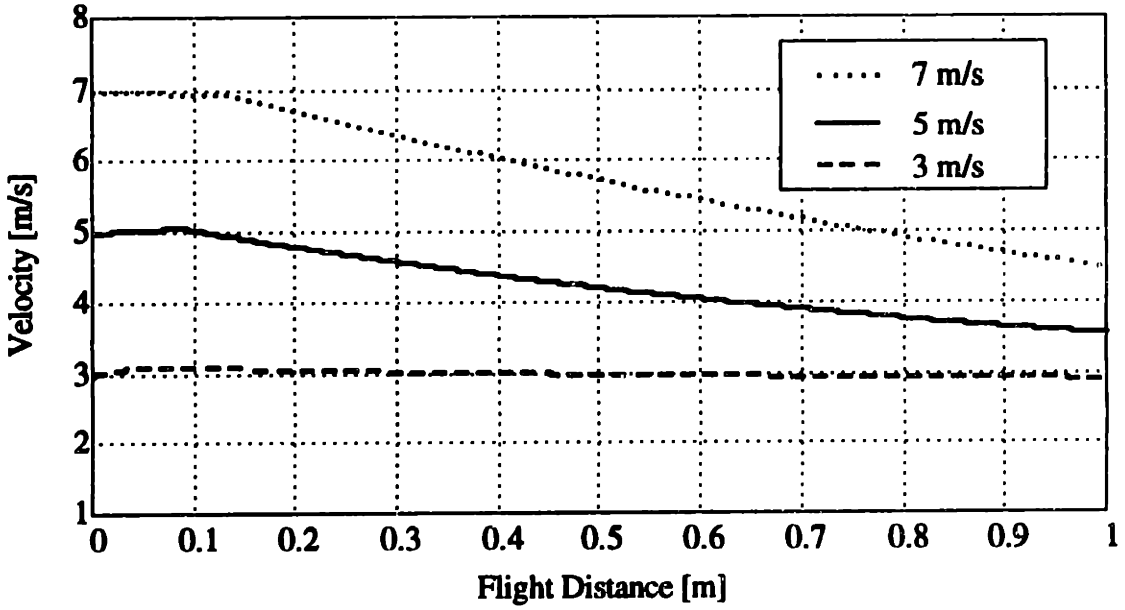

Figure 2.4 Velocity vs. flight distance plot for the initial velocity effect study. Droplet velocities approach the terminal velocity, at approximately 3 m/s, as the flight distance increases.

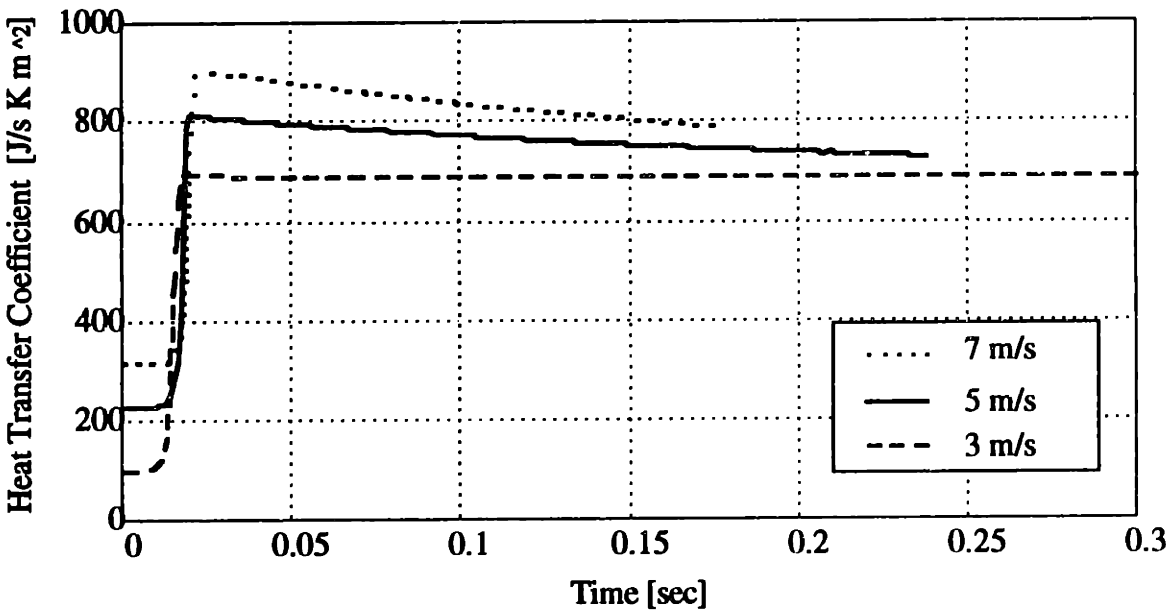

Figure 2.5 Heat transfer coefficient vs. time plot for the initial velocity effect study. The sudden increase in the heat transfer coefficients is due to spreading of the droplets.

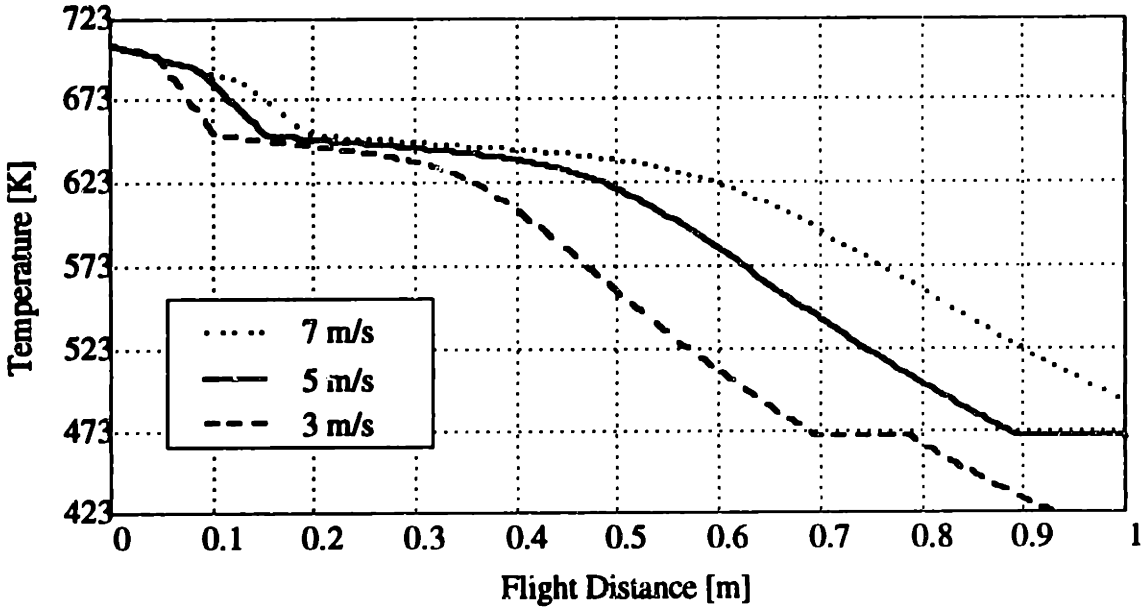

(a)

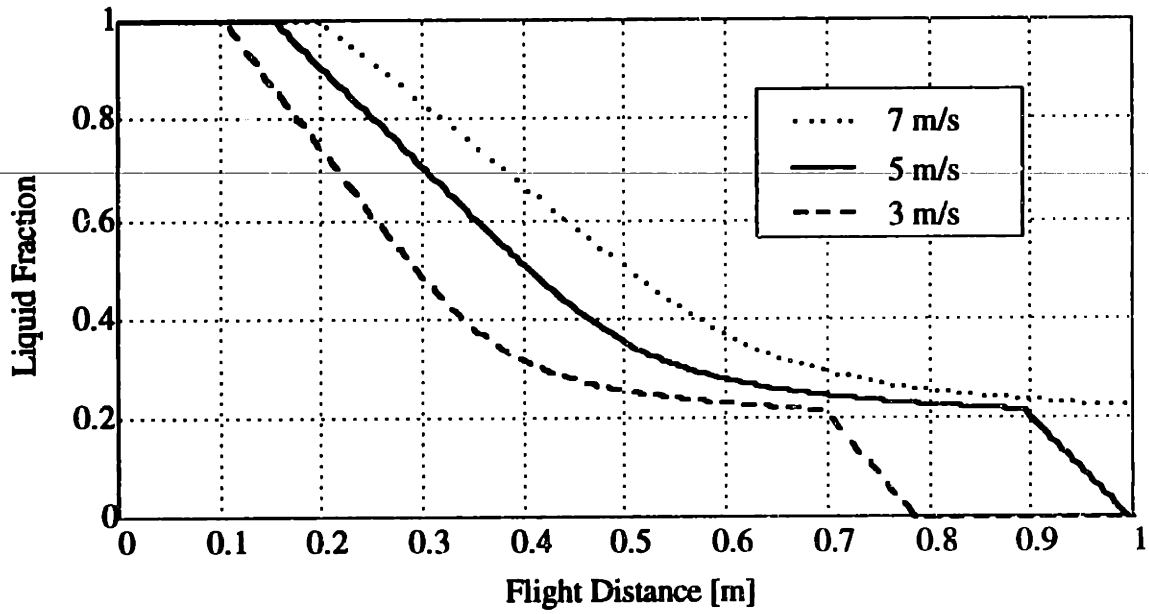

(b)

Figure 2.6 Results for the initial velocity effect study: (a) temperature vs. flight distance plot; (b) liquid fraction vs. flight distance plot. Droplets with a higher initial velocity appear to have a higher temperature and liquid fraction at a given flight distance due to less time spent in flight.

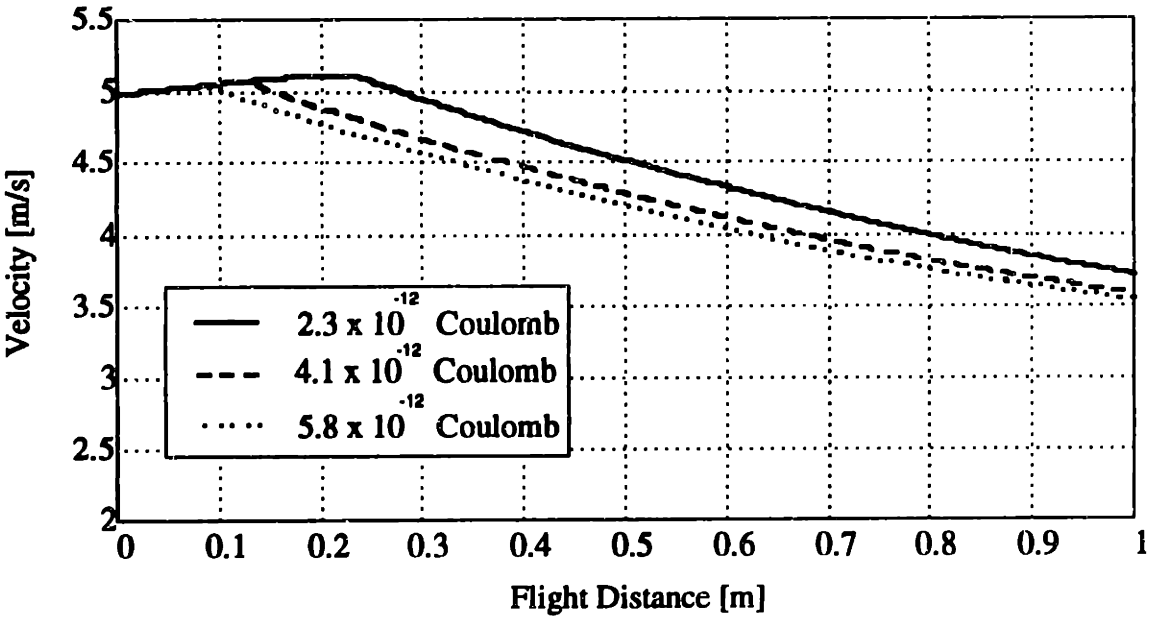

(a)

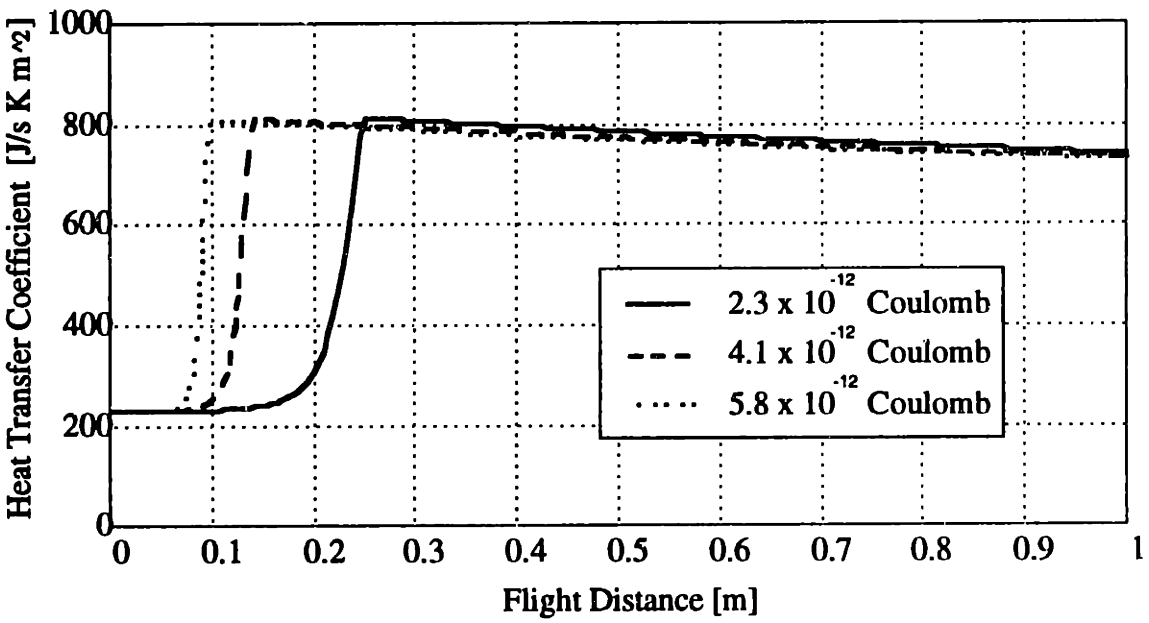

(b)

Figure 2.7 Results for droplet charge effect study: (a) velocity vs. flight distance plot; (b) heat transfer coefficient vs. flight distance plot. Droplet charge affects droplet velocities and heat transfer coefficients mainly by changing the spreading distance.

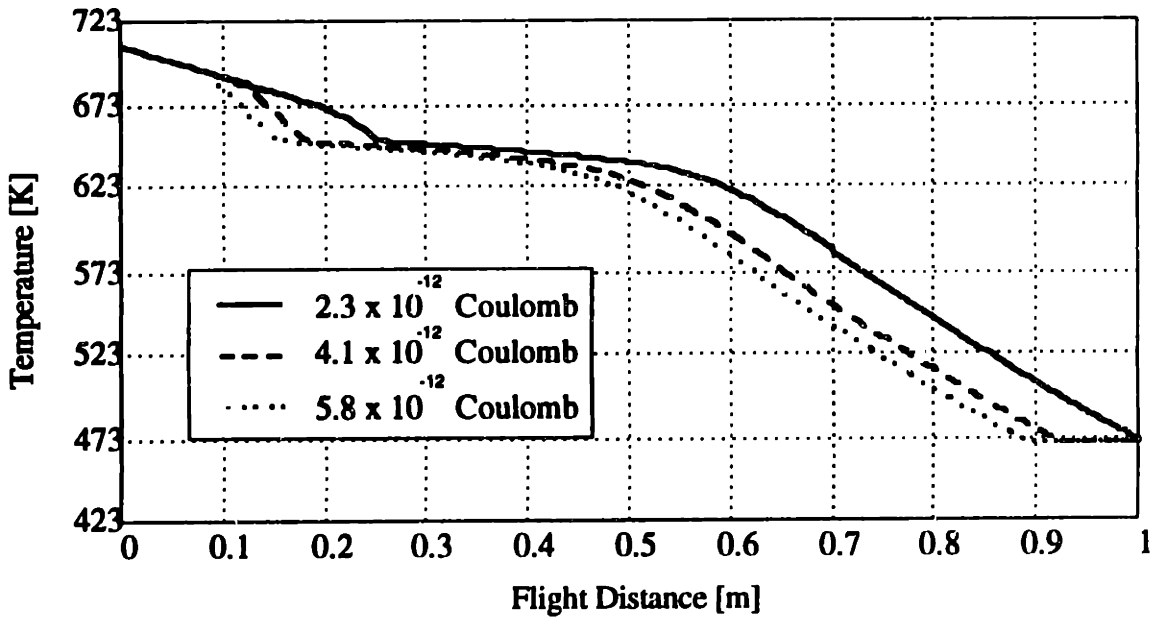

(a)

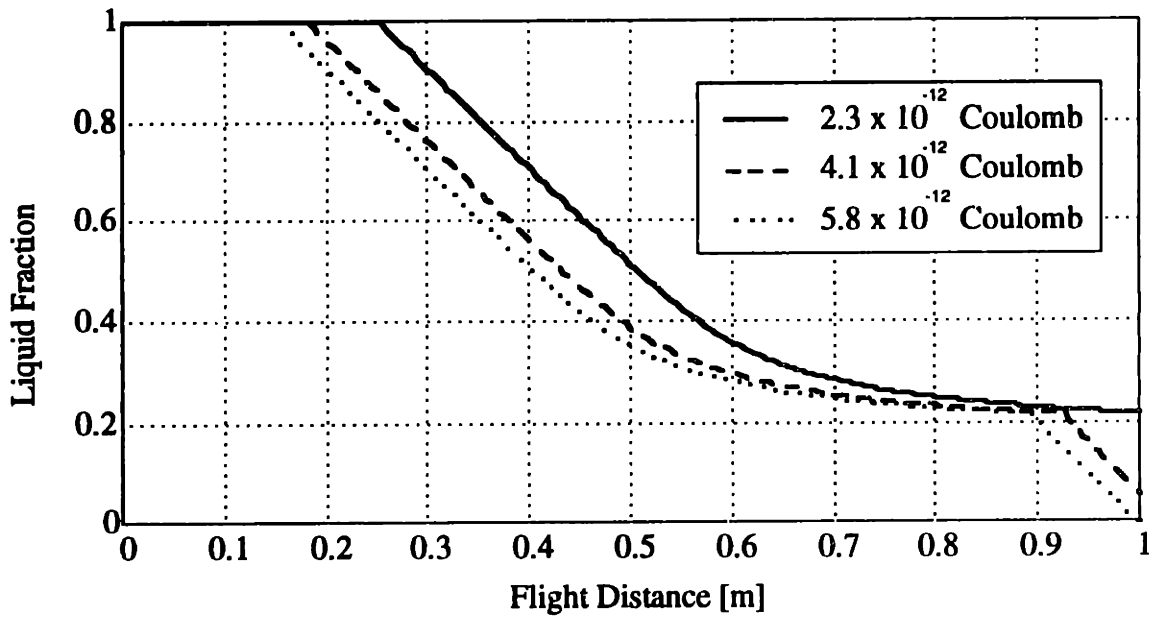

(b)

Figure 2.8 Results for the droplet charge effect study: (a) temperature vs. flight distance plot; (b) liquid fraction vs. flight distance plot. Droplets with a higher charge have a lower temperature and liquid fraction at a given flight distance due to earlier spreading.

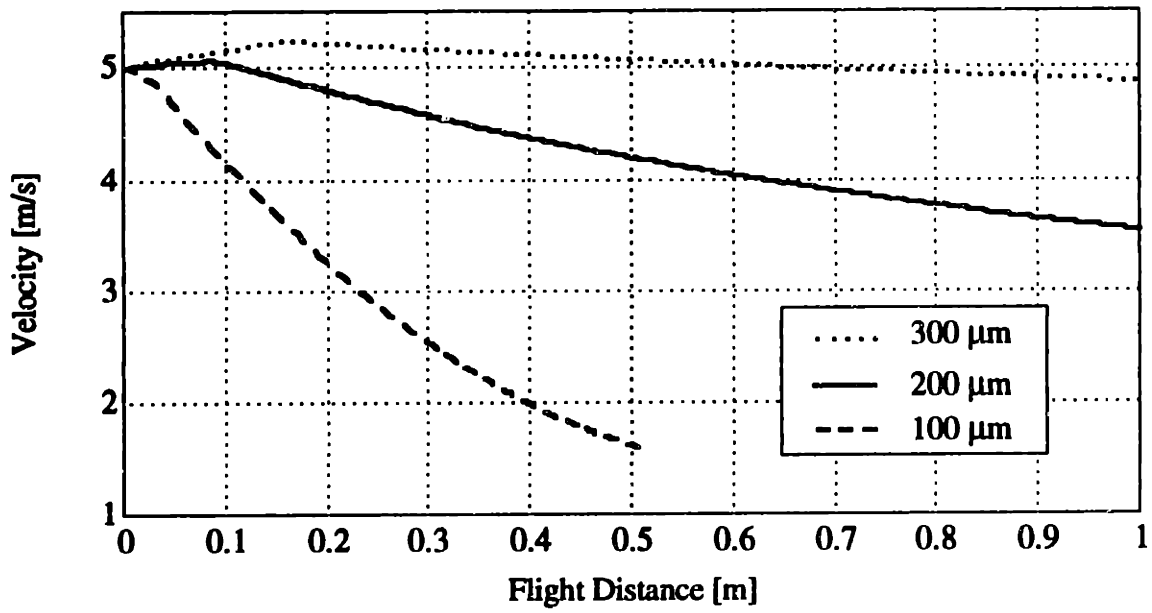

(a)

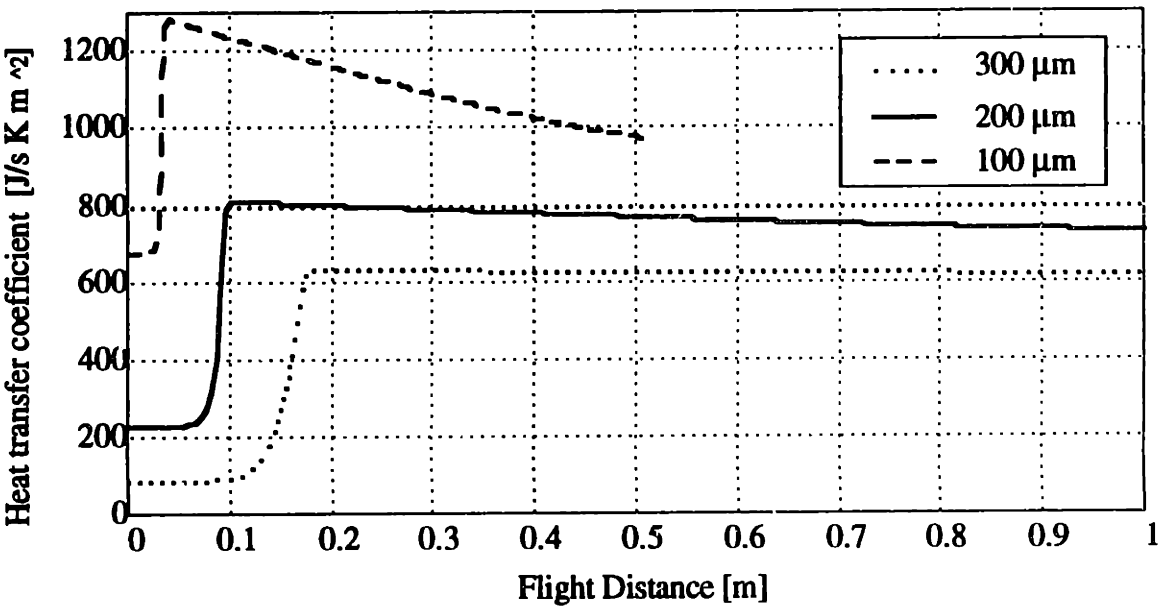

(b)

Figure 2.9 Results for droplet size effect study: (a) velocity vs. flight distance plot; (b) heat transfer coefficient vs. flight distance plot. Smaller droplets approach terminal velocities at a faster rate, spread out at a shorter distance, and have a much lower heat transfer coefficient.

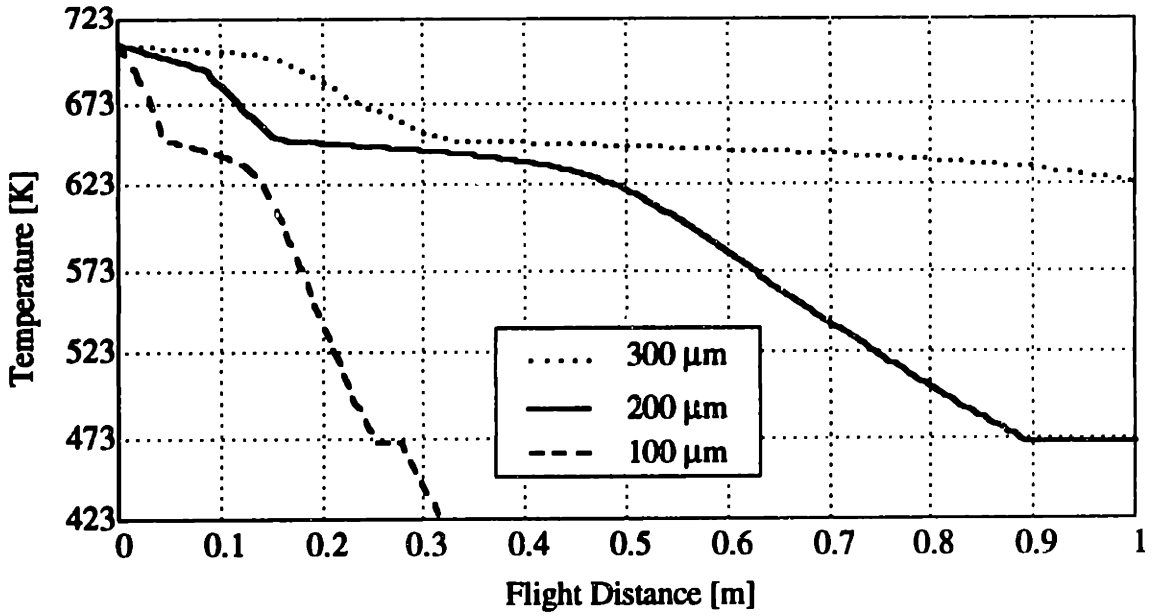

(a)

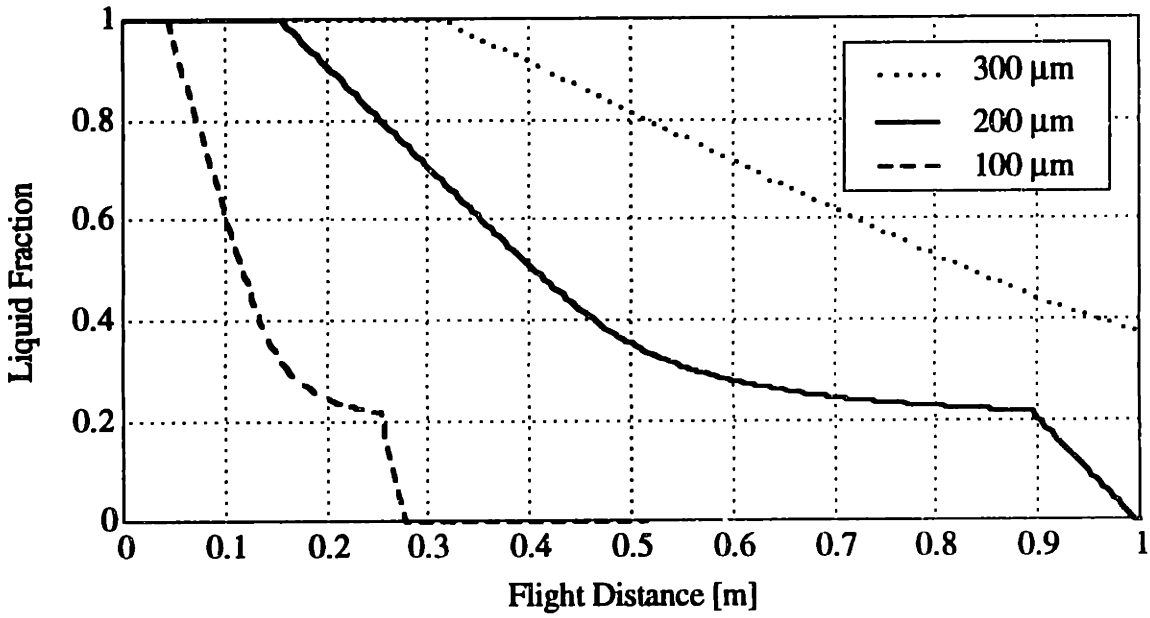

(b)

Figure 2.10 Results for the droplet size effect study: (a) temperature vs. flight distance plot; (b) liquid fraction vs. flight distance plot. Small droplets solidify at a faster rate due to a higher heat transfer coefficient and a higher area to volume ratio.

Chapter 3
Solidification of Droplets in Flight: Experimental Study

3.1 Introduction

The purpose of this experimental study is two-fold. The first is to demonstrate that the experimental methodology can be used to acquire useful information such as liquid fraction and morphology of solidified solids in the droplets. The second is to investigate the effects on droplet solidification of two important process parameters, the droplet size and the oxygen level in the chamber. Although other process parameters such as droplet velocity and droplet spreading in flight can also influence droplet solidification, their effects can be predicted by the droplet solidification model; therefore, they will not be studied here experimentally.

3.2 Experiment

Three set of experiments were conducted to study the effects of flight distance, droplet size, and oxygen level on droplet solidification. For the flight distance effect study, 288 and 181 μm droplets were collected at different flight distances. The droplet size effect study was carried out by using four different droplet sizes, namely 288, 245, 181, and 96 μm. The oxygen effect was studied with three oxygen concentrations, 5, 50, and 100 ppm.

3.2.1 Experimental Apparatus

Figure 3.1 shows the apparatus employed in this study. It consists of a droplet generation unit, a gas chamber unit, and a droplet collecting unit. The droplet generation unit is identical to that discussed in Section 2 of Chapter 1. The reader is directed there for a detailed description.

The gas chamber unit includes a glass chamber, a mechanical vacuum pump, a pure nitrogen tank, a second nitrogen tank with a known oxygen content, and an oxygen sensor.

By evacuating and backfilling the chamber with pure nitrogen several times, the oxygen level in the chamber can be reduced to that of the pure nitrogen tank. The second nitrogen tank can then be used for the final gas filling to control the oxygen level in the chamber. The oxygen sensor serves to monitor the oxygen level during the experiment.

The droplet collecting unit was designed to collect droplets at different droplet flight distances as shown in Figure 3.2. Nine collectors are placed onto a stainless steel shaft starting from the top with a spacing of 5 cm. The stainless shaft can be moved vertically to adjust the collecting distances. To avoid the blocking of lower collectors by upper collectors, the collectors are also separated twenty degrees from their neighbors. The base of each collector is an aluminum piece (25 mm x 20 mm x 2.5 mm). A thin smooth high-carbon steel piece (25 mm x 20 mm x 1 mm) is attached to each aluminum base as the collecting substrate. A quick full swing of the shaft while the spraying unit is on collects of droplets on each collector. The use of room temperature substrates allows for rapid quenching of the droplets. Due to the difference in the cooling rates, solids formed in flight and those formed upon quenching can be distinguished metallographically by microstructural analysis.

3.2.2 Materials

The material used for the experiment is a Zn-20 wt% Sn alloy. Utilizing the Zn-20 wt% Sn alloy greatly facilitates the identification of the solids formed prior to quenching. The first solidified phase, zinc, has zero solubility for tin under equilibrium conditions, thus no precipitation of tin in the solidified zinc phase will occur to cause confusion when the collected samples cool to room temperature. A Zn-Sn phase diagram is shown in Figure 3.3 for reference.

The alloy was prepared by melting 99.99% pure zinc and 99.99% pure tin in the atmosphere in a stainless steel crucible (diameter, 40 mm, height, 100 mm) coated with boron nitride. The molten alloy was well mixed by stirring before it solidified. The oxidized outer layer was removed by lathe turning. About 500 grams of Zn-20 wt% Sn

were produced from each melt. The resulting chunks of material were then cut into small pieces and cleaned with methanol.

3.2.3 Experimental Procedures and Conditions

For each experiment, about 300 grams of Zn-20 wt% Sn were placed in the boron nitride coated stainless-steel crucible for spraying. Every experiment started with evacuating the chamber to 20 Pa and backfilling it with pure nitrogen (impurity < 5 ppm) three times. The chamber was filled with either pure nitrogen or a controlled nitrogen-oxygen mixture, depending on the gas environment desired, after the forth purge. The chamber pressure was maintained at 11.7 kPa. The crucible was then heated to 708 K. After the melt temperature had been stabilized at 708 K for 15 minutes, the vibration frequency and charging voltage were adjusted and the crucible was pressurized to 158.5 kPa to start the spray. For the flight distance effect experiments, the spraying was kept on for 2 minutes for the temperature field in the gas chamber to reach a steady state. Droplet were then collected at various flight distances by quickly rotating the droplet collecting unit. Droplets were also collected in a stainless-steel cup filled with diffusion pump oil placed at the bottom of the chamber. The oil prevented significant deformation of partially solidified droplets. Droplets were only collected at the bottom of the chamber with an oil cup in the droplet size effect experiments and the oxygen effect experiments. A stainless steel cup close to the orifice was used to collect the spray to measure the jet flow rate for the jet velocity calculation.

The controlled experimental conditions used in the flight distance effect, droplet size effect, and oxygen effect studies are listed in Tables 3.1, 3.2, and 3.3, respectively.

3.2.4 Sample Preparation

The substrates from the flight distance effect experiments were carefully removed from the aluminum bases after each experiment. Thin plastic pieces with dimensions of 20 mm x 10 mm x 1 mm were used as the mounting bases for the collected droplets. A very thin

layer of epoxy was applied to the mounting bases to secure the splats. From each substrate, 6 splats were randomly chosen and mounted onto the plastic bases. The centers of the individual splats were aligned in a straight line parallel to the edge of the mounting base. The samples were examined using electron scanning microscopy to reveal the splat geometry and surface features. After microscopy, plastic bases with splats on them were mounted in cups using epoxy for transverse cross-section microstructure examination. These specimens were ground to the center using 320-, 400-, and 600-grit silicon carbide papers. A precise grind could be accomplished because their diameters had been measured from the SEM pictures, thus the depth to which to grind was known. Metadi fluid was used to prepare slurries for 0.3 μm alumina and 0.05 μm alumina for fine polishing since it had been found earlier that polishing with water stains the specimens. Final polishing used a mixture of Metadi fluid and 0.05 μm silicon carbide suspension.

The powders collected with the oil cup were cleaned with methanol after each experiment. The cleaned powders were then sprayed onto one side of a double-sided tape strip with the other side attached to a plastic base. The plastic base was then mounted in a cup using epoxy. The rest of the sample preparation procedures were the same as those for the quenched samples.

3.2.5 Microstructure Characterization and Image Analysis

An Electro Scan environmental SEM operated in the secondary electron mode was employed to reveal the surface morphology of the splats. A JOEL SEM operated in the backscattered electron mode was used to determine the cross-sectional microstructures of the splats. The samples subjected to the cross-sectional microstructure examination were unetched.

In order to determine the liquid fraction of the collected droplets prior to quenching, the cross-sectional micrographs of one typical splat from each sample were subjected to image analysis using the image analysis tool Image developed by NIH. Since the analysis was performed using high magnification micrographs, the entire cross-section of the splats may

be divided into several micrographs, depending on the size of the splats. A proper threshold was set for each analysis to single out the solids formed in flight. However, under a chosen threshold some spots that appear to be liquid in the micrographs were processed as solids. This problem was overcome by erasing the artifacts manually. Although the choice of a threshold is subjective, the errors for each analysis are estimated to be less than 5 percent.

3.3 Results

3.3.1 Results for Flight Distance Effect Study

As mentioned earlier, six splats were randomly picked from each substrate for microstructural examination since splats from the same substrate possess similar microstructure features. Only one splat from each sample is chosen for demonstration.

Low magnification SEM micrographs showing surface morphology and transverse cross-sections of the quenched 288 μm droplets from Experiment Q1 are presented in Figure 3.4 and 3.5 to reveal the degree of droplet solidification as a function of flight distance. As shown in these figures, the degree of solidification increases gradually with the flight distance. Figure 3.6 shows the higher magnification SEM micrographs for the droplet collected 0.35 m from the orifice. This figure shows that the splat has a smooth surface and that a rapidly solidified structure resulted from quenching. The higher magnification SEM micrographs for the droplet collected at 0.40 m are provided in Figure 3.7. Traces of solids formed prior to quenching can be seen from the surface morphology micrograph. The cross-section micrograph clearly shows that the zinc dendrites had just started to grow when the liquid portion was quenched to form a rapidly solidified structure. Figure 3.8 gives the higher magnification SEM micrographs for the droplet collected at 0.45 m. As shown in the figure, the zinc dendrites had grown larger and some of them were broken upon impact. Figure 3.9 shows the higher magnification SEM micrographs

for the droplet collected at 0.60 m, in which the growth of the zinc dendrites from the outer surface to the center is brought to light.

The calculated jet velocity of 5.08 m/s from the flow rate measurement was entered into the droplet solidification model for simulation. The results are plotted in Figure 3.10. The temperature vs. flight distance plot shows that the droplet cooling rate almost doubles when the droplet flight distance reaches 0.17 m. This phenomenon can be explained by droplet spreading resulting from electrostatic repulsion between droplets as described in the modeling section. The spreading distance was measured experimentally at 0.16 m, which agrees reasonably well with the simulation. The liquid fractions measured by image analysis are plotted in Figure 3.10 for comparison. The measurements follow the simulation closely except for the first two data points. The discrepancy is probably caused by a small undercooling of the droplets.

Figures 3.11 and 3.12 show the surface morphology and cross-section of the collected 181 μm droplets from Experiment Q2 at low magnification. As shown in these figures, droplets collected at 0.15 m, 0.20 m, and 0.25 m appear to have the same deformation pattern, while a sudden change in the deformation pattern is found for the droplets collected at 0.30 m. Droplets collected at 0.35 m and 0.40 m seem to have such a high degree of solidification that they hardly deformed. Droplets collected after 0.40 m preserve their spherical shape and show no difference in microstructure from those collected at 0.40 m, therefore they are not presented here. Higher magnification SEM micrographs for the droplet collected at 0.25 m are provided in Figure 3.13. The cross-sectional microstructure displays the rapidly solidified structure. No trace of solids formed prior to quenching is observed. Figure 3.14 shows the higher magnification micrograph for the droplet collected at 0.30 m. In these micrographs, solids formed at different times can be differentiated by their distinct microstructures. The solids formed upon quenching have a rapidly solidified structure, while the solids formed before quenching have a rapidly solidified cellular structure accompanied by dendritic structures. Growth centers for the cellular structures

can be identified in some droplets. From observation, it is believed that the latter droplets experienced a high degree of undercooling before nucleation took place. The high undercooling led to rapid solidification of the droplets with the cellular structure solidified during recalescence and the dendritic structures after recalescence. The recalescence is believed to occur slightly before the droplets reached 0.30 m, reasoned by the fact that only a small portion of the dendritic structure had been solidified prior to impact. Figure 3.15 shows the continued growth of the dendritic structure for the droplet collected at 0.35 m.

A jet velocity calculated at 4.41 m/s from the flow rate measurement was input to the droplet solidification model for simulation. The results are plotted in Figure 3.16. In the temperature vs. flight distance plot, simulations with and without undercooling are both shown. The undercooling behavior was simulated by forcing the droplets to remain in the liquid phase. The simulation was stopped when the flight distance reached 0.30 m since it is found experimentally that droplets nucleated at about 0.3 m. From the plot, the droplets are estimated to have 110 K of undercooling.

3.3.2 Results for Droplet Size Effect Study

Forty powder particles from each experiment were randomly selected for microstructure examination. The liquid droplet size for each experiment converted from the measured powder size is listed in Table 3.4 together with the percentage of undercooled droplets. Figures 3.17 to 3.20 show the representative cross-sectional micrographs for these experiments. As shown in Figure 3.17, the 288 μm droplet experienced no or slight undercooling. The structure is dendritic and the nucleation took place on the droplet surface. For 245 μm droplets, three types of microstructures are observed. Figure 3.18(a) shows the first type of microstructure pertaining to a slightly or not undercooled 245 μm droplet. This microstructure is similar to that of 288 μm droplets. Figure 3.18(b) shows the second type of microstructure characterized by a cellular structure nucleated within the droplet and dendritic structures solidified after recalescence. Some dendrites seem to be the continuation of the cellular structure while some appear to grow from the droplet surface.

About 87% of undercooled 245 μm droplets belong to this category. Figure 3.18(c) shows the third type of microstructure as defined by a cellular structure nucleated on the droplet surface and dendritic structures solidified after recalescence. About 13% of undercooled 245 μm droplets fall into this category. Figure 3.19 shows the microstructure of an undercooled, internally nucleated 181 μm droplet. The percentage of the cellular structure is higher than that for the 245 μm droplet. All 181 μm droplets examined have such a microstructure. Figure 3.20 shows the microstructure of a highly undercooled, internally nucleated 96 μm droplet. Compared to the 181 μm droplets, the percentage of the cellular structure increases and the sizes of cells and dendrites decreases.

3.3.3 Results for Oxygen Effect Study

For the three experiments performed with oxygen concentrations maintained at 5, 50, and 100 ppm, no significant difference in cross-sectioned microstructures can be noticed, although some droplets collected in the 100 ppm experiment were darkened apparently from oxidation. Basically, the droplets were undercooled and internally nucleated. The microstructures are characterized by a cellular structure accompanied by dendritic structures.

3.4 Discussion

3.4.1 Nucleation Kinetics and Droplet Solidification

The droplet size effect study indicates that the population of undercooled droplets, the degree of undercooling, and the tendency to nucleate internally increase as the droplet size decreases. These phenomena can be explained by the kinetic competition among different catalysts for nucleation. According to classical theory, the heterogeneous nucleation rate, J_a, can be represented as [37]:

$$J_a = \Omega_a \exp(-\Delta G^* / kT) \qquad (3.1)$$

where Ω_a is a prefactor proportional to both the number of liquid atoms in contact with the unit area of the catalytic surface and to the atomic jump frequency, ΔG^* is the activation barrier for nucleation, k is Boltzmann's constant, and T is the temperature. The activation barrier, ΔG^*, is given in general by:

$$\Delta G^* = b\,\sigma_{XL}^3\, f(\theta) / \Delta G_v^2 \tag{3.2}$$

where b is a geometrical factor, σ_{XL} is the crystal/liquid interfacial energy, $f(\theta)$ is a function of contact angle θ, and ΔG_v is the driving free energy for nucleation per unit volume of product phase. For a given type of nucleation kinetics, the critical condition to observe nucleation in time t in a droplet with catalytic surface area a is given by :

$$J_a a\, t \approx 1 \tag{3.3}$$

Therefore, the time for the onset of nucleation can be written as [38]:

$$\ln t = -\ln \{\Omega_a a\} + b\,\sigma_{XL}^3\, f(\theta) / (\Delta G_v^2\, k\, T) \tag{3.4}$$

Based on the above equation, a transformation diagram illustrating nucleation kinetics is schematically shown in Figure 3.21, where curves A and B represent two possible types of nucleation catalysts with A being a catalyst more potent than B. Notice that the shapes of these curves are determined by the geometrical factor b, the crystal/liquid interfacial energy σ_{XL}, the functional form of contact angle $f(\theta)$, and the driving free energy for nucleation ΔG_v. The position of the curves in the horizontal direction is dictated by the catalytic surface area a. As shown in Figure 3.21, fast cooling forces nucleation to take place on the less potent nucleation catalysts.

Since two nucleation patterns, internal nucleation and surface nucleation, are observed in the droplet size effect study, at least two types of nucleation catalysts should be present in the droplets, that is, the internal catalysts and the surface catalysts. If the internal catalysts are more potent than those on the surface, more internally nucleated droplets should be found when the droplet size increases because more internal catalysts are included. This apparently contradicts experimental observation. Therefore, the surface nucleation catalysts should have a higher potency than the internal ones. This, however, does not account for the undercooling and internal nucleation phenomena occurring in the smaller droplets. The averaged cooling rate and the surface area for each droplet size studied are listed in Table 3.4. In light of this information, the schematic diagram shown in Figure 3.22 can explain the undercooling and internal nucleation phenomena. The cooling curve, the transformation curve representing internal nucleation, and the curve representing surface nucleation for a 181 μm droplet are indicated by $\dot{T}_1$, I_1, and S_1, respectively. Due to fast cooling, internal nucleation is selected and large undercooling occurs despite the fact that the surface nucleation catalysts are more potent than the internal ones. For a 288 μm droplet, the cooling curve, the transformation curve representing internal nucleation, and the curve representing surface nucleation are indicated by $\dot{T}_2$, I_2, and S_2, respectively. Notice that curve S_2 has the same shape as S_1 but is shifted to the left because of a larger catalytic area as predicted by Equation 3.4. Curve I_2 is also moved to the left because more internal catalysts are included for the larger droplets. The shift of the transformation curve representing internal nucleation and slower cooling combine to cause the 288 μm droplets to nucleate on the surface with slight or no undercooling. The same reasoning can be applied to explain why some 245 μm droplets are undercooled while some are not as well as why some undercooled droplets nucleate internally while some do not. The cooling rate for the 245 μm droplets is believed to lie at a critical point, at which a slight variation in the cooling rate will lead to a change in the type of the nucleation catalysts. This explains the concurrent existence of internally nucleated and surface nucleated droplets. On the other

hand, the difference in the amount of undercooling in these droplets can be accounted for by the combination of the change in the cooling rate and the shift of the transformation curve representing surface nucleation. The curve may shift since the droplet surface area does not necessarily equal the catalytic surface area for nucleation and variation in the catalytic surface area are possible.

Other factors which might have induced the phenomena described above are also investigated. Two are a possible temperature gradient in the droplets and the late onset of oxide formation. The Biot number of the largest droplet size, 288 μm, is calculated at 0.016, which is much smaller than the critical value 0.1; therefore, a temperature gradient before nucleation did not likely exist in the 288 μm droplets and thus, the surface nucleation was not caused by a temperature gradient. The surface nucleation observed for 288 μm droplets could have been catalyzed by surface oxides. However, if the smaller droplets nucleated internally because surface oxides could not form in time for nucleation due to fast cooling, increasing the oxygen concentration in the environment should increase the likelihood of surface nucleation. This does not agree with the results of the oxygen effect study. Consequently, the late onset of oxide formation cannot be responsible for the internal nucleation of the smaller droplets.

3.5 Conclusions

(1) The droplet intercepting technique developed in this study successfully determined the liquid fractions and microstructures of the 288 μm Zn-20 wt% Sn droplets collected at various flight distances. This technique also effectively determined the degree of undercooling of the 181 μm Zn-20 wt% Sn droplets.

(2) The flight distance effect study shows that the droplet thermal model accurately predicted the liquid fraction of 288 μm Zn-20 wt% Sn droplets at various flight distances, in which case no apparent undercooling occurred. On the contrary, the droplet thermal

model failed to predict the liquid fraction of 181 Zn-20 wt% Sn droplets because undercooling resulted in this case.

(3) The degree of droplet undercooling is a strong function of droplet size, i.e., the cooling rate. In general, small droplets will experience undercooling and large droplets will not. Droplets of intermediate size tend to have non-uniform undercooling behavior: some droplets will experience undercooling and some will not. For those undercooled droplets, the degree of undercooling may vary.

(4) Nucleation kinetics succeed in explaining qualitatively the undercooling and nucleation behavior of the droplets in this study, that is, why 288 μm Zn-20 wt% Sn droplets nucleated on the surface while 181 and 96 μm Zn-20 wt% Sn droplets nucleated inside and why non-uniform undercooling behavior occurred to 245 μm Zn-20 wt% Sn droplets. However, a quantitative explanation is difficult because the nucleation catalysts are unknown and the physical parameters used in the heterogeneous nucleation theory are not easy to determine.

(5) The concentration of oxygen is found to have no significant effect on the droplet solidification in this study. However, since the lowest oxygen concentration used in the study was 5 ppm it is not known how an oxygen-free environment could change the droplet solidification. Oxygen concentration may affect droplet solidification of other alloys differently. This, however, will need further investigation.

Table 3.1 Experimental conditions for flight distance effect experiments.

	Exp. Q1	Exp. Q2
Orifice size (μm)	150	100
Liquid droplet size (μm)	288	181
Driving pressure (kPa)	137.8	137.8
Perturbation frequency (kHz)	7.15	11.1
Oxygen level (ppm)	5	5
Charging field strength (V/mm)	222	200
First collector distance (m)	0.35	0.15

Table 3.2 Experimental conditions for droplet size effect experiments.

	Exp. D1	Exp. D2	Exp. D3	Exp. D4
Orifice size (μm)	150	125	100	45
Liquid droplet size (μm)	288	245	181	96
Driving pressure (kPa)	137.8	137.8	137.8	137.8
Perturbation frequency (kHz)	7.15	9.0	11.0	22.0
Oxygen level (ppm)	10	10	10	10
Charging field strength (V/mm)	200	200	200	200

Table 3.3 Experimental conditions for oxygen effect experiments.

	Exp. O1	Exp. O2	Exp. O3
Orifice size (μm)	100	100	100
Liquid droplet size (μm)	181	181	181
Driving pressure (kPa)	137.8	137.8	137.8
Perturbation frequency (kHz)	11.1	11.1	11.1
Oxygen level (ppm)	5	50	100
Charging field strength (V/mm)	200	200	200

Table 3.4 Liquid droplet size and percentage of undercooled droplets for droplet size effect experiments.

	Exp. D1	Exp. D2	Exp. D3	Exp. D4
Orifice size (μm)	150	125	100	45
Liquid droplet size (μm)	288	245	181	96
Percentage of undercooled droplets	0	72	100	100

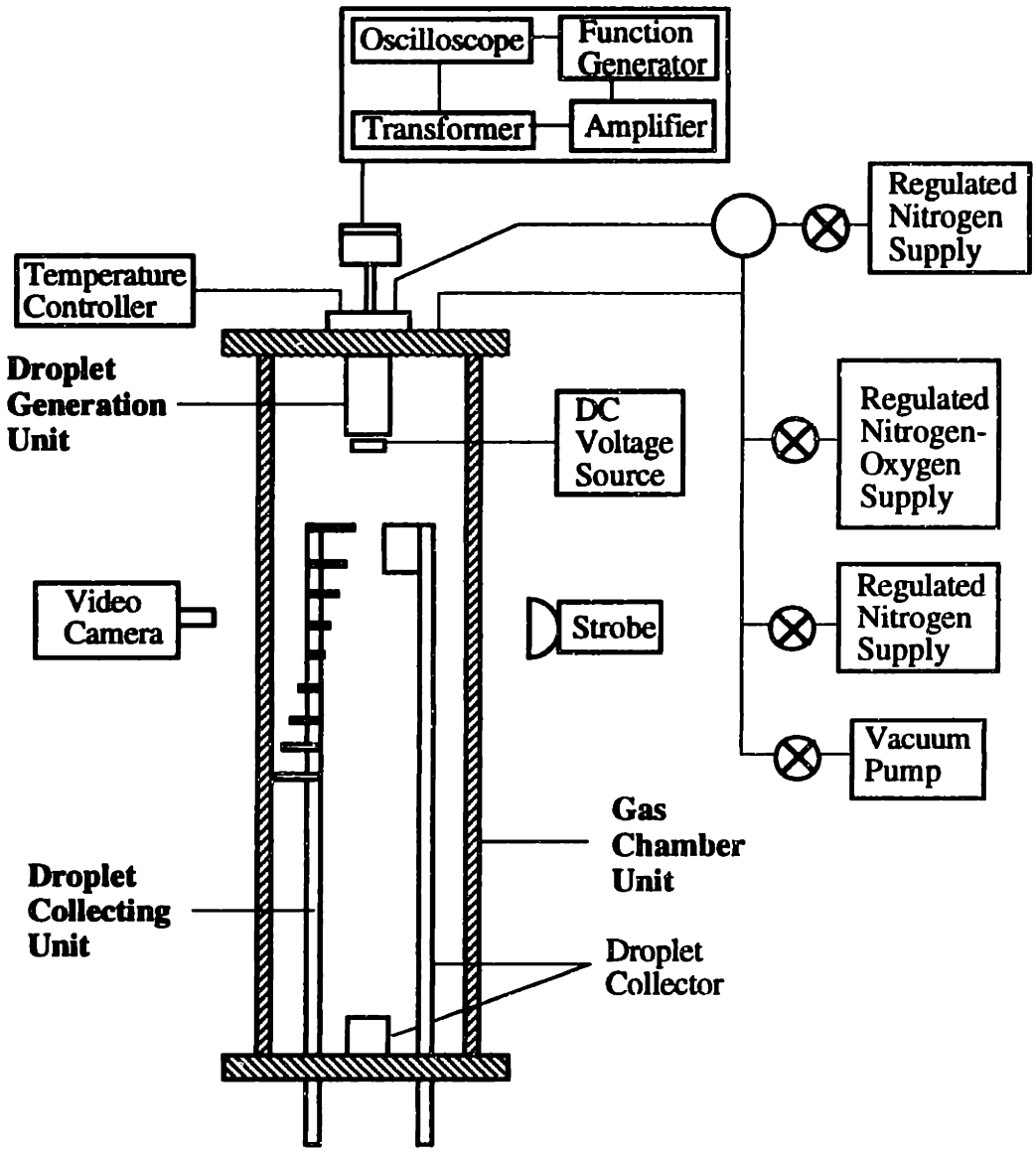

Figure 3.1 Experimental apparatus.

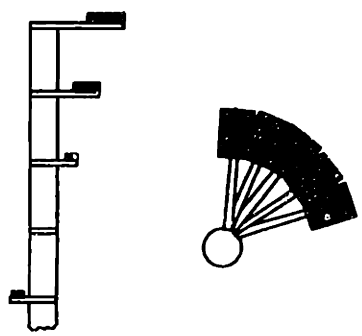

Side view Top view

Figure 3.2 Droplet collecting unit.

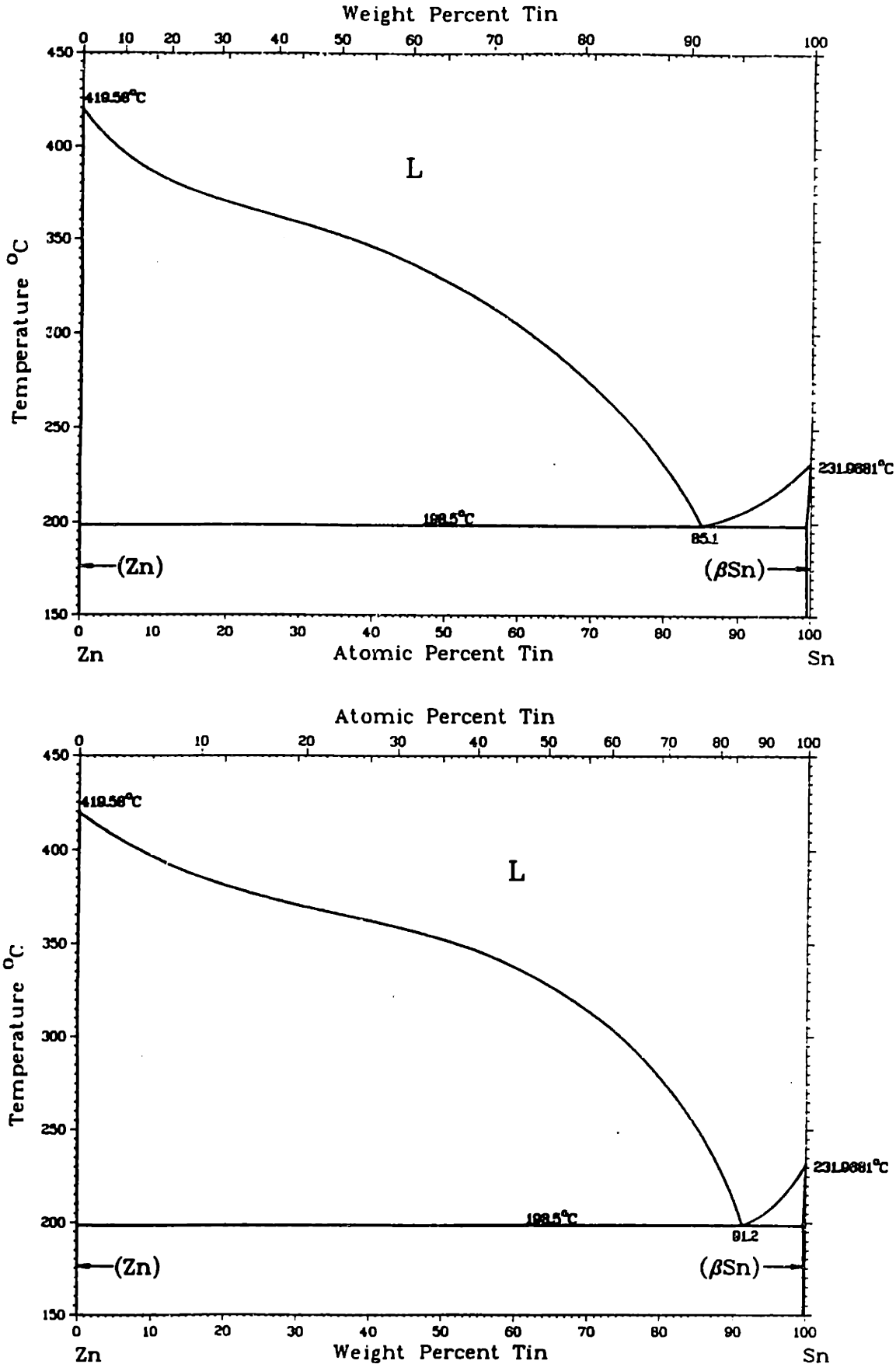

Figure 3.3 Zn-Sn phase diagram.

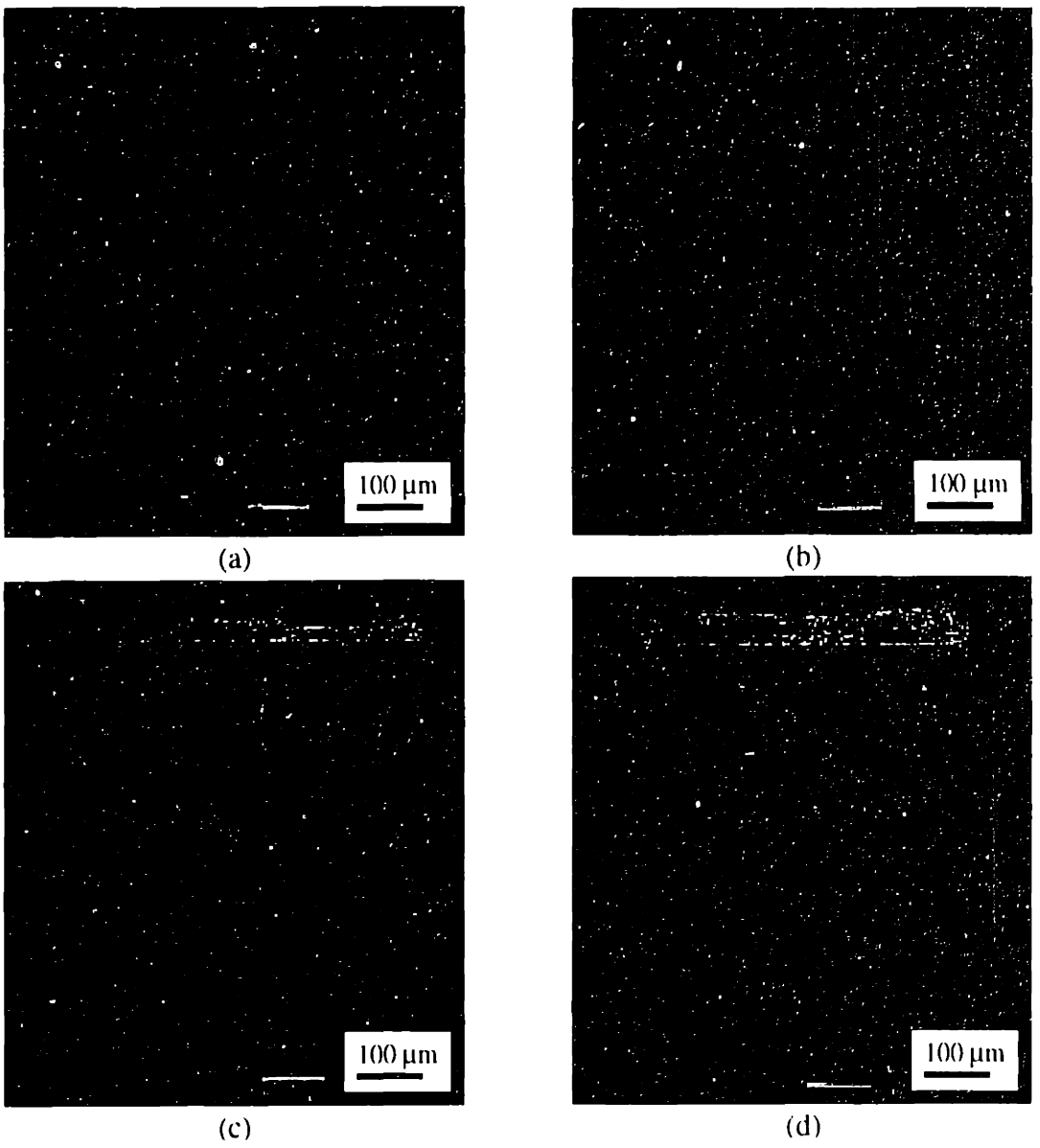

Figure 3.4 Low magnification micrographs showing surface morphology and cross-sectioned microstructures for the splats collected in Experiment Q1. The flight distances are: (a) 0.30 m; (b) 0.35 m; (c) 0.40 m; and (d) 0.45 m.

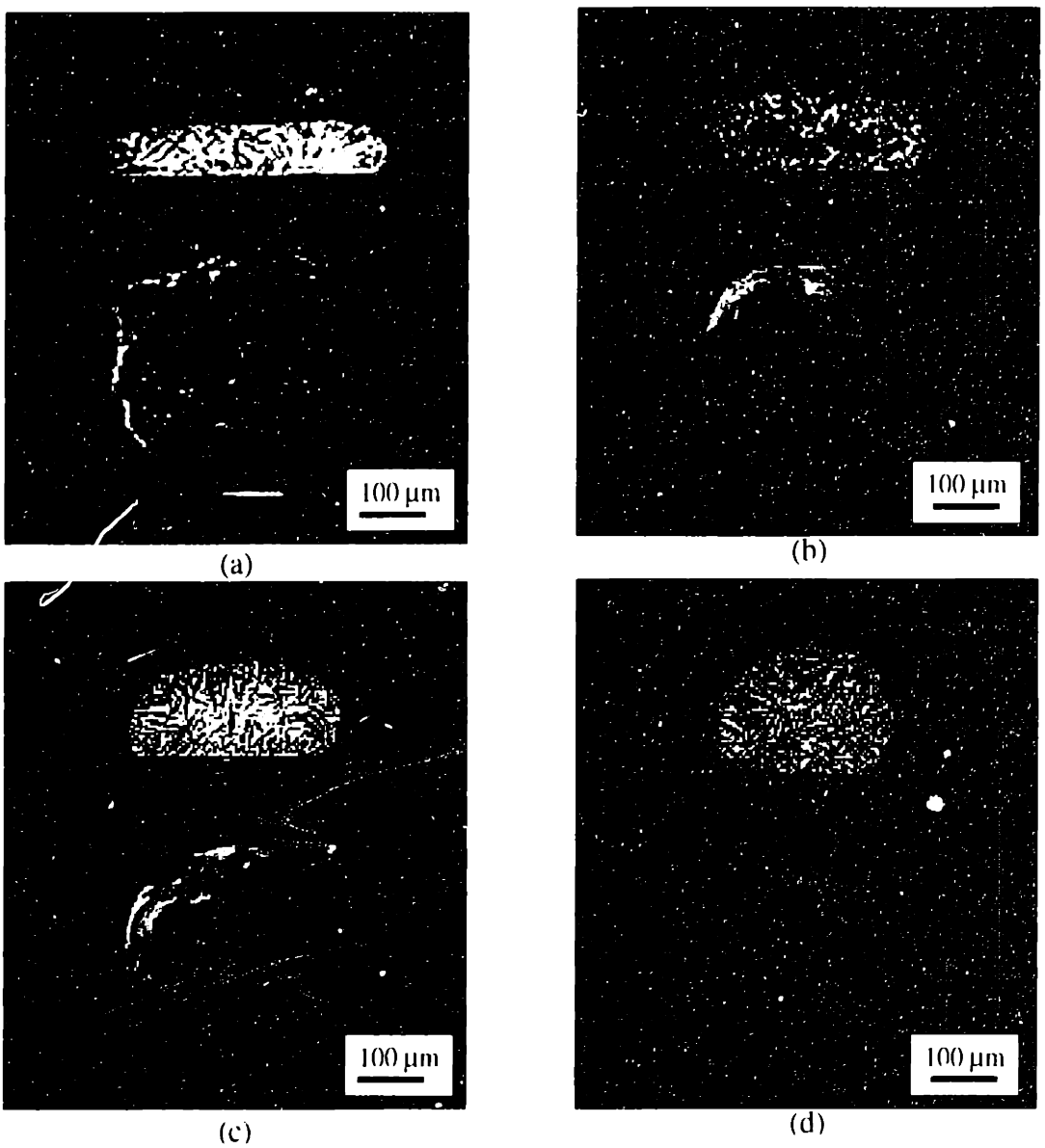

Figure 3.5 Low magnification micrographs showing surface morphology and cross-sectioned microstructures for the splats collected in Experiment Q1. The flight distances are: (a) 0.50 m; (b) 0.55 m; (c) 0.60m; and (d) 0.65 m.

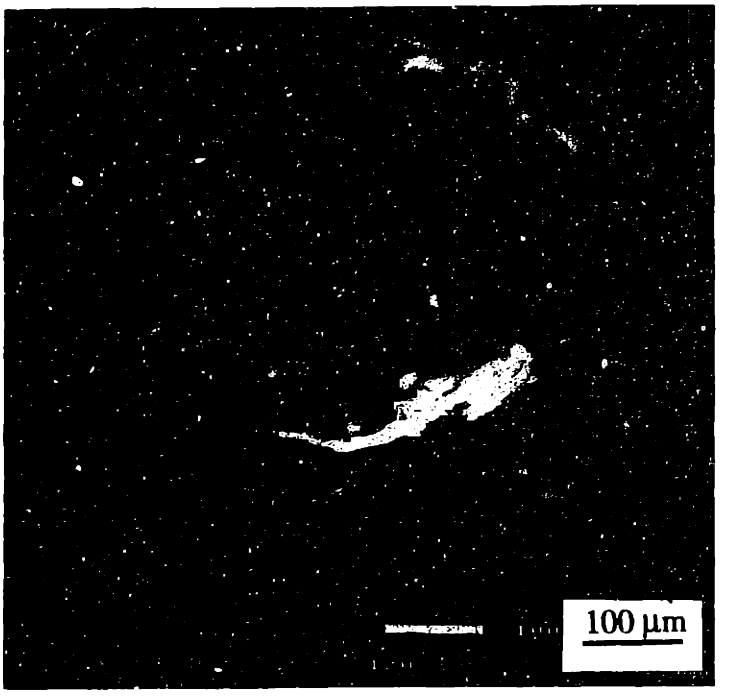

(a)

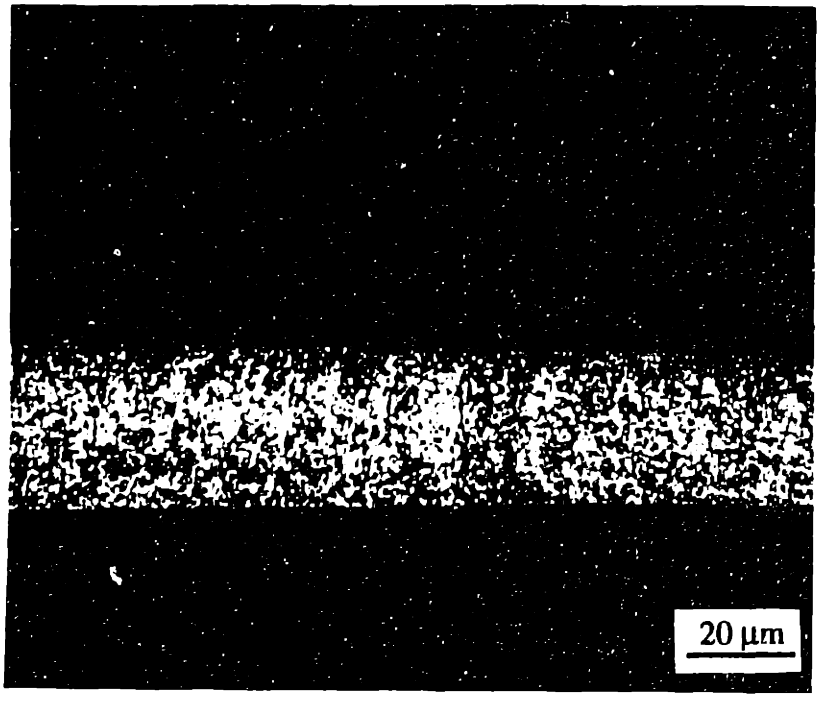

(b)

Figure 3.6 Micrographs for the droplet collected at 0.35 m: (a) surface morphology; and (b) cross-sectioned microstructure. No traces of solids formed prior to impact are observed.

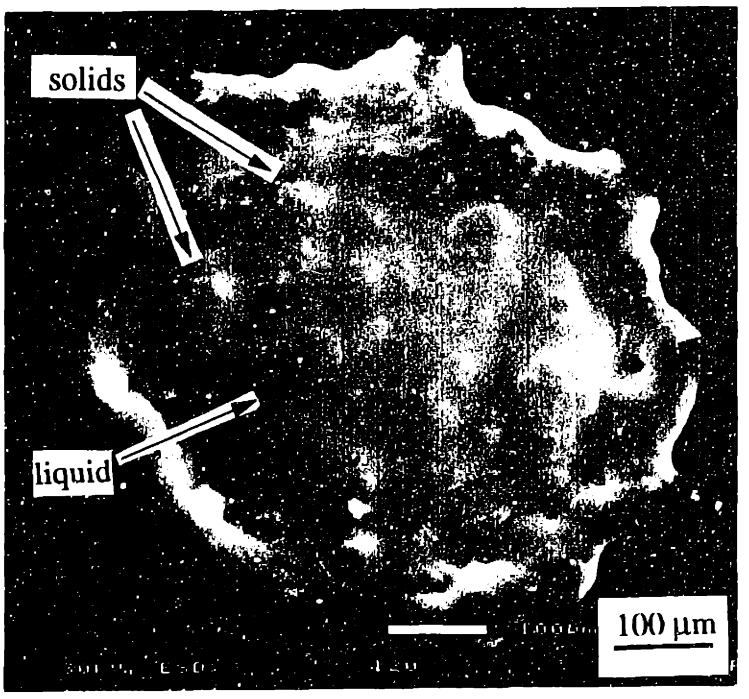

(a)

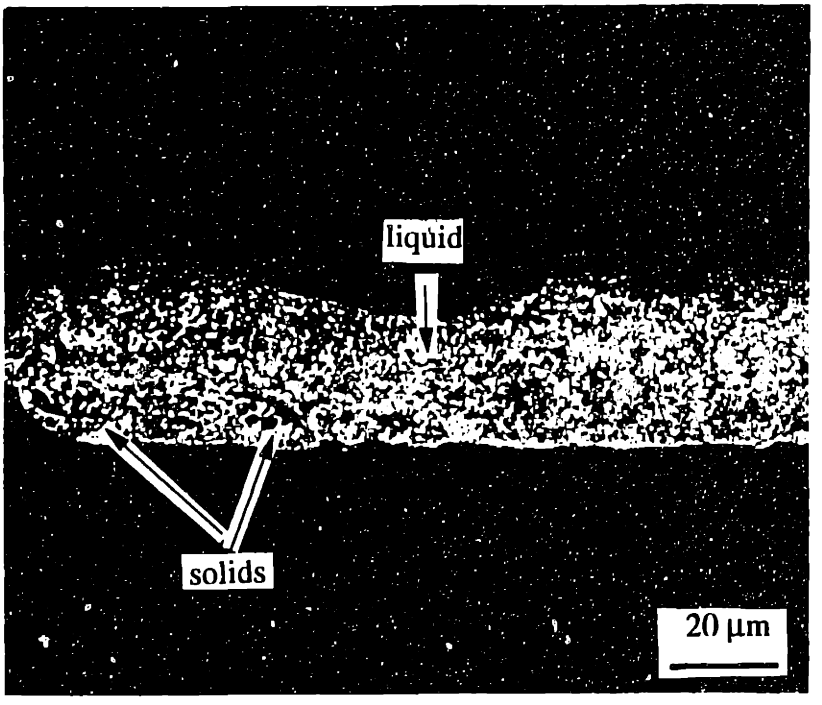

(b)

Figure 3.7 Micrographs for the droplet collected at 0.40 m: (a) surface morphology, and (b) cross-sectioned microstructure. The arrows indicate the liquid portion and solids prior to quenching.

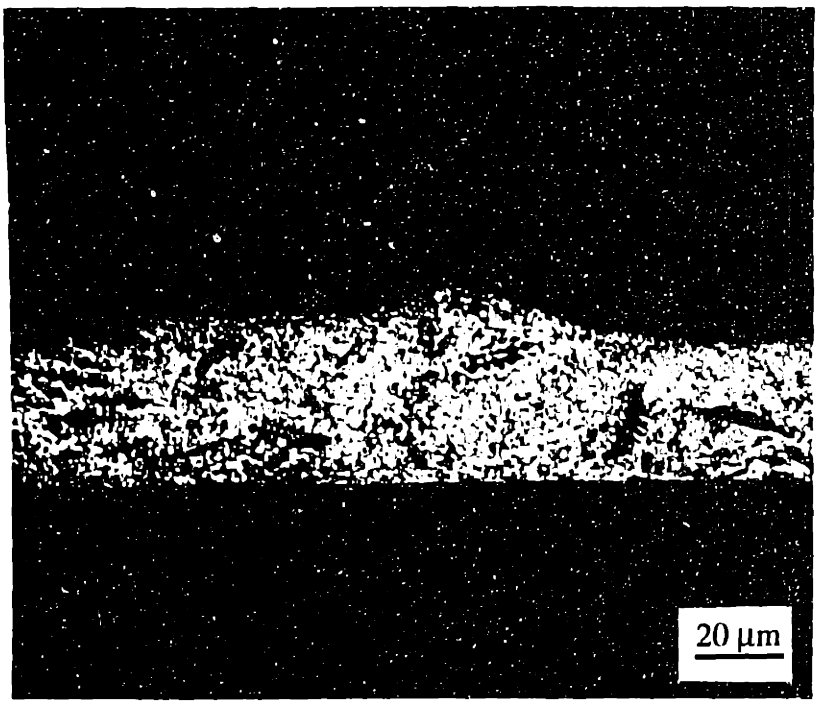

Figure 3.8 Cross-section micrograph for the droplet collected at 0.45 m. Compared to the droplet collected at 0.40 m, the portion of solids formed prior to impact has increased.

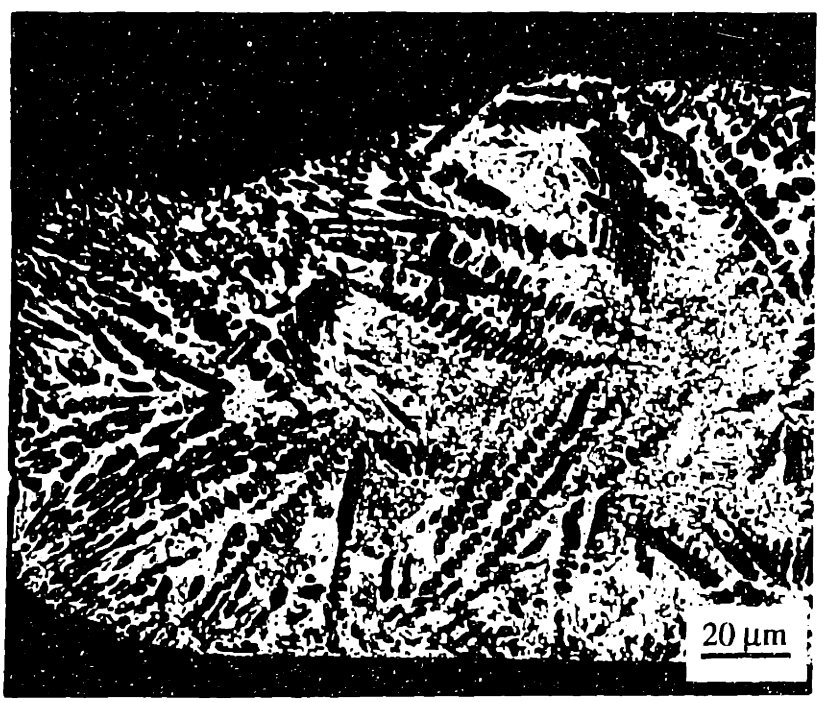

Figure 3.9 Cross-section micrograph for the droplet collected at 0.60 m. More solids solidified prior to impact are observed.

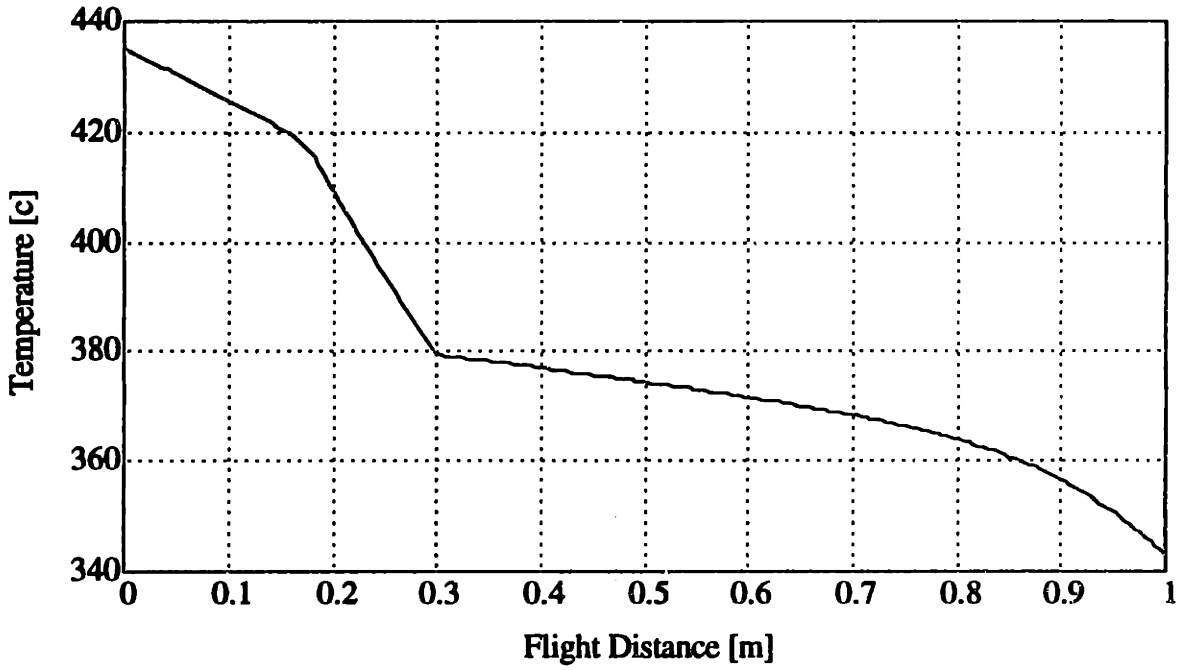

(a)

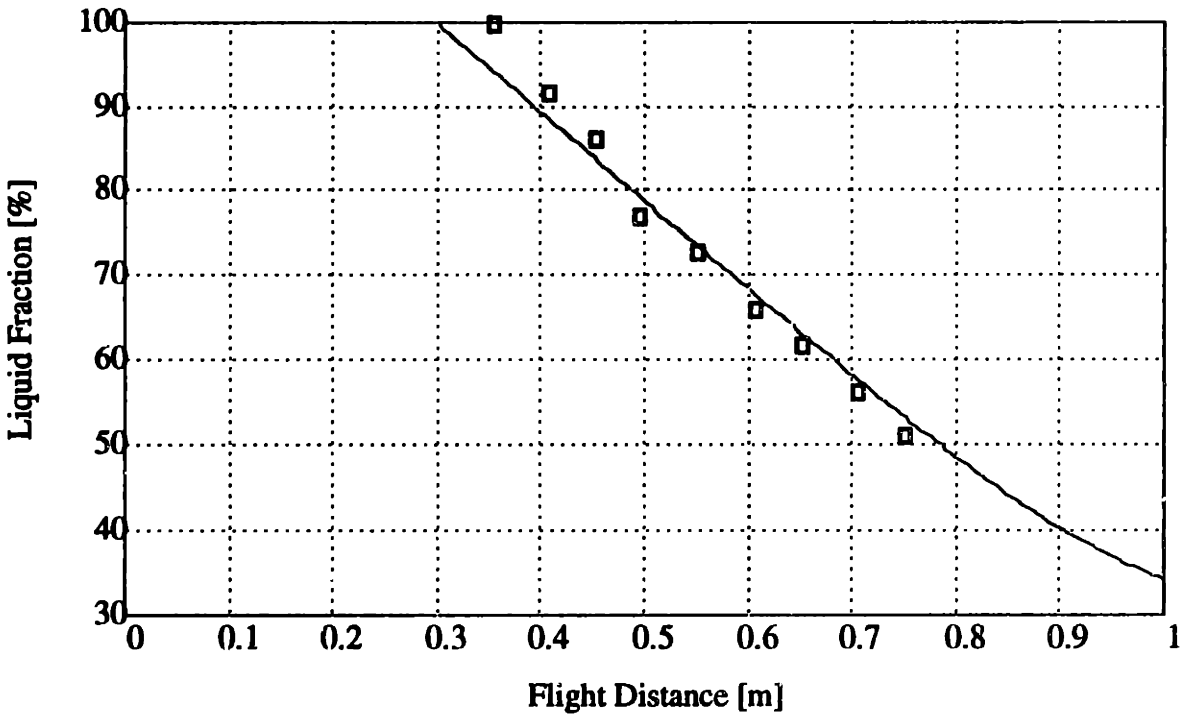

(b)

Figure 3.10 Simulation and experimental results for 288 μm droplet solidification: (a) calculated temperature vs. flight distance plot; and (b) calculated and experimental liquid fraction vs. flight distance plot. The squares represent the measured liquid fraction.

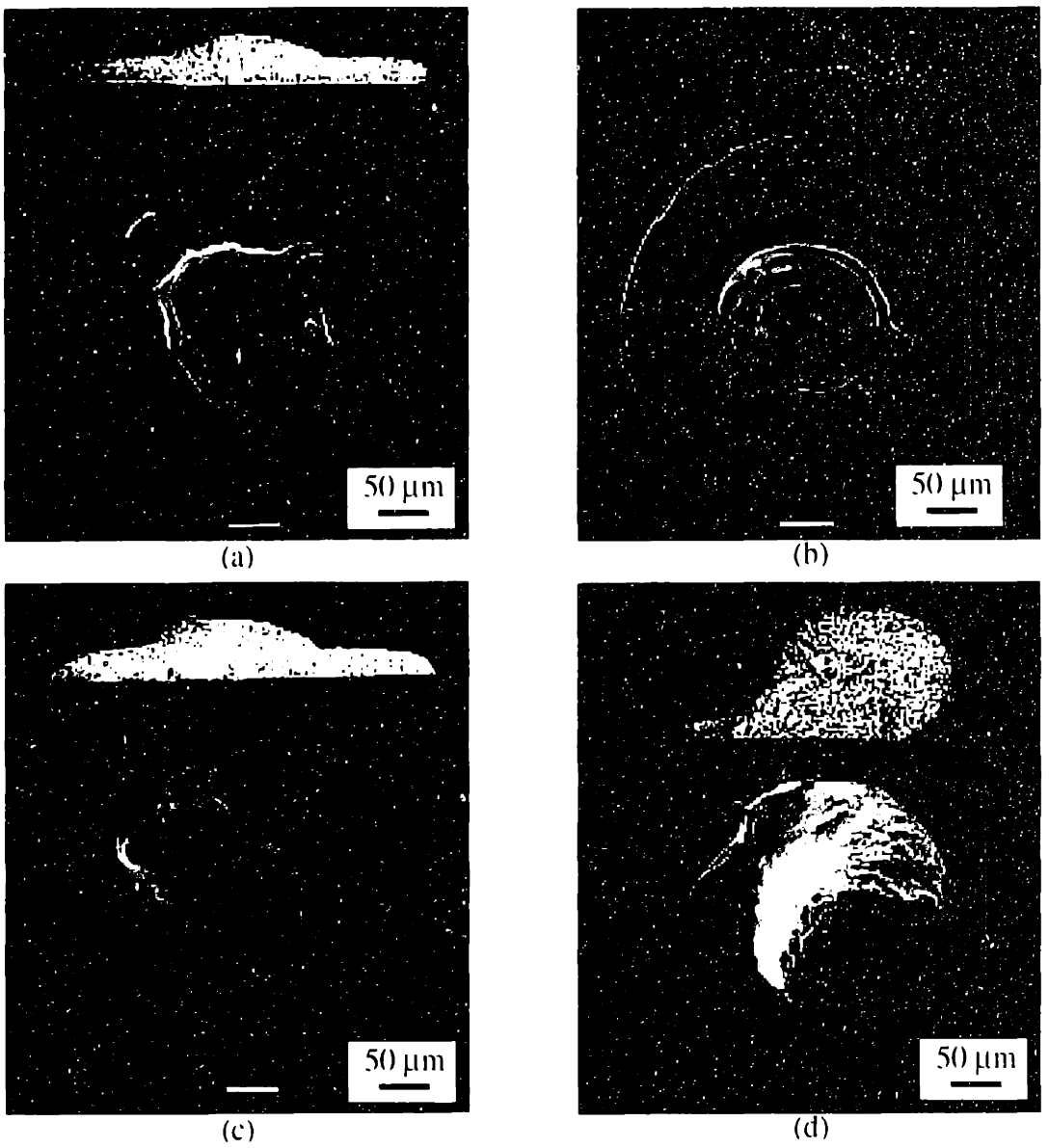

Figure 3.11 Low magnification micrographs showing surface morphology and cross-sectioned microstructures for the splats collected in Experiment Q2. The flight distances are: (a) 0.15 m; (b) 0.20 m; (c) 0.25m; and (d) 0.30 m.

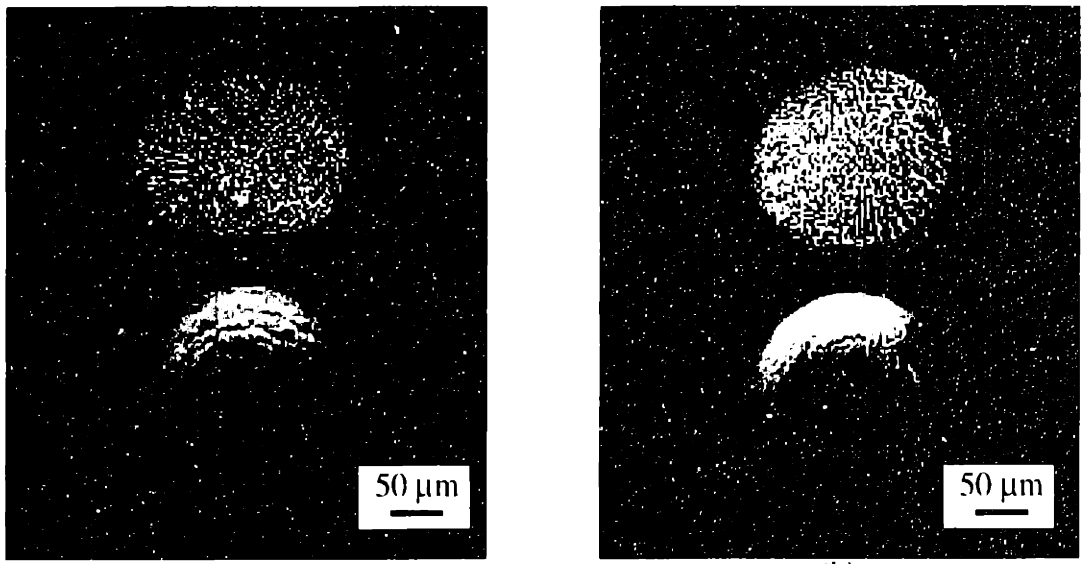

(a) (b)

Figure 3.12 Low magnification micrographs showing surface morphology and cross-sectioned microstructures for the splats collected in Experiment Q2. The flight distances are: (a) 0.35 m; and (b) 0.40 m.

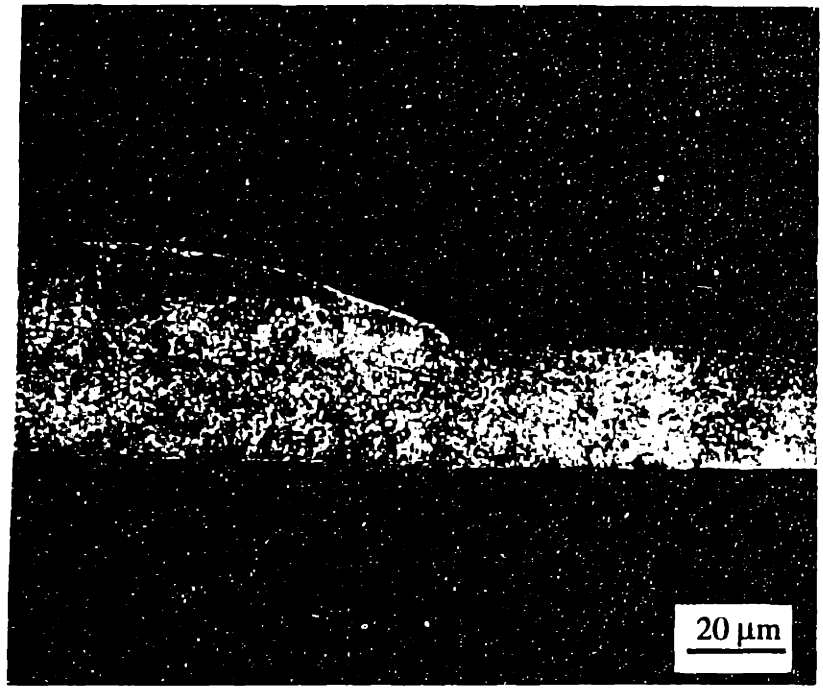

Figure 3.13 Cross-section micrograph for the droplet collected at 0.25 m. The solids formed upon quenching have a rapidly solidified structure as seen at lower left portion of the droplet.

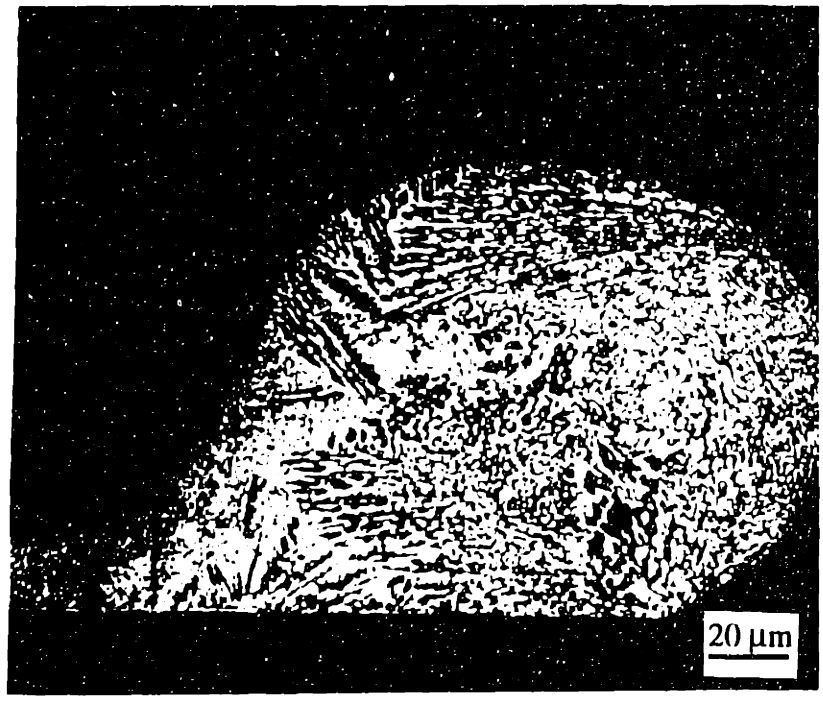

Figure 3.14 Cross-section micrograph for the droplet collected at 0.30 m. A large portion of the droplet soldified prior to impact.

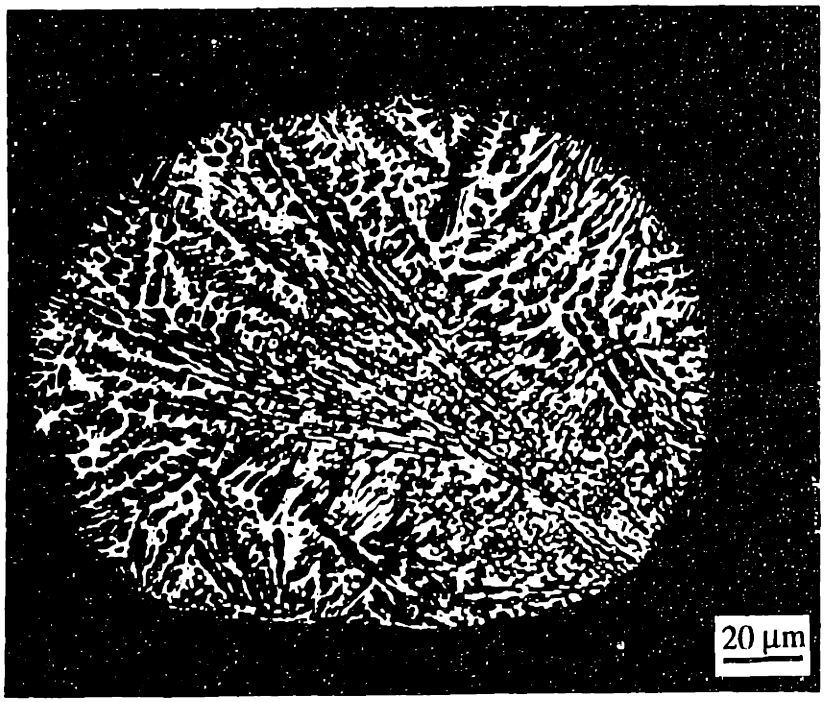

Figure 3.15 Cross-section micrograph for the droplet collected at 0.35 m.

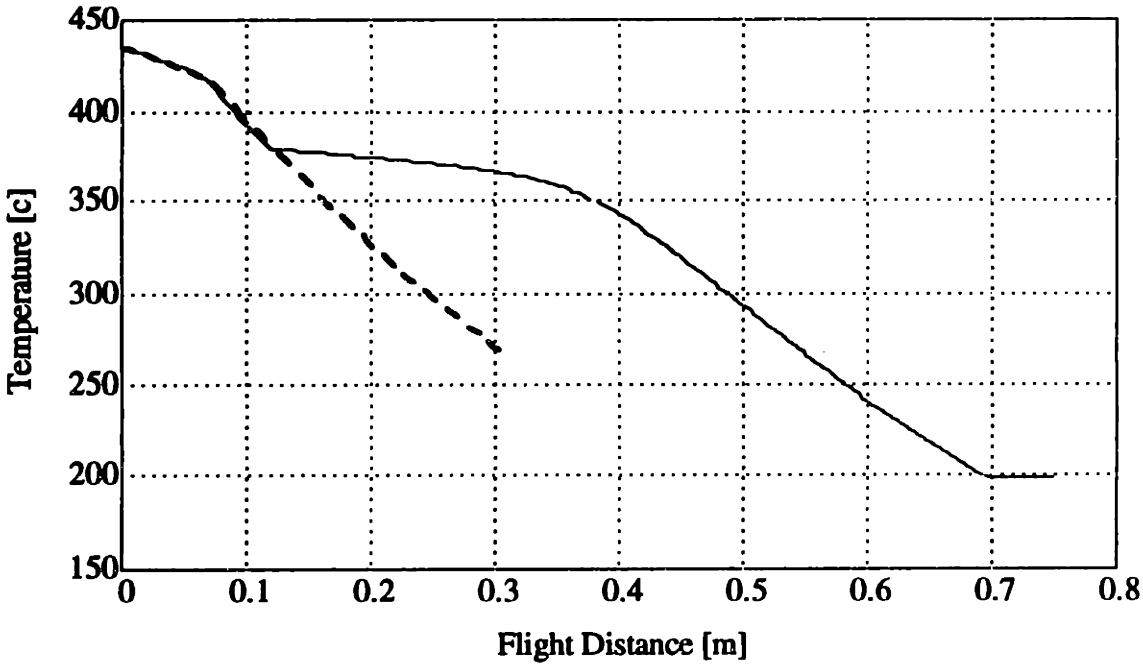

(a)

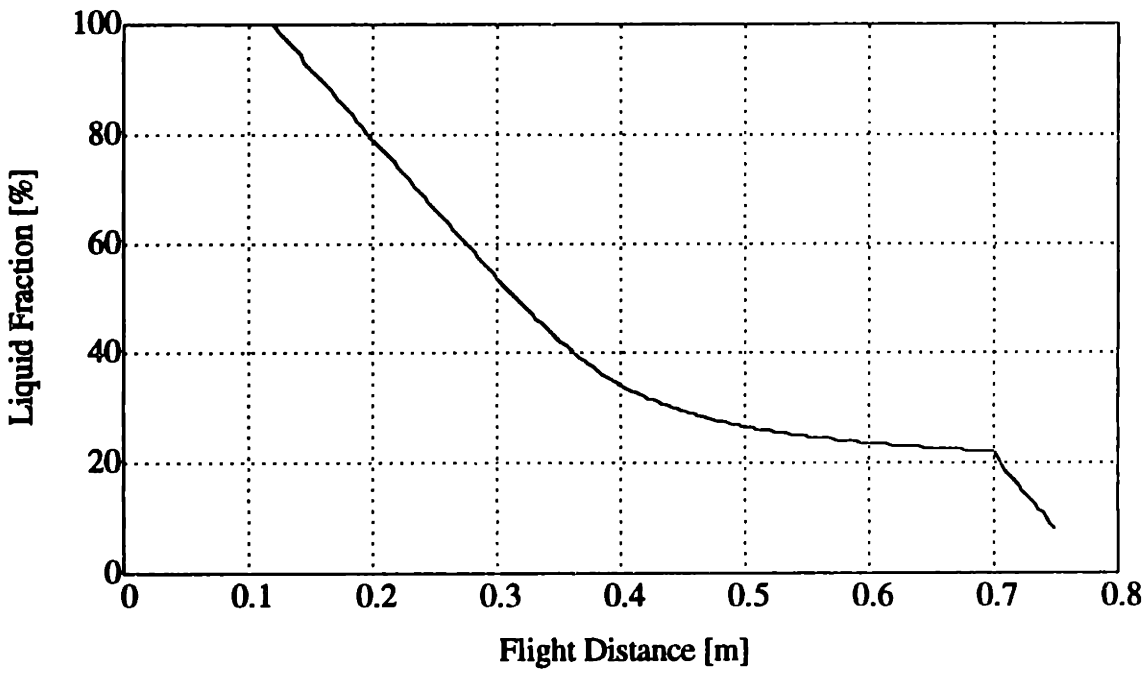

(b)

Figure 3.16 Simulation results for 288 μm droplet solidification: (a) temperature vs. flight distance plot; (b) liquid fraction vs. flight distance plot.

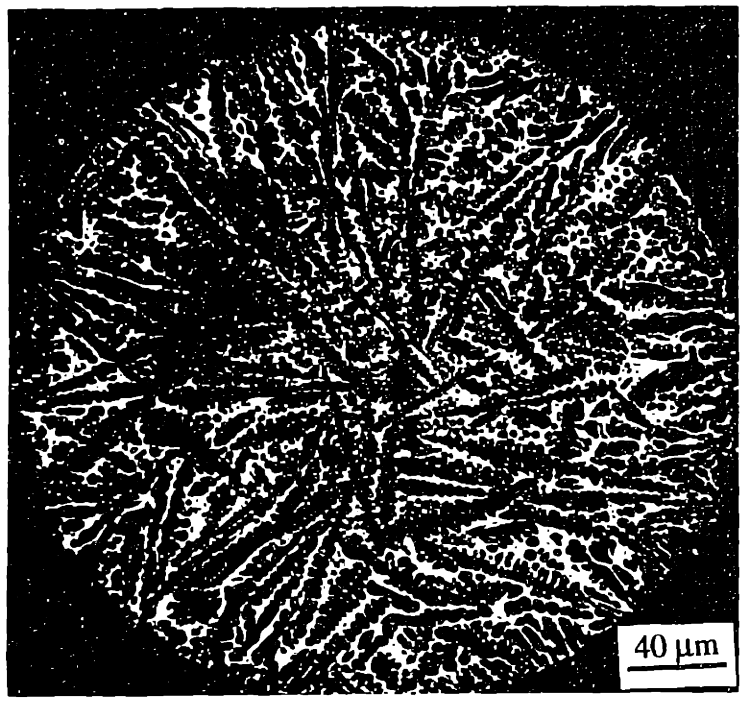

Figure 3.17 Typical cross-sectioned microstructure for 288 µm droplets. A surface nucleated dendritic structure is observed.

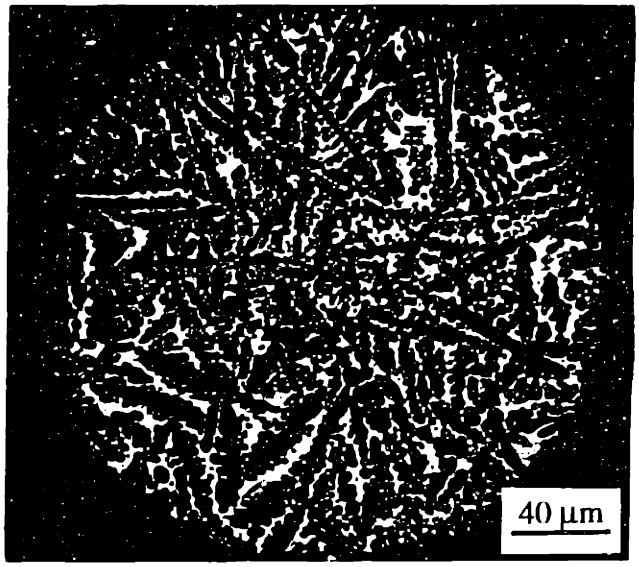

(a)

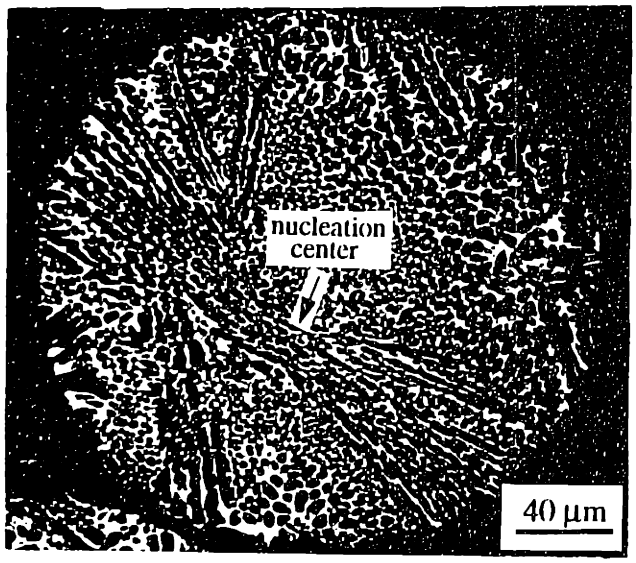

(b)

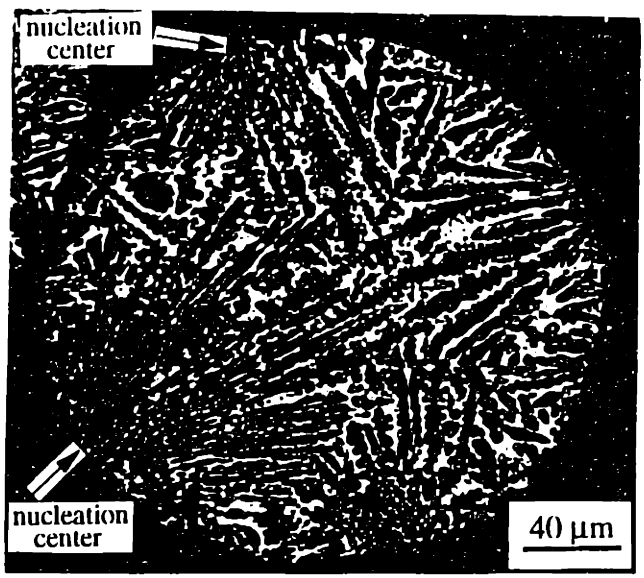

(c)

Figure 3.18 Typical cross-sectioned microstructures for 245 μm droplets. (a) first type: surface nucleated dendritic structure; (b) second type: internally nucleated cellular structure; and (c) third type: surface nucleated cellular structure.

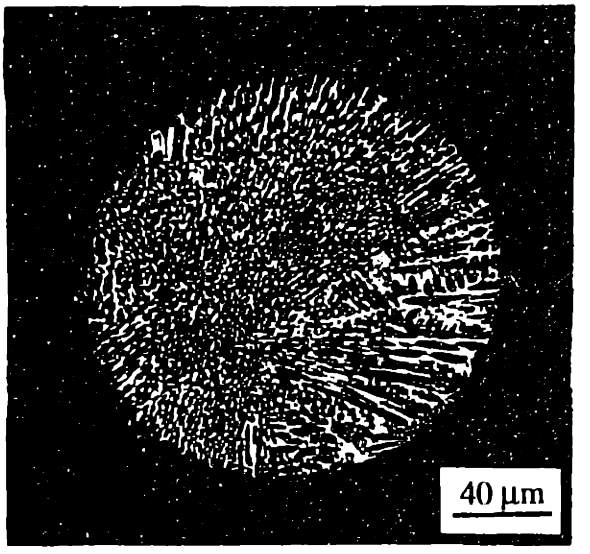

Figure 3.19 Typical cross-sectioned microstructure for 181 μm droplets. An internally nucleated cellular structure is observed.

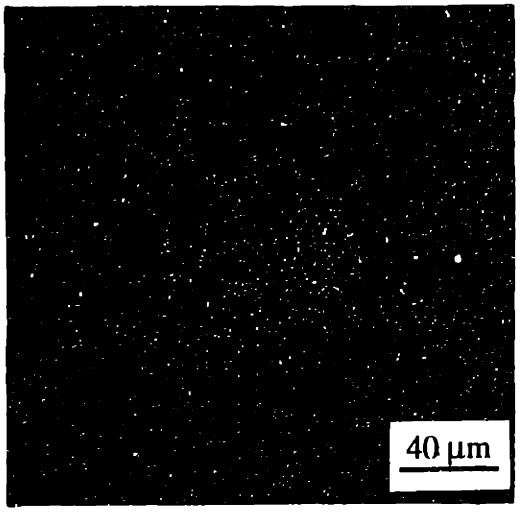

Figure 3.20 Typical cross-sectioned microstructure for 96 μm droplets. The percentage of the cellular structure is higher than that of the 181 μm droplets.

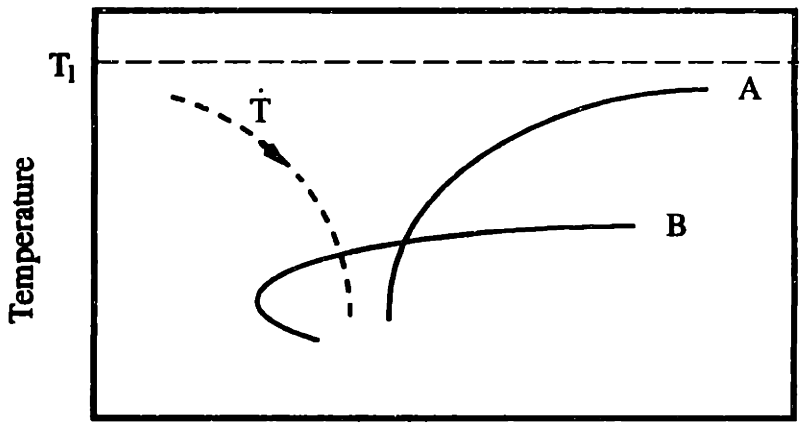

Figure 3.21 Transformation diagram representing two different nucleation kinetics that may occur in undercooled droplets. T_l is the liquidus temperature of the alloy. Curve A represent a more potent catalyst than Curve B.

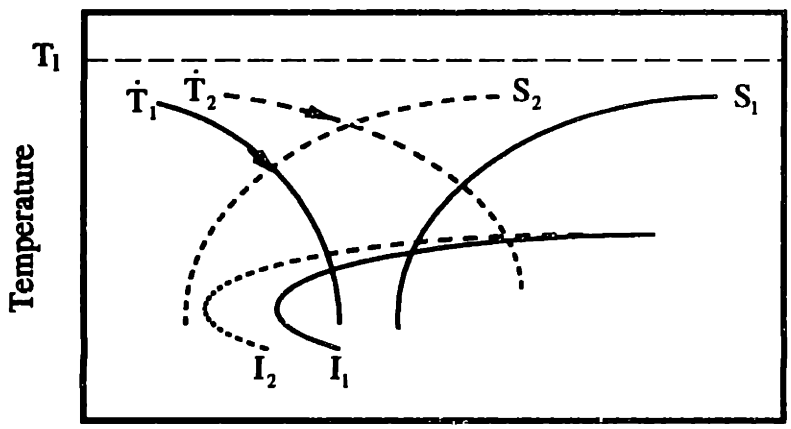

Figure 3.22 Transformation diagram representing internal and surface nucleation kinetics that may occur in 288 and 181 μm droplets. T_l is the liquidus temperature of the alloy. The cooling curve, the transformation curve representing internal nucleation, and the curve representing surface nucleation for 181 μm droplets and for 288 μm droplets are indicated by $\dot{T}_1$, I_1, S_1, $\dot{T}_2$, I_2, and S_2, respectively.

Chapter 4

Effects of Droplet Thermal State and Substrate Condition on Deposit Microstructure

4.1 Introduction

A wide range of spray forming conditions can be obtained in the UDS process for microstructural control by manipulating droplet thermal states and substrate thermal conditions. For example, superheated, undercooled, or partially solidified droplets can be sprayed onto fully liquid, semi-solid, or completely solidified deposit surfaces to produce deposits with different microstructures. To achieve precise microstructural control, an understanding of the relationships between the deposit microstructures and the spray conditions in the UDS process must be understood. These relationships, however, are not yet clear. This work is aimed to provide a general idea about how final deposit microstructures can be influenced by droplet thermal states and substrate thermal conditions so that the basis for further study can be established.

4.2 Experiment

Experiments using a Sn-5 wt% Pb alloy were carried out to study the effects of the droplet thermal state and the substrate condition on the deposit microstructure by controlling droplet liquid fraction and substrate temperature. The experimental conditions were obtained using the droplet thermal model described in Chapter 2 to have the desired droplet liquid fraction. Physical constants used in the simulation are described in Appendix C and a Sn-Pb phase diagram is shown in Figure 4.1 for reference. The deposit surface was maintained in a fairly constant temperature during the experiment by applying a low deposition rate and periodic deposition. Periodic instead of continuous deposition allowed the cooling time necessary for the deposit surface to solidify completely between spraying cycles.

Seven experiments were performed with droplets of 100% liquid with 85 K superheat, 100% liquid without superheat, 70% liquid, and 40% liquid sprayed onto a substrate maintained at 426 and 446 K, respectively. (The liquidus temperature and eutectic temperature of this alloy are 226 and 183 K, respectively) Experimental parameters such as the melt temperature, the droplet flight distance, the substrate moving speed and frequency, and the substrate temperature are listed in Table 4.1.

4.2.1 Experimental Apparatus

The experimental apparatus shown in Figure 4.2 is composed of a droplet generation unit, a gas chamber unit, a motion system, and a temperature-controlled copper substrate (300 mm x 150 mm x 20 mm). The droplet generation unit is the same one as used in the droplet solidification study of Chapter 3 and will not be described here.

The gas chamber unit includes a stainless-steel chamber (2.0 m x 1.0 m x 0.6 m), a vacuum pump, and a N_2 - 2%H_2 gas supply tank. By evacuating and backfilling the chamber several times, the oxygen concentration in the chamber can be reduced to that of the gas tank. The N_2 - 2%H_2 gas mixture further prevents oxidation of the alloy.

The motion system contained in the stainless-steel chamber consists of an X-Y linear table driven by two DC servo motors and a computer responsible for motion control. A tachometer and an encoder are incorporated into each axis for velocity and position feedback signals. With the feedback signals, the motions of the linear table can be programmed to have desired trajectories. The copper substrate is attached to the linear table and is thermally insulated on the sides and at the bottom to protect the linear table and to prevent heat loss. Four cartridge heaters equally spaced are imbed in the copper substrate. Three thermocouples are placed on the substrate surface for temperature monitoring and control. The input power to the heaters is controlled by a temperature controller to maintain a constant substrate temperature.

4.2.2 Experimental Procedures and Conditions

About 400 g of a high purity binary alloy was melted in the crucible in each experiment. A ruby orifice with a diameter of 100 μm was used. The driving pressure was set at 138 kPa to maintain a constant initial jet velocity of 5.2 m/s. With the perturbation frequency set at 10 kHz, uniform droplets of 198 μm in diameter were generated. Spray cone diameter was controlled at 17 mm for both experimental conditions by adjusting the field strength of the charging plate to compensate for the difference in flight distances. This corresponds to a deposition rate of 179 μm/s. The substrate temperature was kept constant at 446 K. The motion of the x-y table was programmed to permit repeated deposition along a rectangular path on the copper substrate with a cycle time of 4.2 seconds. The traveling speed along one of the long edges was set constant at 38 mm/s. This substrate velocity, together with the 17 mm spray cone diameter, resulted in an increase of 83 μm in deposit thickness per cycle. A total of 136 deposition cycles was executed for each experiment.

4.2.3 Sample Preparation

A transverse cross-sectional slice, perpendicular to the bottom surface, was cut from each deposit for sample preparation. The deposit produced in Experiment 1 is shown in Figure 4.3 for reference. These samples were then mounted in clear-cast epoxy, ground, and polished to 0.1 μm. A solution of 2 vol.% HCl - 5 vol.% HNO_3 in methanol was used to exposed the microstructures for examination under a scanning electron microscope.

4.3 Results

Figure 4.4 summarizes the results of the experiments. Experiments 1 to 4 all produced dense, columnar microstructures. Experiment 5 yielded a dense, fine equiaxed grain microstructure. Experiments 6 and 7 resulted in very porous structures. The results for Experiments 1 to 4 were alike, therefore, they are described in detail together. The results for Experiments 6 and 7 are also illustrated together since they present similar features.

4.3.1 Columnar Microstructure

SEM micrographs from Experiment 1 are shown in Figure 4.5 to represent the microstructures produced in Experiments 1 to 4. Columnar growth prevails in the deposit except in a transition zone near the bottom, in which the microstructure changes from a fine, equiaxed microstructure to a columnar structure. The thickness of the transition zone is about 500 to 600 μm. The Sn-rich columnar grains grew incrementally as the molten droplets were added. The growth of the columnar crystals continued for many hundreds of splats and is therefore epitaxial. Figure 4.6 shows the microstructure at a mid portion of this deposit at a higher magnification. A closer look at Figure 4.6 reveals that the columnar grain boundaries are partially delineated with thin films of Pb without secondary arms, indicating that the interface morphology is cellular. Fine spherical precipitates of Pb were also observed within the columnar grains of Sn. The cellular structures and high density of intra-grain precipitates are indicative of rapid solidification. Splat or spray boundaries are virtually invisible.

4.3.2 Fine, Equiaxed Microstructure

Figure 4.7 shows the equiaxed microstructure from the mid portion of the Sn-5 wt% Pb deposit produced in Experiment 5 using 70% liquid droplets. The entire deposit presents the same microstructure shown in the figures. The microstructure is characterized by uniformly-sized Sn-rich grains with Pb-rich phase present along the grain boundaries. The average grain size is about 40 μm. The amount of the Pb-rich phase precipitating along the grain boundaries is not sufficient to account for the 5% Pb content in the alloy. A closer look at the microstructure, as in Figure 4.8, reveals the fine Pb-rich intragranular precipitates in the interior of the Sn-rich grains. No splat or spray boundaries are discernible and no noticeable porosity can be found.

4.3.3 Porous Structure

Figure 4.9 shows the porous structure produced in Experiment 6 using droplets with 70% liquid and a substrate at 426 K. As shown in the figure, the bottom region,

composed of the first two or three droplet layers, is less porous than the upper region, although it still presents a significant level of porosity. Figure 4.10 shows the microstructure of one of the prior droplets in the deposit. The microstructure consists of fine Sn-rich equiaxed grain with a Pb-rich phase precipitating on the tin boundaries. The Sn-rich grains averaged about 10 μm are much finer than those produced in Experiment 5. Similar porous structure is observed for the deposit produced in Experiment 7 using droplet with 40 % liquid and a substrate at 446 K.

4.4 Discussion

4.4.1 Formation of Columnar Microstructure

Epitaxial columnar microstructures occurred in Experiments 1 to 4 since the droplets were all in liquid state upon impact, providing no growth centers, and nucleation in the molten splat was more difficult than continuous growth of the columnar crystals into the newly added liquid layer. The epitaxial columnar growth in the spray deposit produced in Experiments 1 to 4 is significant in that these columnar crystals are not only directionally solidified but also rapidly solidified. Such rapid-solidification epitaxial growth can only result when all of the incoming droplets are molten, which is not the case with non-uniform droplet spray processes. Singer and Evans [1] first reported on the epitaxial crystal growth in a spray deposit of Nimonic 80A produced with a gas-atomized process at a low deposition rate. The observed epitaxial growth, however, was confined in small volumes consisting of a few splats. This is most likely caused by the formation of thin films of oxide on the splat surface which act as barriers to epitaxial crystal growth [36]. The use of a N_2 - 2% H_2 gas mixture as the atmosphere in the present study prevented such oxide formation.

4.4.2 Formation of Equiaxed Microstructure

The formation of an equiaxed microstructure requires that crystals of random orientation be produced at some stage of processing. Several possible mechanisms, listed

below, have been proposed for the formation of randomly oriented crystals in spray forming [45-48]:

(1) Randomly oriented crystals are formed readily in mushy droplets or are generated upon impact due to fragmentation of the solids in the droplets.

(2) Crystals growing in the mushy deposit surface are fragmented by the impact of incoming droplets to provide randomly oriented growth centers.

(3) Small presolidified particles act as randomly oriented growth centers upon arrival on the deposit surface.

(4) Crystals in the deposit surface are deformed by the incoming droplets and recrystallize subsequently to form an equiaxed microstructure.

To study the role of the deposit surface on the formation of equiaxed microstructure, a deposit thermal model developed by Acquaviva [11] was employed to investigate the surface condition of the deposit for Experiment 5. The discrete nature of deposition was simplified in this model by assuming an equivalent averaged continuous deposition. The simulation result is shown in Figure 4.11. As shown in the figure, the deposit surface was below the eutectic temperature at all times during the experiment. This indicates that the deposit surface was maintained in a constantly solid state. Therefore, mechanism (2) should not have played a role in the formation of the equiaxed microstructure since the crystals at the deposit surface were all solidified before the arrival of the next droplets and accordingly could not have been fragmented. Mechanism (3) also could not have participated in the formation of the equiaxed microstructure due to the absence of presolidified particles in the UDS process. Moreover, because of the low droplet velocity of about 5 m/s used, mechanism (4) may not have contributed. The results suggest that an equiaxed microstructure can be produced by mechanism (1) alone. The equiaxed microstructure was possibly formed due to the continued growth and eventual coarsening of the randomly oriented solids in the newly added splats. The absence of splat or spray boundaries in the spray deposit, as shown in Figure 4.6, strongly suggests that some of the

grains in the prior splat grow epitaxially into the new splat until they contact other crystals, thus eliminating splat boundaries in the incrementally solidified deposit.

The observed average grain size, 40 μm, is more than two times smaller than the droplet radius, 90 μm, which is as long as a dendrite arm can grow if droplets solidify completely in flight. Since the droplets contained 70% liquid upon impact, the dendrite arm should grow only to 10 μm if surface nucleation is assumed. The size of the randomly oriented crystals for equiaxed grain growth can only be smaller because dendrite arms might break upon impact. This effect, however, is believed to be small. The final grain size, 40 μm, is therefore the result of dendrite arm re-orientation upon impact, and post-impact growth and coarsening. Based on these arguments, it can be stated the grain size of the equiaxed grain is a function of not only the droplet liquid fraction and local solidification time but also the droplet size since the dendrite arm length is largely determined by the droplet size. Further study is necessary to investigate the dendrite arm breaking effect and the significance of the post-impact growth and coarsening.

4.4.3 Formation of Porous Structure

Experiment 6 resulted in a porous structure because the relatively cool substrate caused the 70% liquid droplets to solidify at a faster rate, thus reducing the degree of droplet spreading to the extent that pores could not be closed. Experiment 7 resulted in a porous structure since the droplets used in this experiment contained only 40% liquid at the time of impact, the degree of spreading and the amount of liquid were not enough to fill the gaps between splats. In both experiments, the bottom regions are denser than the upper regions because the degree of droplet spreading was higher for the first two or three layers due to the flat substrate surface. Spreading became more difficult as the layers built up to form a rougher deposit surface.

The fine, equiaxed microstructures observed in the prior-droplet splats for both Experiments 6 and 7 are the consequence of dendrite arm re-orientation upon impact, and post-impact growth and coarsening. The grain size (10 μm) is much smaller than

that of Experiment 5 (40 μm) because the liquid state coarsening effect is highly reduced due to either the cooler substrate in Experiment 6 or the low liquid content droplets in Experiment 7.

4.4.4 Process-Microstructure Map

The conditions used in the present study represent only few of many conditions applicable to spray forming by the UDS process. A process-microstructure map which includes all possible spray forming conditions is schematically presented in Figure 4.12 to show the microstructures that are expected in the UDS process. In this map, the droplet thermal state and the deposit thermal state are chosen as the independent variables. It should be emphasized that the process map is intended for a qualitative representation of the possible process window and the expected microstructures but not for characterization of the relationships between process parameters and microstructures. A quantitative process-structure map may be difficult, if not impossible, to genenerate because the associated process parameters vary with types of microstructures; as a result, there may not be general variables to characterize the process-structure relationships. For example, the generation of epitaxial columnar structures depends only on droplet liquid fraction and local solidification time while the production of equiaxed microstructures depends not only on droplet liquid fraction and local solidification time but also on droplet size as mentioned earlier.

In general, the combination of hot droplets and a long solidification time produces coarse solidification structures (upper right corner), whereas cold droplets and rapid solidification produce porous structures (lower left corner). An optimum range for the production of dense, fine, equiaxed microstructures is thus found between these two extremes. The conditions in the lower right half are not attainable because the liquid fraction of the deposit surface cannot exceed the droplet liquid fraction unless a secondary heat source is used to heat the deposit surface. The conditions near the upper left corner are important since they lead to rapidly solidified novel microstructures as demonstrated in this

study. Amorphous deposits can perhaps be produced with undercooled droplets at a sufficiently low, controlled deposition rate. It should be emphasized that the process-structure map only serves to show the possible microstructures that can be produced with the UDS process.

4.5 Conclusions

(1) Spray forming of molten Sn-5 wt% Pb droplets at a low deposition rate produced rapidly solidified columnar microstructures. No splat boundaries were produced. The primary Sn-rich phase columnar grains were contiguous through the entire deposit thickness of about 20 mm. The epitaxial columnar microstructures came about because nucleation in the molten splat was more difficult than the continuous growth of the columnar crystals into the newly added liquid layer.

(2) Spray forming of 70% liquid Sn-5 wt% Pb droplets onto a 446 K substrate produced a fine, equiaxed microstructure. The equiaxed grains are those of the Sn-rich phase and were delineated with thin films of the Pb-rich phase along the grain boundaries. No splat or spray boundaries were noted.

(3) The equiaxed microstructure evolved mainly from randomly oriented crystals, which were originally present as dendrites in the droplets and were re-oriented upon impact. The lack of splat boundaries was explained by the local epitaxial growth of the grains in the prior splat and the oxide-free deposit surface maintained during the experiment. The use of mushy droplets is the single most important requirement for the formation of equiaxed microstructures in a spray deposit. The thermal state of the deposit surface may play only a minor role.

(4) The equiaxed grain size is a function of droplet liquid fraction, droplet size, and local solidification time. The droplet liquid fraction and the droplet size determine the size of dendrite arms, thus, the size of the randomly oriented crystals for equiaxed grain growth;

while the local solidification time controls the post-impact growth and coarsening of the randomly oriented crystals.

(5) Porous structures were produced when 70% liquid droplets were deposited onto a 426 K substrate and when 40% liquid droplets were deposited onto a 446 K substrate. Porous structures resulted because the degree of droplet spreading was reduced either by low liquid content in the droplets or by a high freezing rate from a relatively cold substrate.

(6) A schematic process-microstructure map for the spray forming process is used to qualitatively show the entire process window and expected microstructures for spray forming with uniform-droplet sprays. A quantitative process-structure map may be difficult, if not impossible, to generate because general variables to characterize the process-structure relationships may not exist.

Table 4. 1 Experimental conditions for deposit microstructure experiment.

Exp. No.	Melt Temp (K)	Flight Distance (m)	Charging Field Strength (V/mm)	Estimated Droplet Liquid Fraction	Substrate Moving Period (sec/cycle)	Substrate Temp (K)
1	673	0.27	66.7	100 % (+85 K)	4.2	446
2	673	0.27	66.7	100 % (+85 K)	4.2	426
3	573	0.27	66.7	100 % (+0 K)	4.2	446
4	573	0.27	66.7	100 % (+0 K)	4.2	426
5	673	0.48	94.4	70 %	4.2	446
6	673	0.48	94.4	70 %	4.2	426
7	573	0.48	94.4	40 %	4.2	446

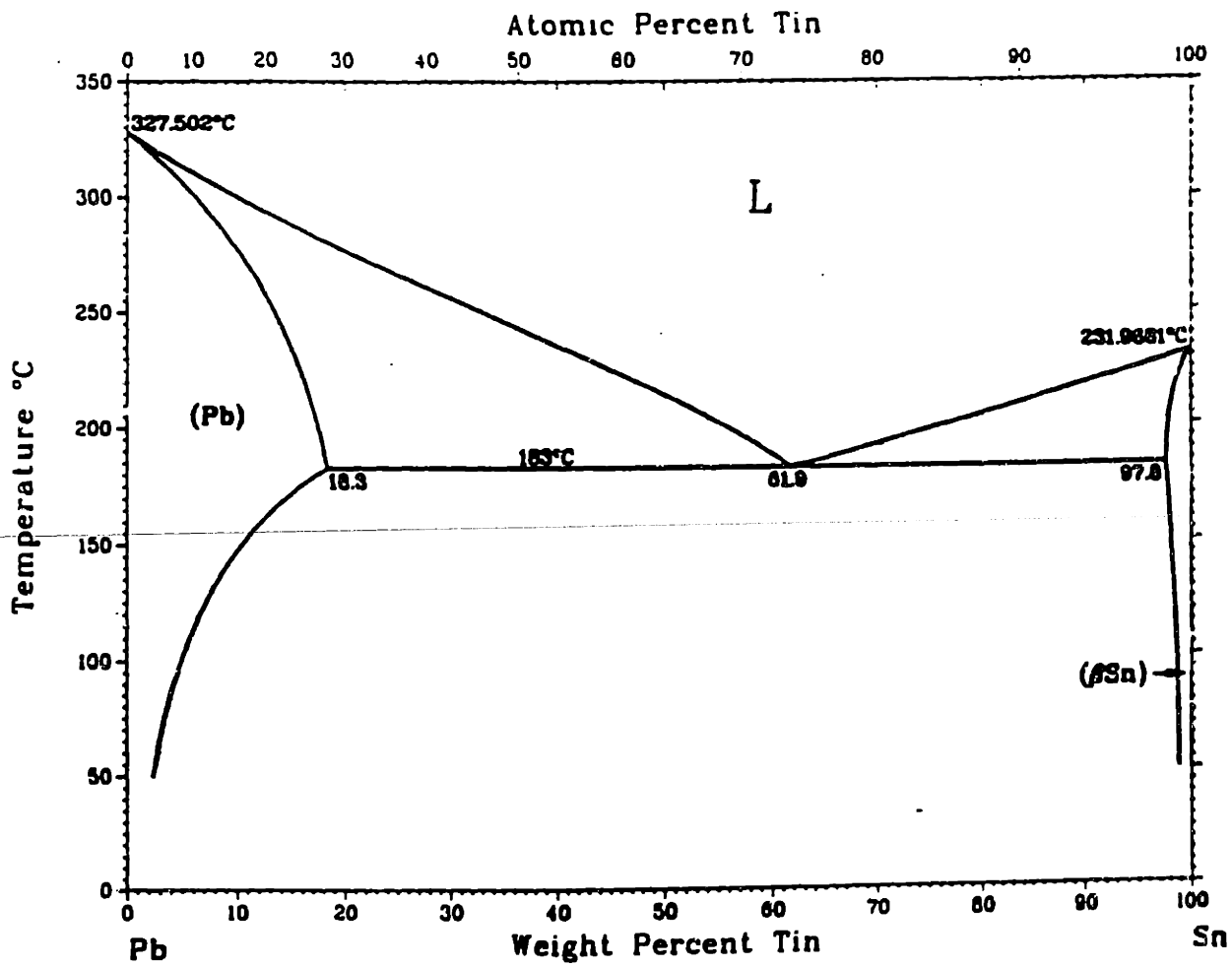

Figure 4.1 Sn-Pb phase diagram.

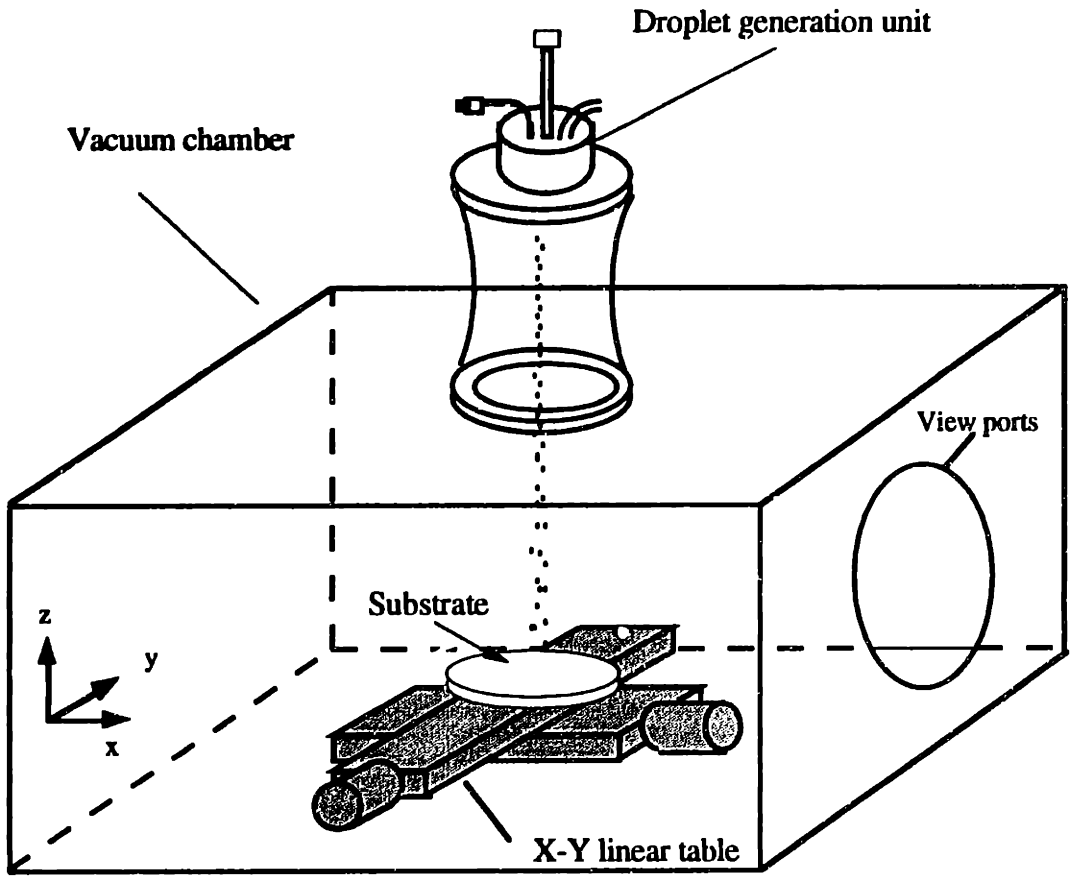

Figure 4. 2 Schematic illustration of the apparatus for deposit microstructure experiment. The apparatus consists of a droplet generation unit, a vacuum chamber, a X-Y linear table, and a copper substrate.

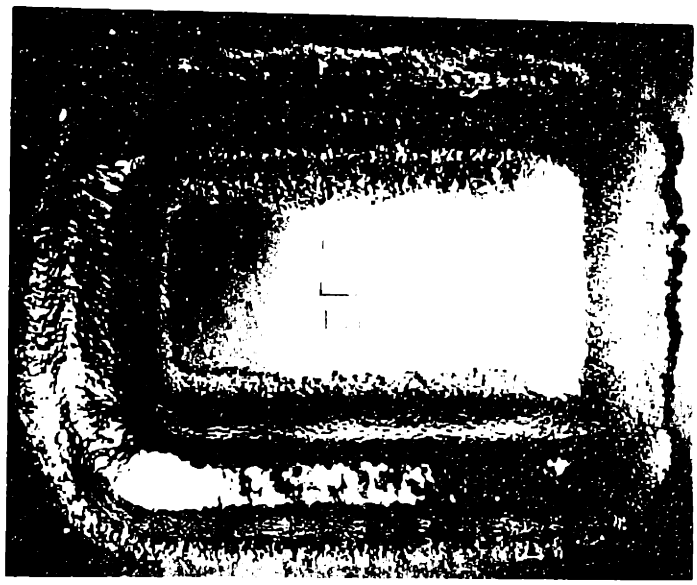

Figure 4.3 Picture of the deposit produced in Experiment 1.

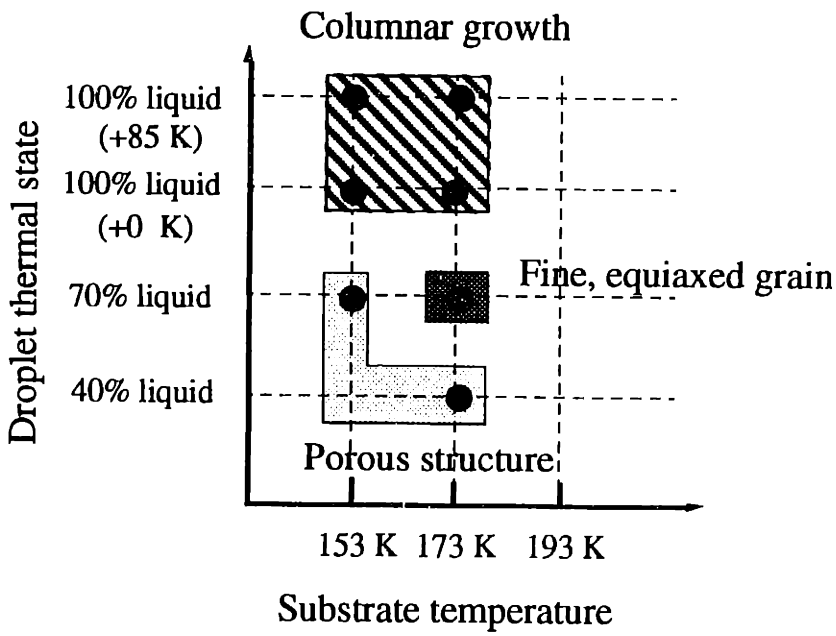

Figure 4.4 Summary of the spray deposition experiment results. Columnar, equiaxed, and porous microstructures are produced in the deposit microstructure experiment.

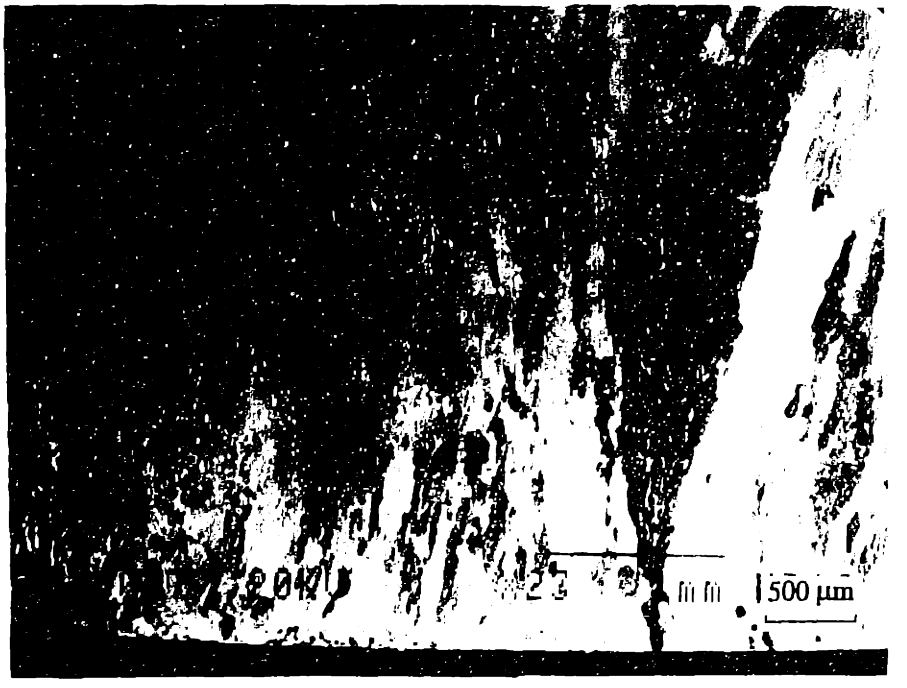

Figure 4.5 SEM cross-section micrograph of the spray deposit for Experiment 1. A fine, equiaxed microstructure is found near the bottom. A epitaxial growth columnar microstructure characterizes the rest of the region.

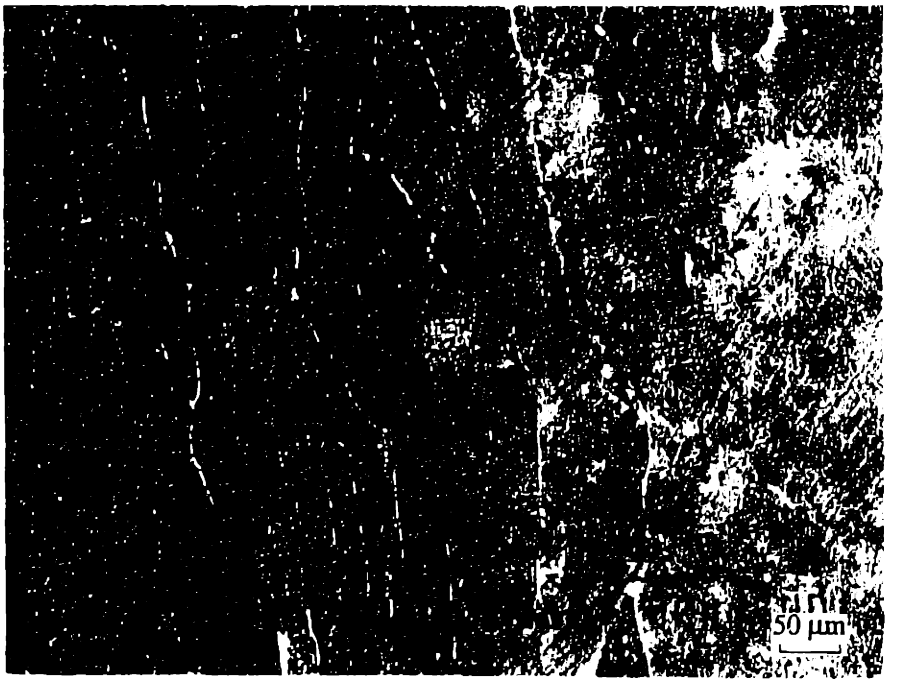

Figure 4.6 SEM cross-section micrograph of the spray deposit for Experiment 1 taken at the middle portion at a higher magnification. Fine intragranular Pb-rich precipitates as well as Pb-rich precipitates along the boundaries are present.

Figure 4.7 SEM cross-section microgrph of the spray deposit from Experiment 5. This deposit shows a fine, equiaxed microstructure and virtually no porosity.

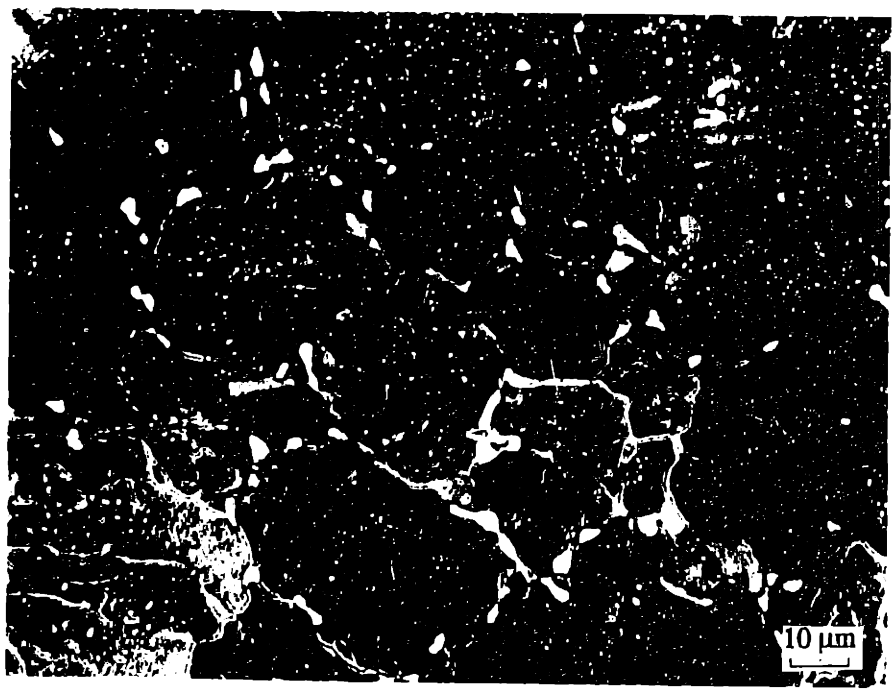

Figure 4.8 SEM cross-section micrograph of the spray deposit from Experiment 5 at higher magnification. Fine intragranular Pb-rich precipitates and coarse Pb-rich precipitates along the grain boundaries are noted.

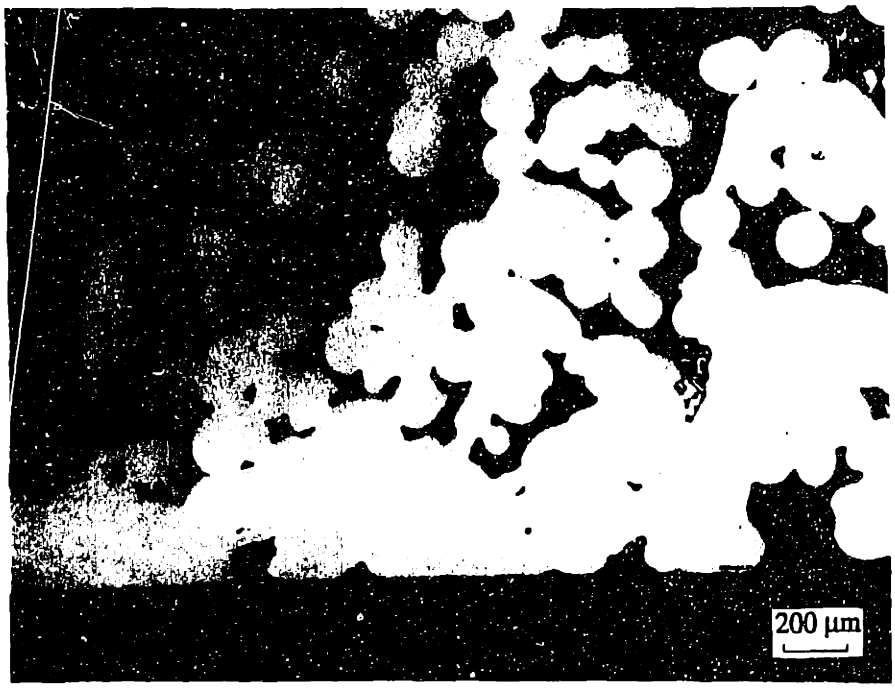

Figure 4.9 SEM cross-section micrograph of the spray deposit from Experiment 6. This deposit is very porous except at the bottom region.

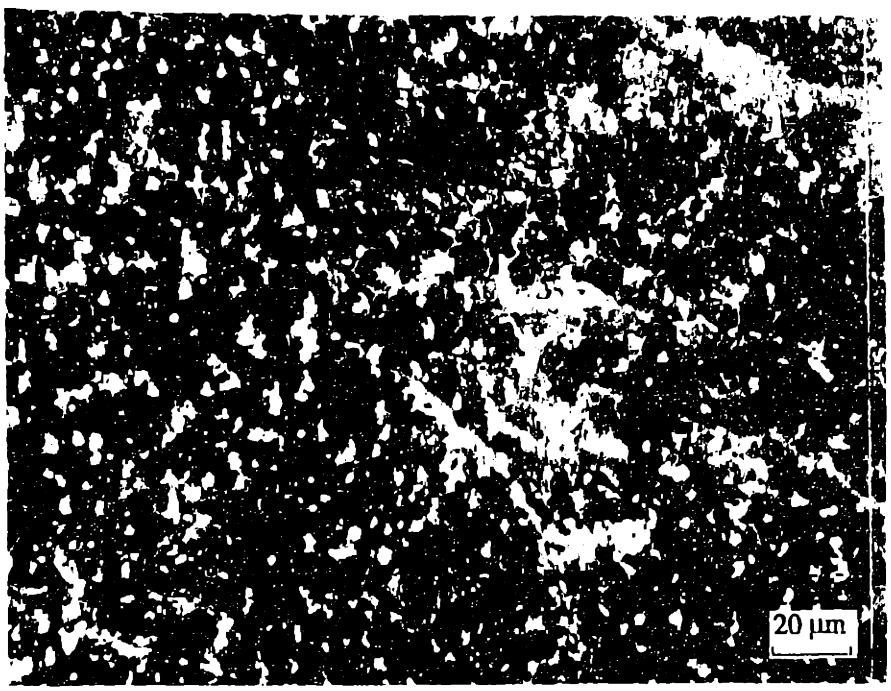

Figure 4.10 SEM cross-section micrograph of one of the prior droplet in the spray deposit from Experiment 6. Finer equiaxed grains with Pb-rich precipitates on the boundary are noted.

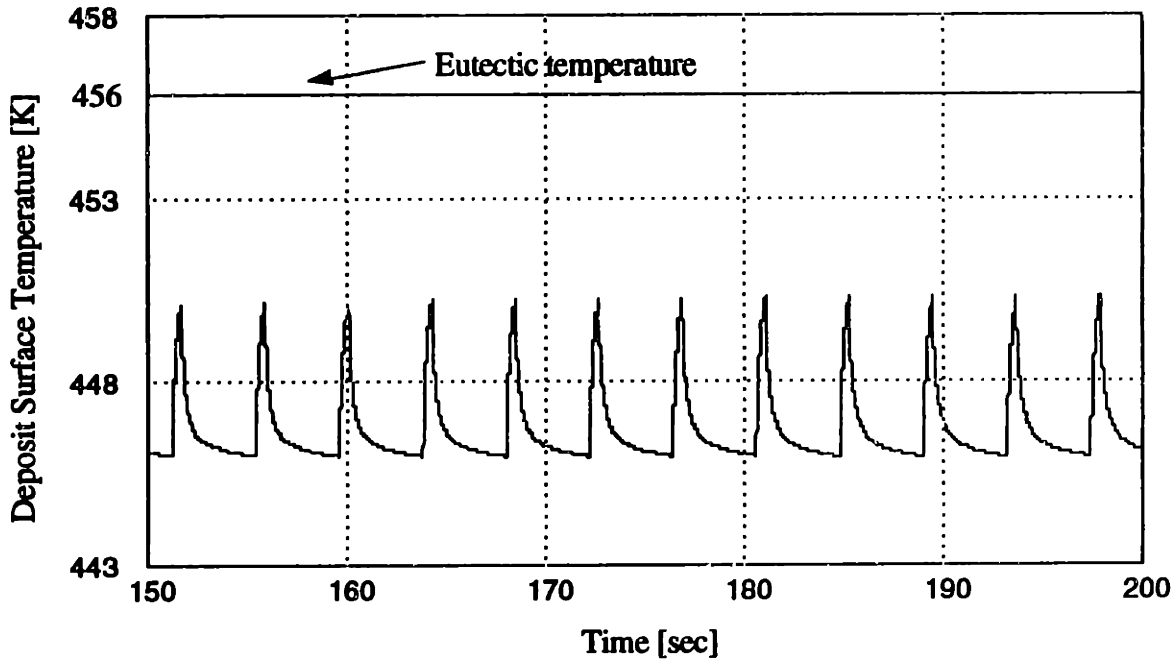

Fig. 4.11 Simulated deposit surface temperature vs. time for Experiment 1. The eutectic temperature is indicated to show that the deposit surface was constantly maintained in a solid state.

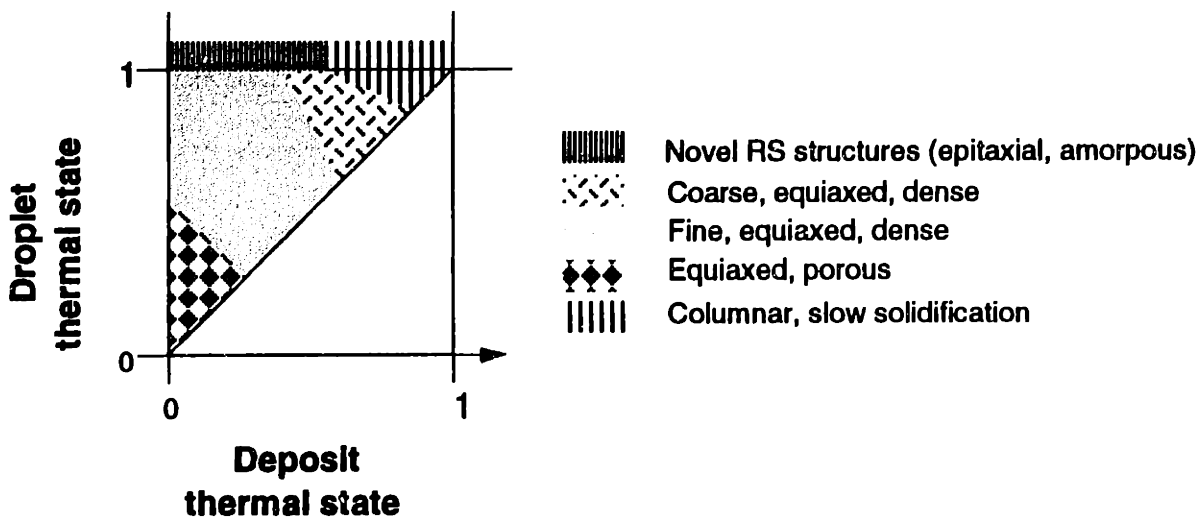

Fig. 4. 12 Schematic process-microstructure map for uniform-droplet spray forming

Chapter 5
Summary and Conclusions

5.1 Summary

5.1.1 Droplet Thermal Model

• Droplet solidification is modeled by considering droplet flight trajectory and droplet heat transfer simultaneously. The Scheil equation is employed to model solute redistribution in the droplet during solidification. The effects on droplet solidification of several process parameters such as initial jet velocity, droplet charge, and droplet size are studied through simulation.

• Droplets with a higher initial velocity have a higher cooling rate. However, since the time required for them to reach a certain flight distance is shorter, they lose less heat than the droplets with a lower velocity at the same flight distance. Therefore, droplets with a higher velocity have a higher temperature and liquid fraction when collected at the same flight distance.

• The droplet charge affects droplet cooling mainly by changing the spreading distance, i.e. the distance at which the heat transfer coefficient increases dramatically. The delay in spreading distance for less charged droplets is reflected by the delay for the droplet temperature to reach the eutectic point. The heat transfer coefficient change resulting from the small velocity change is insignificant in influencing droplet cooling.

• Droplet size is the most critical process parameter in controlling the droplet cooling rate. A wider range of cooling rates is achieved by varying the droplet size than by altering the initial velocity or droplet charge. Smaller droplets cool faster and solidify in short distances; thus they are more sensitive to variations in flight distance than larger droplets.

5.1.2 Droplet Solidification Experiment

• Experiments investigated the effects on droplet solidification of flight distance, droplet size, and oxygen concentration using a Zn-20 wt% Sn alloy.

• For the flight distance effect study, 288 μm droplets were collected every 0.05 m from 0.35 to 0.75 m and 181 μm droplets were collected every 0.05 m from 0.15 to 0.55 m. The results showed that the 288 μm droplets solidified gradually without undercooling and the 181 μm droplets experienced undercooling of about a 110 K. For the 288 μm droplet samples, the liquid fractions derived from image analysis show good agreement with those derived from simulation.

• For the droplet size effect study, 288, 245, 181, and 96 μm droplets were collected. The results show that the 288 μm droplets experienced virtually no undercooling, the microstructure is dendritic, and the nucleation took place on the droplet surface. Three types of microstructures were observed for the 245 μm droplets. The first type is similar to the 288 μm droplet microstructure. The second type is characterized by a celluar structure nucleated within the droplet and dendritic structures solidified after recalescence. The third type is defined by a cellular structure nucleated on the the droplet surface and dendritic structures solidified after recalescence. The 181 and 96 μm droplets were all undercooled and internally nucleated. The percentage of the cellular structure increases and the sizes of the cells and dendrites decrease when droplet size decreases.

• Kinetic competition between different catalysts for nucleation explains why the population of undercooled droplets, the degree of undercooling, and the tendency to nucleate internally an increase as the droplet size decreases.

• For the oxygen effect experiment, 181 μm droplets were collected with the chamber oxygen concentration maintained at 5, 50, 100 ppm. No significant difference in the cross-section microstructure can be noticed. The droplets are undercooled and internally nucleated.

5.1.3 Deposit Microstructure

• Seven experiments were performed to study the effects of the droplet thermal state and the substrate condition on the droplet microstructure by spraying droplets of 100% liquid with 85 K superheat, 100% liquid with no superheat, 70% liquid, and 40% liquid onto a substrate maintained at 426 and 446 K, respectively.

• The results show that droplets with 100% liquid all produced epitaxial columnar microstructures. With 70% liquid droplets and a 446 K substrate, a fine, equiaxed, dense microstructure was produced. Porous structures resulted when 70% liquid droplets were deposited onto a 426 K substrate or when 40% liquid droplets were deposited onto a 446 K substrate.

• The epitaxial columnar microstructure resulted because nucleation in the molten splat was more difficult than the continuous growth of the columnar crystals into the newly added liquid layer. The equiaxed microstructure evolved mainly from randomly oriented crystals, which were originally present as dendrites in the droplets and were re-oriented upon impact. Porous structures resulted because the degree of droplet spreading was reduced either by low liquid content in the droplets or by a high freezing rate from a relatively cold substrate.

5.2 Conclusions

(1) The value of the droplet thermal model lies in its effectiveness in determining the effects on droplet solidification of droplet initial velocity, droplet charge, and droplet size, which would otherwise takes much more time and effort to demonstrate by experiment. Although the droplet thermal model becomes ineffective when undercooling occurs, it allows for study of the influence of various process parameters on droplet cooling rate, and therefore on droplet undercooling behavior.

(2) The undercooling behavior of droplets is a function of droplet size, purity of materials, and gas environment in the chamber. The degree of droplet undercooling is difficult, if not

impossible, to predict with existing theories. The droplet interacting technique combined with the droplet thermal model is capable of successfully determining the degree of undercooling.

(3) To produce fine, equiaxed grain microstructures, the droplets should be as small as possible since the final grain size is a function of the dendrite arm size (or the droplet size) as explained in Chapter 4. The droplet size, however, cannot be too small for undercooling to occur. Therefore, an optimum droplet size should exist for the production of fine, equiaxed grain microstructures for any alloys.

Chapter 6
Suggestions for Future Study

Several research areas can be further explored based on this work,. They include developing a grain size predictive model for deposits with equiaxed microstructures; establishing the relationship among the droplet thermal state, the substrate condition, and porosity formation; and producing rapid solidified materials using highly undercooled droplets. This chapter describes suggestions for these studie.

6.1 Grain Size Predictive Model

Chapter 4 concludes that an equiaxed microstructure evolves in the UDS process mainly from randomly oriented crystals which are either formed readily in mushy droplets or generated upon impact due to fragmentation of the solids in the droplets. If the number and size distribution of these randomly oriented crystals can be determined, it is possible to predict the final grain size using existing grain growth and coarsening theories based on the spray forming condition. To develop a grain size predictive model, the following procedures are suggested:

(1) Determine the number and size distribution of the randomly oriented crystals in a single droplet splat immediately after impact by using the experimental methodology employed in the flight distance effect study.

(2) Determine the constants which are needed in applying grain and coarsening theory by annealing the splat samples under different thermal conditions.

(3) Develop a grain growth and coarsening model by considering the concurrent growth and coarsening in the mushy regime and pure coarsening in the solid regime.

(4) Calculate the thermal history of the deposit with the deposit solidification model.

(5) Predict the final grain size using the grain growth model and the thermal history of the deposit.

6.2 Porosity Formation

Porosity formation should be avoided in the production of high strength materials since porosity is detrimental to the material mechanical properties. Therefore, it is necessary to establish the relationship among the droplet thermal state, the substrate condition, and the porosity. Since the droplet thermal state in the UDS process can be fully characterized using the experimental method developed in this work, construction of a map for porosity formation is possible. The following procedures are suggested for the construction of such a map:

(1) Deposit droplets with various thermal states on substrates with various thermal conditions using different materials to examine porosity formation.

(2) Derive two scaling numbers based on the droplet liquid fraction, droplet size, substrate thermal conditions, and material properties for the map construction.

(3) Construct the general map for porosity formation using the two scaling numbers and the experimental results.

6.3 Rapid Solidified Materials

The experimental results presented in Chapter 3 suggest three things about the UDS process: high undercooling can be achieved in small droplets, the degree of undercooling is uniform for sufficiently small droplets, and undercooling can be quantified using the experimental method developed. These advantages, combined with the capability to control the deposition rate and substrate condition precisely, make the UDS the most reasonable process to produce bulk rapidly solidified amorphous and crystalline materials. The periodic deposition employed in this work is suggested for the production of rapidly solidified materials.

Appendix A

Matlab Droplet Solidification Simulation Program

```
clear
% Feb. 3,1996
% Modified by Chen-An Chen for droplet solidification for Zn-Sn alloy
% Droplet Flight Simulation
%*************************************************************************
% Declare Variables and Initial Values
%*************************************************************************
% Gravitational Acceleration [m/s2]
      g = 9.81;
% Permittivity of Free Space [C2/Mm2]
     ezero = 8.85e-12;
clear
% Gas Properties
% Gas Properties for Nitrogen %% Gas #1
% gas density [kg/m3] (@300K 1990-91 CRC 6-17)
      Dg(1) = 1.12;
% gas viscosity [Ns/m2] (@300K 1990-91 CRC 6-17)
      Vg(1) = 1.8E-5;
% gas conductivity [W/mK] (@300K 1990-91 CRC 6-17)
      Kg(1) = 2.58E-2;
% chosen gas (nitrogen)
      gas = 1;
% Properties for Zn-Sn alloy
% weight percentage of Sn
      Co=0.2;
      Cl=0.2;
%initial melt temperature (deg C)
      T=435;
%density of the alloy [kg/m3]
      density=DZnSn(Co,Cl,T)
%liquidus temperature
                  Tl=419.58-3.237*(Co*100)+7.571e-2*(Co*100)^2-7.285e-
4*(Co*100)^3    %Tin deg C
%initial melt enthalpy [J/kg]
      en=eZnSnlqd(Co,T);

% Control Parameters
% orifice diameter [m]
      orifice = 100E-6
% driving pressure [psi]
     pressure = 20
% driving frequency [Hz]
      frq = 8300
% charger diameter [m]
      charger_diameter = 0.0045;
% charger voltage [volts]
      charger_voltage = 400
% meseasured mass flow rate [kg/sec]
      mflow = 55.5e-3/(60*4);   %=169.9e-3/284 (150μm)
        gas_temperature = 50;
```

```
        substrate_position = 1.0

% Jet Parameters
% volume flow rate
    vflow = mflow/density;
% jet diameter [m]
            dj = orifice;
% jet velocity [m/s] (+downward)
    vj = vflow/(pi*(dj^2)/4)

% Droplet Parameters

% droplet diameter [m]
        d = ((6/4)*dj^2*vj/frq)^(1/3)
% droplet cross sectional area [m2]
        ac = (1/4)*pi*d^2;
% droplet surface area [m2]
        as = pi*d^2;
% droplet volume [m3]
        vlm = (1/6)*pi*d^3;
% droplet mass [kg]
 density
        m = density*vlm;
% charger capacitance [farads] (check this d should be orifice diameter)
        charger_capacitance = 2*pi*ezero*(vj/frq)/log(charger_diameter/dj);
% droplet charge [Coulombs]
        q = charger_capacitance*charger_voltage
% scatter constant
        sc = q*q/((4*pi*ezero)*((1/6)*pi*d^3*density));
% Counting Parameters
% number of droplets for spreading calculations
        nd = 5;
% time per spreading step
        tpss = 0.0001;
% number of spreading steps per flight step
        nsspfs = 10;
% time per flight step
        tpfs = nsspfs*tpss;
% number of steps (approximate)
        ns = abs(round(substrate_position/(vj*tpfs)));
% number of data points (approxiamte)
        ndp = 50;
% number of steps per data point
        nspdp = ceil(ns/ndp);

% Droplet Initial Conditions and Data Variables
% position [m] (measured from orifice (+z downward)
        xc = 0.0001*d*rand(nd,1);
        for j=1:nd
  xc(j) = xc(j)+(0.00001*d*cos(pi*j));
     end
        yc = 0.0001*d*rand(nd,1);
        zcur = 0;
        x = zeros(ndp,1);
```

```
        y = zeros(ndp,1);
        z = zeros(ndp,1);
% velocity [m/s] (+vz downward)
        vxc = zeros(nd,1);
        vyc = zeros(nd,1);
        vzcur = vj;
        vx = zeros(ndp,1);
        vy = zeros(ndp,1);
        vz = zeros(ndp,1);
% accelerations [m/s2] (+az downward)
        axc = zeros(nd,1);
        ayc = zeros(nd,1);
        azcur = 0;
        ax = zeros(ndp,1);
 ay = zeros(ndp,1);
        az = zeros(ndp,1);
% thermal data variables
sT(1)=T;
sflqd(1)=1;
sz(1)=0;
stime(1)=0;
sCl(1)=Cl;
%*************************************************************************
% Intermediate Variables
%*************************************************************************
% Counters n(step), dc(data), i,j,k(misc)
% Reynold's Number Re
% Prandlt Number Pr
% Drag Coefficient from Mathur and Gutierrez-Miravete et. al. Cdm
% Drag Coefficients from Mulholland, Srivastava, and Wendt:
%   for a single droplet Cd_inf
%   for a rod Cd_rod
%   for a stream of droplets approximating a rod Cd_one
%   for a stream of droplets Cd_stream
%   combined drag coefficient Cd_combined
% Heat Transfer Coefficient h
% Rate of Heat Transfer Q
% Number of Droplets in Currently in Flight nfd
%*************************************************************************
% The Simulation
%*************************************************************************

n = 1;
dc = 1;
while zcur<substrate_position

  n = n+1;

% Calculate Vertical Droplet Acceleration

Re = abs(vzcur*d*Dg(gas)/Vg(gas));
clearance = sqrt(xc(1)^2+yc(1)^2);
Cdm = 0.28+(6/(Re^0.5))+(21/Re);
if clearance>d
```

```
  aznew = g-(Cdm*Dg(gas)*(vzcur^2)*ac)/(2*m);
else
  Cd_inf = Cdm;
  Cd_rod = 0.755/Re;
  Cd_one = (Cd_rod^(-0.678)-Cd_inf^(-0.678))^(-1/0.678);
  Cd_one_plus = Cd_one+(43/Re)*(((vzcur/frq)/d)-1);
  Cd_stream = (Cd_one_plus^(-0.678)+Cd_inf^(-0.678))^(-1/0.678);
  Cd_combined =((d-clearance)/d)*Cd_stream+(clearance/d)*Cd_inf;
  aznew = g-(Cd_combined*Dg(gas)*(vzcur^2)*ac)/(2*m);
end
%*************************************************************************
% Calculate Droplet Thermal State
%*************************************************************************
Cg = specheat(gas,gas_temperature);
avgtmp = (gas_temperature+T)/2;
Cga = specheat(gas,avgtmp);
Re = abs(vzcur*d*Dg(gas)/Vg(gas))
Pr = Vg(gas)*Cg/Kg(gas)
h = Kg(gas)*(2+0.6*(Re^0.5)*(Pr^0.33))*((Cga/Cg)^0.26)/d;
if clearance<d
  zspry=zcur;
  h = h*(Cd_combined/Cd_inf);
end
Q=h*tpfs*as*(T-gas_temperature)/m; % per unit mass
% Calculate thermal variables and density change
if T>Tl
 T=fZnSnlqd(Q,en,Co,T);
 fl=1;
 en=en-Q;
 if T<Tl % This "if" loop is put here to avoid temperature jump at Tl
   T=Tl;
 end
else
 if T>198.5
    Cl=fZnSnmushy(Q,en,Cl,Co);
    fl=(Cl/Co)^(-1);
    T=419.58-3.237*(Cl*100)+7.571e-2*(Cl*100)^2-7.285e-4*(Cl*100)^3
    if T<198.5
      T=198.5;
      Cl=91.2;
      fseut=1-fl;
    end
    en=en-Q;
 else
   if fl>0
    T=198.5;
    fl=fZnSneut(Q,en,fseut,fl);
      if fl<0;
        fl=0;
      end
    en=en-Q;
   else
    T=fZnSnsld(Q,en,Co,T)
    fl=0;
```

```
    en=en-Q;
    end
  end
end
% claculate droplet surface area
 density=DZnSn(Co,Cl,T);
 vlm=m/density;
 d=(6*vlm/pi)^(1/3);
 as=pi*d^2;
% Calculate Droplet Scattering

if sqrt(xc(nd)^2+yc(nd)^2)<(5*d)
  step = nsspfs;
  period = tpss;
else
  step = 1;
  period = tpfs;
end
nfd=nd;
for i = 1:step
  for j = 1:nfd
    axn(j) = 0;
    ayn(j) = 0;
    for k = 1:nfd
        if k ~= j
          dnm = (xc(j)-xc(k))^2+(yc(j)-yc(k))^2+((j-k)*(vzcur/frq))^2;
          axn(j) = axn(j)+sc*(xc(j)-xc(k))/dnm^(3/2);
          ayn(j) = ayn(j)+sc*(yc(j)-yc(k))/dnm^(3/2);
 end
   end
 end
  for j = 1:nfd
    vxn(j) = vxc(j)+((axn(j)+axc(j))/2)*(period);
    vyn(j) = vyc(j)+((ayn(j)+ayc(j))/2)*(period);
    axc(j) = axn(j);
    ayc(j) = ayn(j);
    xc(j) = xc(j)+((vxn(j)+vxc(j))/2)*(period);
    yc(j) = yc(j)+((vyn(j)+vyc(j))/2)*(period);
    vxc(j) = vxn(j);
    vyc(j) = vyn(j);
  end
end

% Update Variables

vznew = vzcur+((aznew+azcur)/2)*tpfs;
azcur = aznew;
zcur = zcur+((vznew+vzcur)/2)*tpfs;
vzcur = vznew;

% store data
sT(n)=T;
sflqd(n)=fl;
sz(n)=zcur;
```

```
stime(n)=(n-1)*tpfs;
sCl(n)=Cl;

end  % while loop

save zno100 sT sflqd sz stime tpfs zspry;
%clg
%plot(szur1, sT1);
%xlabel('Flight Distance [m]');
%ylabel('Temperature [c]');
%title('Temperature vs Flight Distance');
%pause
%clg
%plot(szur1, (1-ssdf1)*100);
%xlabel('Flight Distance [m]');
%ylabel('Liquid Fraction [%]');
%title('Liquid Fraction vs Flight Distance');
%pause
%clg
%plot(stime1, sT1);
%xlabel('Flight Time [sec]');
%ylabel('Temperature [c]');
%title('Temperature vs Flight Time');
%pause
%clg
%plot(stime1, (1-ssdf1)*100);
%xlabel('Flight Time [sec]');
%ylabel('Liquid Fraction [%]');
%title('Liquid Fraction vs Flight Time');

function D=DZnSn(Co,Cl,T)
Tl=419.58-3.237*Co+7.571e-2*Co^2-7.285e-4*Co^3;    %Tin deg C
arp=(22.59+0.9205*1e-2*T)*1e-6;
DSns=7305*(1+arp*(T-20)); %T in deg C, density in kg/m^3
DSnl=7147-0.6895*T;
DZns=7160-0.746*T;
DZnl=7040-0.966*T;
if T > Tl
D=1/((1-Co)/DZnl+Co/DSnl);
else
 if T>= 198.5
 fl=(Cl/Co)^(-1);
 fs=1-fl;
 Cs=0;
 D=1/((fl*(1-Cl)/DZnl)+(fl*Cl/DSnl)+(fs*(1-Cs)/DZns)+(fs*Cs/DSns));
 else
 D=1/((1-Co)/DZns+Co/DSns);
 end
end

function total=eZnSneut(fseut,fl)
Cleut=0.912;
T=198.5;   %Tin deg C
Tk=T+273.15;
```

```
eSns=(21.59*Tk+9.08e-3*Tk^2-7242.50)*1000/118.69;          % in j/kg
eSnl=(28.03*Tk-3.03e5*Tk^(-1)-585.76)*1000/118.69;
eZns=(22.38*Tk+5.02e-3*Tk^2-7121.17)*1000/65.38;
eZnl=(31.38*Tk-3556.4)*1000/65.38;
total=fseut*eZns+(1-fseut-fl)*(1-Cleut)*eZns+(1-fseut-fl)*Cleut*eSns+fl*(1-
Cleut)*eZnl+fl*Cleut*eSnl;

function en=eZnSnlqd(Co,T)
Tk=T+273.15;
eSnl=(28.03*Tk-3.03e5*Tk^(-1)-585.76)*1000/118.69;
eZnl=(31.38*Tk-3556.4)*1000/65.38;
en=(1-Co)*eZnl+Co*eSnl;
%unit for enthalpy is j/kg

function total=eZnSnmushy(Co,Cl)
fl=(Cl/Co)^(-1);
fs=1-fl;
Cs=0;
T=419.58-3.237*(Cl*100)+7.571e-2*(Cl*100)^2-7.285e-4*(Cl*100)^3;   %Tin deg C
Tk=T+273.15;
eSns=(21.59*Tk+9.08e-3*Tk^2-7242.50)*1000/118.69;          % in j/kg
eSnl=(28.03*Tk-3.03e5*Tk^(-1)-585.76)*1000/118.69;
eZns=(22.38*Tk+5.02e-3*Tk^2-7121.17)*1000/65.38;
eZnl=(31.38*Tk-3556.4)*1000/65.38;
total=fs*(1-Cs)*eZns+fs*Cs*eSns+fl*(1-Cl)*eZnl+fl*Cl*eSnl;

function en=eZnSnsld(Co,T)
Tk=T+273.15;
eSns=(21.59*Tk+9.08e-3*Tk^2-7242.50)*1000/118.69;
eZns=(22.38*Tk+5.02e-3*Tk^2-7121.17)*1000/65.38;
en=(1-Co)*eZns+Co*eSns;
%unit for enthalpy is j/kg

function fl=fZnSneut(den,olden,fseut,oldfl)
fl=oldfl-0.00001;
en=eZnSneut(fseut,fl);
endiff=olden-en;
while (abs((den-endiff)/den) > 0.01)
fl=fl-0.00001;
en=eZnSneut(fseut,fl);
endiff=olden-en;
end

function T=fZnSnlqd(den,olden,Co,oldT)
T=oldT-0.2;
en=eZnSnlqd(Co,T);
endiff=olden-en;
while (abs((den-endiff)/den) > 0.01)
T=T-0.001;
en=eZnSnlqd(Co,T);
endiff=olden-en;
end

function Cl=fZnSnmushy(den,olden,oldCl,Co)
```

```
Cl=oldCl+0.00001;
en=eZnSnmushy(Co,Cl);
endiff=olden-en;
while (abs((den-endiff)/den) > 0.01)
Cl=Cl+0.00001;
en=eZnSnmushy(Co,Cl);
endiff=olden-en;
end

function T=fZnSnsld(den,olden,Co,oldT)
T=oldT-0.2;
en=eZnSnsld(Co,T);
endiff=olden-en;
while (abs((den-endiff)/den) > 0.01)
T=T-0.001;
en=eZnSnsld(Co,T);
endiff=olden-en;
end
```

Appendix B

Physical Constants of Zn, Sn, and Pb

The enthalpies for pure Zn, Sn, and Pb in solid and liquid states with respectect to the standard state are expressed, respectively, as [39]:

$$H_{s,Zn} - H_{ST,Zn} = 22.38\,T + 5.02 \times 10^{-3}\,T^2 - 7121.17$$

$$H_{\ell,Zn} - H_{ST,Zn} = 31.38T - 3556.40$$

$$H_{s,Sn} - H_{ST,Sn} = 21.59\,T + 9.08 \times 10^{-3}\,T^2 - 7242.50$$

$$H_{\ell,Sn} - H_{ST,Sn} = 28.03\,T - 3.03 \times 10^{5}\,T^{-1} - 585.76$$

$$H_{s,Pb} - H_{ST,Pb} = 23.55\,T + 4.87 \times 10^{-3}\,T^2 - 7465.00$$

$$H_{\ell,Pb} - H_{ST} = 32.49\,T - 1.54 \times 10^{-3}\,T^2 - 5749.00$$

where T is the temeprature in K and the unit for the entalpies are kJ/kg.

The densities for pure Zn [40], Sn [41], and Pb [41] in solid and liquid states are expressed, respectively, as :

$$\rho_{s,Zn} = 7160 - 0.746T_c$$

$$\rho_{\ell,Zn} = 7040 - 0.966T_c$$

$$\rho_{s,Sn} = 7322 - 0.567T_c$$

$$\rho_{\ell,Sn} = 7147 - 0.6895T_c$$

$$\rho_{s,Pb} = 11680 - 0.567T_c$$

$$\rho_{\ell,Pb} = 11071 - 1.277T_c$$

The relationship between the liquidus temperature and the composition for hypoeutectic Zn-Sn allys (Zn-rich) derived by curve-fitting the liquidus curve in the phase diagram is expressed as:

$$T_\ell = 419.58 - 3.24C_{\ell,\,Sn} + 7.57 \times 10^{-2}C^2_{\ell,\,Sn} - 7.29 \times 10^{-4}C^3_{\ell,\,Sn}$$

where T_ℓ is the liquidus temperature and $C_{\ell,\,Sn}$ is the weight percentage of Sn in the liquid.

The relationship between the liquidus temperature and the composition for hypoeutectic Sn-Pb allys (Sn-rich) is expressed as [42]:

$$T_\ell = 232.3 - 1.99C_{\ell,\,Pb} + 3.40 \times 10^{-2}C^2_{\ell,\,Pb} - 4.29 \times 10^{-4}C^3_{\ell,\,Pb}$$

where T_ℓ is the liquidus temperature and $C_{\ell,\,Pb}$ is the weight percentage of Pb in the liquid.

The partition ratios for hypoeutectic Sn-Pb allys (Sn-rich) are approximated by [42]:

$$k = 0.096 - 1.56 \times 10^{-3}C_{\ell,\,Pb} + 2.01 \times 10^{-5}C^2_{\ell,\,Pb}$$

where k is the partition ratio and $C_{\ell,\,Pb}$ is the weight percentage of Pb in the liquid.

Bibliography

1 Singer, A.R.E. and Evans, R.W., 1983, "Incremental Solidification and Forming," *Metals Technology*, vol. 10, February, pp. 61-68.

2 Sridharan, K., Perepezko, J.H., 1994, "Microstructure Control in Alloy Steel Powders", International Journal of Powder Metalurgy, Vol 30, no 3., pp. 301-311.

3 Leatham, A.G. and Lawly, A., 1993, "The Osprey Process: Principles and Applications," *The International Journal of Powder Metallurgy*, vol. 29, no. 4, pp. 321-329.

4 Lavernia, E.J., Gutierrez, E.M., Szekely, J., and Grant, N.J., 1988, "A Mathematical Model of the Liquid Dynamic Compaction Process. Part 1: Heat Flow in Gas Atomization," *International Journal of Rapid Solidification*, Vol. 4, pp. 89-124.

5. Smith, R.W., Novak, R., 1991, "Advances and Applications in U.S. Thermal Spray Technology: 1. The Market and R&D," *Powder Metallurgy International*, Vol. 23, no. 3, pp. 231-236.

6 Thorpe, M.L.,"Thermal Spray Industry," Advanced Materials & Processes, May 1993, pp. 50-61.

7 Annavarapu, S. and Doherty, R.D., 1993, "Evolution of Microstructure in Spray Casting," *The International Journal of Powder Metallurgy*, Vol. 29, no. 4, pp. 331-343.

8 Liang, X., Earthman, J.C., and Lavernia, E.J., 1992, "On the Mechanism of Grain Formation During Spray Atomization and Deposition," *Acta Metallurgica et Materialia*, Vol. 40, no.11, pp. 3003-3016.

9 Bewlay, B. P. and Cantor, B., 1991, "The Relationship between Thermal History and Microstructure in Spray-Deposited Tin-Lead Alloys," *Journal of Materials Research*, Vol. 6, no. 7, pp. 1433-1454.

10 Payne, R.D., Matteson, M.A., and Moran, A.L., 1993, "Application of Neural Networks in Spray Forming Technology," *The International Journal of Powder Metallurgy*, Vol. 29, no. 4, pp. 345-351.

11 Acquaviva, P. J., Nowak, T., and Chun, J. H. "Issues in Application of Thermal Spraying to Metal Mold Fabrication," Proceedings of the International Body Engineering Conference (IBEC '94) on Advanced Technologies and Processes, Detroit, Michigan, USA, September 26-29, 1994.

12 Gutierrez-Miravete, E., Lavernia, E.J., Trapaga, G.M., Szekely, J, and Grant, N.J., 1989, "A Mathematical Model of the Spray Deposition Process," *Metallurgical Transactions A*, Vol. 20A, no. 1, pp. 71-85.

13 Mathur, P., Apelian, D., and Lawley, A., 1989, "Analysis of the Spray Deposition Process," *Acta Metallurgica*, Vol. 37, no. 2, pp. 429-443.

14 Payne, R.D., Moran, A.L., and Cammarata, R.C., 1993, "Relating Porosity and Mechanical Properties in Spray Formed Alloy 625," *Ship Materials Engineering Department Research and Development Report*, January, pp. 1-14.

15 Chun, J.-H. and Passow, C.H., 1993, "Droplet-Based Manufacturing," *Annals of the CIRP*, Vol. 42, no. 1, pp. 235-238.

16 Passow, C. H., J. H. Chun and T. Ando, 1993, "Spray Deposition of a Sn-40 wt pct Pb Alloy with Uniform Droplets," *Metallurgical Transactions A*, Vol. 24A, pp. 1187-1193.

17 Szekelly, J. and Fisher, R.J, 1970, "On the Solidification of Metal Spheres Due to Thermal Radiation at the Bonding Surface," *Metallurgical Transactions* , Vol. 1, pp. 1480.

18 Hodkin, D.J., Sutcliffe, P.G., and Russel, E.L., 1973, *Powder Metetallurgy*, Vol. 16, pp. 277.

19 Glickstein, M.R., Patterson, R.J. II, Shockley, *Rapid Solidification Processing: Principles and Technologies*, R. Mehrabian, B.H. Kear, and M. Cohen (eds.), Claitor Publishing Division, Baton Touge, LA (1978), pp. 46.

20 Levi, C.G. and Mehrabian, R., 1980, "Heat Flow in Atomized Metal Droplets," *Metallurgical Transactions B.*, Vol. 11B, pp. 21.

21 Levi, C.G. and Mehrabian, R., 1982, "Heat Flow during Rapid Solidification of Undercooled Metal Droplets," *Metallurgical Transactions A*, vol. 13A, pp. 221.

22 Turnbull, D., *Thermodynamics in Physical Metallurgy*, American Society for Metals, Metals Park, OH, 1949.

23 Levi, C.G., 1988, "Thermal Considerations on the Recalesence of Alloy Powders," *Metallurgical Transactions A*, Vol. 19A, pp. 687.

24 Zhao, Q., "Evolution of the Rapid Solidfication Structure of Highly Undercooled Ni-25wt% Sn Alloy" Ph.D. Thesis, Department of Materials Science and Engineering, MIT, 1992.

25 Lipton, J., Kurz, W., Trivedi, R., 1987, "Rapid Dendrite Growth in Undercooled Alooys", *Acta Metallurgica*, Vol. 35, pp. 957.

26 Passow, C.H., "A Study of Spray Forming Using Uniform droplet Sprays," S.M. Thesis, Department of Mechanical Engineering, MIT, 1992.

27 Turnbull, D., 1950, "The Supercooling of Aggregates of Small Metal Particles," *Journal of Metals, Transactions AIME*, Vol. 188, pp. 1144.

28 Turnbull, D., and Cech, R.E., 1950, "Microscopic Observation of the Solidification of Small Metal Droplets," *Journal of Applied Physics*, Vol. 21, pp. 804.

29 Chu, M.G., Shiohara, Y., and Flemings:, M.C., 1984, "Solidification of Highly Undercooled Sn-Pb Alloy Droplets," *Metallurgical Transactions A*, Vol. 15A, pp. 1303.

30 Piccone, T.J., Wu, Y., Shiohara, Y., Flemings, 1987, Dendrite Growth of Undercooled Nickel-Tin: Part II," *Metallurgical Transactions A*, 18A, pp. 925.

31 Wu, Y., Piccone, T.J., Shiohara, Y., Flemings, M.C., 1988, "Dendrite Growth of Undercooled Nickel-Tin: Part III," *Metallurgical Transactions A*, Vol. 19A, pp. 1109.

32 Zhao, Q, Piccone, T.J., Shiohara, Y., Flemings, M.C., 1989, "Rapid Quenching and Powder Preparation", *Proceedings of Materials Research Society International Meeting on Advanced Materails*, Vol. 3, pp. 597.

33 Suzuki, M., Piccone, T.J., Flemings, M.C., Brody, H.D.,1991, "Solidification of Highly Undercooled Fe-P Alloys", *Metallurgical Transactions A*, Vol. 22A, pp. 2761.

34 Mathur, P.C.,"Analysis of the Spray Deposition Process," Ph.D. Thesis, Drexel University, 1988.

35 Mulholland, J.A., Srivastava, R.K., and Wendt, J.O.L., "Influence of Droplet Spacing on Drag Coeffiecient in Nonevaporating, Monodisperse Streams," *AIAA Journal*, 26(10), 1231.

36 Flemings, M.C., *Solidification Processing*, McGraw-Hill, New York, (1974).

37 Perepezko, J.H., "Nucleation in Undercooled Liquids," *Materials Science and Engineering*, 65,125-135, 1984.

38 Perepezko, J.H., "Solidification of Highly Supercooled Liquid Metals and Alloys," *Journla of Non-Crystalline Solids*, 156-158, 463-472, 1993.

39 Hultgren, R., Desai, P.D., Hawkins, D.T., Gleiser, M., Kelley, K.K., 1973, *Selected Values of the Thermodynamic Properties of the Elements*, ASM, Metals Park, OH, pp. 379, 477, and 501.

40 Pelzel, E. and Sauerwald, F., 1941, Zeitschrift fur Metallkunde, Vol. 33, pp. 229.

41 Poirier, D.R., 1988, "Densities of Pb-Sn Alloys during Solidification," *Metallurgical Transactions A*, Vol. 19A, pp. 2349.

42 Poirier, D.R., Nandapurkar, P., 1988, "Entalpies of a Binary Alloy during Solidification", *Metallurgical Transactions A*, Vol. 19A, pp. 3059.